



UNIVERSIDAD DE CONCEPCIÓN
FACULTAD DE CIENCIAS FÍSICAS Y MATEMÁTICAS

Exploring the formation of supermassive black holes in protostar clusters, incorporating a hydrodynamic treatment

Its sensitivity to different temperatures

Por: Paulo Antonio Solar Vera

Tesis presentada a la Facultad de Ciencias Físicas y Matemáticas para optar
al grado académico de Magíster en Ciencias con Mención en Física

December 2022
Concepción, Chile

Profesor Guía: Dr. Dominik Schleicher



© 2022, Paulo Solar Vera

Se autoriza la reproducción total o parcial, con fines académicos, por cualquier medio o procedimiento, incluyendo la cita bibliográfica del documento



ACKNOWLEDGEMENTS

En Primer lugar me gustaría agradecer a mi familia, mis padres Tranquilina y Patricio, mi abuelita María y mis hermanos Andres, Ignacio y Patricia por apoyarme en cada paso tanto en mi carrera como en la vida, por siempre escuchar mis problemas, darme consejos, creer en mi y a pesar de las dificultades brindarme su apoyo y cariño sincero. Quiero agradecer especialmente a mi madre por su amor incondicional, ser un ejemplo y una guía para mi. Agradezco a mi esposa Annina por su amor, apoyo, paciencia, comprensión y ser una compañera en mis años de estudio, darme la tranquilidad en los momentos difíciles y compartir conmigo los momentos de felicidad. También me gustaría expresar mi gratitud a los amigos y compañeros que fui haciendo a lo largo de mi carrera. Así como también a mis amigos de toda la vida.

I would also like to acknowledge my professor and supervisor Dominik Schleicher for guiding me and supporting me in the development of my thesis, as well as in the moments out of the office. I would like to express my gratitude to Prof. Ralf Klessen for his always useful advices and corrections. And I especially thank Bastian Reinoso for his help from the beginning to solve code problems and for the productive discussions about the investigation.

Financial support from the Millenium Nucleus NCN19-058 (TITANs) and from FONDECYT REGULAR (project code 1201280) are acknowledged. My simulations were performed using KULTRUN cluster at the Astronomy Department of the Universidad de Concepción.

Resumen

Los agujeros negros supermasivos tienen un origen enigmático y en los últimos años se han descubierto más de 200 de ellos con masas de alrededor de $10^9 M_{\odot}$ con un corrimiento al rojo muy alto $z > 6$. La formación de los primeros agujeros negros supermasivos sigue siendo una pregunta abierta en cosmología y uno de los caminos para explicar su formación es la creación de semillas de agujeros negros supermasivos a través de la acreción y colisiones en cúmulos masivos con una alta densidad estelar. En esta tesis investigamos la formación de una semilla de un agujero negro supermasivo mediante de un escenario de formación de colisiones y acreción en un cúmulo estelar denso de Población III en una nube de gas primordial. Además investigamos la sensibilidad del modelo a distintas temperaturas iniciales. Realizamos simulaciones de tres dimensiones multifísicas incluyendo hidrodinámica y dinámica de N-cuerpos con el código AMUSE. Utilizamos las condiciones iniciales de un sistema compacto, con un gas monoatómico en muy baja metalicidad con diferentes temperaturas iniciales, imitando enfriamientos de hidrógeno atómico o hidrógeno molecular del gas. Nuestros resultados apuntan a que es posible la formación de un objeto masivo central a través de colisiones y acreción del gas, alcanzando para todas las temperaturas (500–8000 K) masas del orden de $10^4 M_{\odot}$, siendo casi la masa total del sistema. Observamos que el cambio en la temperatura no impide la formación de un objeto muy masivo, pero puede influenciar su evolución. Las altas temperaturas de los gases reducen la acreción como resultado de las altas presiones centrales en el cúmulo, en comparación a temperaturas más bajas se alcanzan mayores tasas de acreción producto de una baja presión central, llevando a la formación de un objeto central masivo en menos tiempo. Este estudio amplía nuestro conocimiento en la formación de una semilla de un agujero negro supermasivo, incorporando un tratamiento numérico hidrodinámico del gas y recetas de acreción más sofisticadas. La implementación numérica del gas y recetas de acreción más avanzadas es un gran paso para comprender la formación de agujeros negros supermasivos. Es necesario implementar efectos de enfriamiento y calentamiento del gas físicamente consistente, añadir la química del gas y efectos de retroalimentación radiativa por parte de las protoestrellas y como ellos afectan a la evolución y formación de objetos masivos en el futuro.

Keywords – black hole physics – methods: analytical – galaxies: nuclei – quasars:

supermassive black holes - stars: formation - stars: Population III



Abstract

Supermassive black holes have an enigmatic origin and in the last years more than 200 have been discovered with masses around $10^9 M_{\odot}$ at very high redshift $z > 6$. The formation of the first supermassive black holes is still an open question in cosmology and one of the pathways for their formation is the creation of supermassive black hole seeds through accretion and collisions in massive clusters with a high stellar density. In this thesis we investigate the formation of a supermassive black hole seed through collisions and accretion in a dense Population III star cluster in a primordial gas cloud. In addition, we investigate the sensitivity of the model to different initial temperatures. We perform three-dimensional multi-physics simulations including hydrodynamics and N-body dynamics with the AMUSE code. We used initial conditions of a compact system, with a monoatomic gas at very low metallicity with different initial temperatures, mimicking cooling of atomic hydrogen or molecular hydrogen of the gas. Our results indicate that the formation of a central massive object through collisions and gas accretion is possible, reaching for all temperatures (500 – 8000 K) masses of the order of $10^4 M_{\odot}$, being about the total mass of the system. We observe that the change in temperature does not prevent the formation of a very massive object, but it can influence its evolution. High gas temperatures reduce accretion as a result of high central pressures in the cluster, compared to lower temperatures, higher accretion rates are achieved as a result of low central pressure, leading to the formation of a massive central object in less time. This study has extended our knowledge on the formation of supermassive black hole seeds, incorporating a hydrodynamic numerical treatment of the gas and more sophisticated accretion recipes. The numerical implementation of the gas and more advanced accretion recipes is a great step forward to understand the formation of supermassive black holes. It is necessary to implement physically consistent cooling and heating, add gas chemistry and radiative feedback effects by protostars and how they affect the evolution and formation of massive objects in the future

Keywords – black hole physics – methods: analytical – galaxies: nuclei – quasars: supermassive black holes - stars: formation - stars: Population III

Contents

AGRADECIMIENTOS	i
Resumen	ii
Abstract	iv
1 Introduction	1
1.1 Context	1
1.2 Formation mechanisms of supermassive black holes at high redshift	4
1.2.1 Direct collapse scenario	6
1.2.1.1 Photodissociation of H_2 by LW radiation	7
1.2.1.2 H^- photodetachment	9
1.2.1.3 Collisional H_2 dissociation	10
1.2.2 Supermassive black holes from Pop. III stars and supermassive stars	10
1.2.3 Massive black holes via runaway collisions in a dense star cluster	15
1.3 Previous work	20
1.4 This project	22
2 Numerical Method	24
2.1 AMUSE	24
2.1.1 The AMUSE framework	24
2.2 The Bridge Method	27
2.3 Hydrodynamics	28
2.3.1 Barnes-Hunt treecode	30
2.3.2 Smoothed Particle Hydrodynamics Method	32
2.3.3 Smoothing lengths	36
2.3.3.1 Scatter interpretation	36
2.3.3.2 Gather interpretation	36
2.4 Gravity	38
2.4.1 Equations of motion for a self-gravitating system	38
2.4.2 Ph4 Code	39
2.4.2.1 The Ahmad-Cohen scheme	42
2.5 Sink particles	43

2.5.1	Sink accretion	45
2.5.1.1	Timescale for spherically symmetric radial accretion	47
2.5.1.2	Timescale for disc accretion	48
2.5.1.3	Net timescale for accretions models	48
2.5.2	Sink update	52
2.5.3	Angular momentum feedback from a sink particle	53
2.5.4	Stellar collisions	55
2.5.5	The Mass-Radius Parametrization	56
2.5.5.1	PROTOSTAR STAGE	57
2.5.5.1.1	'SMS' Track	57
2.5.5.1.2	'VMS' Track	58
2.5.5.1.3	"NORMAL" Track	59
2.5.5.2	STAR STAGE	60
2.5.5.3	SUPERMASSIVE STAR STAGE	60
3	Development of the Setup	61
3.1	Previous steps for the implementation	61
3.2	Initial temperature	61
3.3	External pressure	62
3.4	High density limitation	65
3.4.1	Adiabatic implementation	66
3.4.2	Sink creation	68
3.4.2.1	Density criterion	69
3.4.2.2	Sink-overlap criterion	69
3.4.2.3	Gravitational potential minimum criterion	70
3.4.2.4	Hill Sphere criterion	70
3.5	Setup	70
3.6	Computational resources	71
4	Results	73
4.1	Runaway collisions and accretion simulations	73
4.2	Colder temperatures	87
5	Discussion and conclusions	107
5.1	Summary and conclusions	107
5.2	Discussion	109
	Referencias	113

List of Tables

3.5.1 Summary of the initial conditions.	71
4.1.1 Summary of the simulations. From left to right the columns correspond to the simulation name, final mass of the MMO, mean accretion of the MMO, percentage of the MMO final mass as a function of the total mass of the system, the final gas mass, mean temperature, final star number, final star mass, number of collisions and the total escaped mass.	75
4.2.1 Summary of the mean values for the 8000 K simulations and simulations with initial temperatures of 5000 K, 1000 K and 500 K, from top to bottom. From left to right the columns correspond to the simulation name, final mass of the MMO, mean accretion of the MMO, percentage of the final mass of the MMO as a function of the total mass of the system, the final gas mass, mean temperature, final star number, final star mass, number of collisions and the total escaped mass.	89

List of Figures

- 1.1.1 Masses and redshifts of 203 quasars known at $z \geq 6$. 79 of these 203 quasars are from Bañados 2016. 8 quasars from Pan-STARRS (Mazzucchelli et al. 2017, Tang et al. 2017, Koptelova et al. 2017, Bañados et al. 2018), 3 quasars from VIKING (Decarli et al. 2018, Venemans et al. 2019), 37 quasars from a combination of DES/SDSS, UKIRT, VISTA and WISE (Wang et al. 2016a, Reed et al. 2017, Wang et al. 2017, Reed et al. 2019, Wang et al. 2019, Fan et al. 2019b, Yang et al. 2019), 72 quasars from the SHELLQs and other Subaru surveys (Kashikawa et al. 2015, Matsuoka et al. 2018a,b, 2019b,a) and 4 quasars from a combination of VST-ATLAS and WISE (Carnall et al. 2015, Chehade et al. 2018). Here the masses were estimated from the rest-frame UV luminosity, assuming a constant bolometric correction and Eddington ratio of $f_{\text{Edd}} = 1$. The two black curves illustrate the mass of a BH as a point of comparison. Starting from a seed BH of stellar mass $M_{\bullet} = 10 M_{\odot}$ (lower curve) or $100 M_{\odot}$ (upper curve) at $z = 35$, the mass of a BH constantly increases at the Eddington rate, with a radiative efficiency of $\varepsilon = 0.1$. From Inayoshi et al. (2020). 3
- 1.2.1 The image shows three potential ways that SMBH seeds were created in the early Universe. The left-hand route shows how the initial generation of stars collapsed, which were formed from gas with the expected abundances after recombination ($Z = 0$). Alternatively on the right side, both of these scenarios require the presence of few metals ($Z < Z_{\text{crit}}$) in a gas cloud that will form a disc as it cools and then a star cluster that may experience a runaway collision process producing a massive star or black hole. However if star formation is suppressed, a strong inflow of gas is anticipated at the center of the cloud, creating a supermassive star or an IMBH. From Volonteri (2010). 5
- 1.2.2 Conditions for the direct collapse scenario, where the lines represent the radiation flux required to destroy and suppress the formation of H_2 molecules in a $10^7 M_{\odot}$ gas cloud. The black and blue dashed lines represent one zone and 3D models, along with a red cross including an X-Ray ionization background which however makes little difference. From Latif et al. (2015). 9

1.2.3	Final fate of massive single stars as a function of the initial metallicity and initial mass. The green line separates the regimes where the stars keep their hydrogen envelope (left and lower right) from those where the hydrogen envelope is lost. The dashed blue line indicates the border of direct black hole formation (black region). At lower masses and higher metallicities is the regime of BH formation by fallback (red zone) and the green zone indicates the formation of neutron stars. Also note that the white zone between the BH formation zones is a strip of pair-instability supernovae that leave no remnant. From Heger et al. (2003)	12
1.2.4	Possible detection of the first stars. Absorption profile of the 21 cm line plotted against the redshift and the age of the Universe. The signal is absorbed due to the change of the spin of the H atoms that are around the first stars. The black solid line is the best fit for the hardware and software configurations which yields the best signal-to-noise ratio. From Bowman et al. (2018)	13
1.2.5	Resulting mass distributions of Pop III.1 (left) and III.2D (right) stars for different redshifts. The different colours represent different redshift ranges. The black solid lines show the total distributions over all redshifts for each population and the dotted lines show the sum of them. From Hirano et al. (2015)	14
1.2.6	Percentage of realizations which produce a VMS (f_{VMS})(top) and the most massive VMS ($M_{\text{VMS,max}}$)(bottom) as a function of the initial central stellar mass density for the top-heavy Salpeter IMF assuming $S = 0$ and $b = 0$. From Katz et al. (2015)	17
1.2.7	The top panel shows the mass evolution of the runaway star ($M_{\text{max}}(t)/M_{\text{ini}}$) in a cluster with $N = 5000$ stars, where each star has an initial mass of $M_* = 2 M_{\odot}$ and an initial radius of $R_* = 200 R_{\odot}$. The middle panel shows the number of collisions (N_{col}) as a function of the crossing time of the cluster, and the red line is the best Gaussian fit. The bottom panel is the mass growth rate dM/dt in $M_{\text{ini}}T_{\text{cr}}^{-1}$. From Reinoso et al. (2018)	18
1.2.8	Evolution of different types of the shape of the model cluster (A, B, and C clusters) represented by triangles, circles, and squares, respectively, with $N = 10^3$ stars on the left side and $N = 10^4$ on the right side (for more information about the A, B and C cluster see Table 1 in Vergara et al. (2021)). Results are given for initial stellar radii $R = 50, 1000 R_{\odot}$ as a function of rotation factors (k -factor). Top panel: Normalized number of escaper. Middle panel: Normalized number of collisions with the most massive object. Bottom panel: Mass of the most massive object. From Vergara et al. (2021)	19

1.3.1	Time evolution of the maximum mass in the system, for six different accretion models and standard set of parameters. All models efficiently convert at least half of the initial gas mass into one single massive object, except for the model 5. From Boekholt et al. (2018) .	21
1.3.2	The expected evolution of the stellar cluster during the formation of a central massive object. At the times A-B the most massive star sinks to the center. At time C) the most massive star in the center accretes material through both stellar collisions and gas reservoir. Finally at time D) the supermassive star collapses into a very massive black hole. From Schleicher et al. (2022) .	22
2.1.2	Fundamental domains of AMUSE. Multiscale and multiphysics codes are connected disciplines, as depicted in the domain-application plane. Figure from Portegies Zwart and McMillan (2018) .	27
2.3.1	2D y 3D example of the construction of the hierarchical tree. From Apple Developer Documentation.	31
2.3.2	Schematic image of the SPH method. Domain of particle i with kernel function W which shows the influence of neighbouring particles j , determined by the smoothing length limit h . Particle j is at a distance r from particle i . From Duckworth et al. (2021) .	35
2.3.3	In (a) we illustrate the “scatter” interpretation. In (b) the “gather” interpretation is demonstrated (Hernquist and Katz, 1989a).	37
2.5.1	Configuration of a SPH particle near the accretion radius of a sink particle. The volume that contains SPH particles is shaded, and the white volume is the inside of the accretion radius contains no gas particles. From Bate et al. (1995) .	45
3.3.1	Different snapshots for the time evolution of the gas cloud density with a mass of $M = 3 \times 10^4 M_{\odot}$ and radius $R = 0.14$ pc, without the external pressure implementation. The red arrows represent the gas velocity field.	63
3.3.2	Different snapshots for the time evolution of the gas cloud density with a mass of $M = 3 \times 10^4 M_{\odot}$ and radius $R = 0.14$ pc, with the external pressure implementation. The red arrows represent the gas velocity field.	65
3.4.1	Pressure vs Volume for an isothermic equation of state (red line), an adiabatic state equation (green line) and an equation of state according to the equation proposed in 3.4.3 for different densities (dashed lines).	67
3.4.2	Temperature evolution of prestellar clouds with different metallicities. The metallicities $[Z/H] = -\infty$ ($Z = 0$), -5 , -3 , -1 and -6 , -4 , -2 , 0 are shown by solid and dashed lines. The lines for constant Jeans mass are indicated by thin dotted lines. From Omukai et al. (2005) .	68

4.1.1	Density projections for simulations with an initial temperature of 8000 K at different times of a primordial gas cloud with an embedded protostar cluster. The black dots are the protostars and the red dot is the MMO of the cluster. The collapse of the gas cloud and the migration of the MMO towards the cluster center are observed.	74
4.1.2	Time evolution of the mass fraction for the simulations with an initial temperature of 8000 K of the gas (blue zone), stars (red zone) and the mass that escapes (green zone), according to the escape criterion. The green dotted lines are the times when the protostars accreted 25%, 50%, 75% and 90% of the gas mass.	76
4.1.3	Time evolution of the 90%, 75%, 50%, 30% and 10% Lagrangian radii in one of our 8000 K simulations. In the top panel the Lagrangian radii for the protostars labeled as 'Stars' are shown, in the middle panel for the gas 'Gas' and in the bottom panel the Lagrangian radii for the total system 'Gas + Stars'.	78
4.1.4	Evolution of the gas and protostellar mass for the simulations Sim1, Sim2 and Sim3 with an initial temperature of 8000 K (top panel). Comparison of the time evolution of the MMO mass and the total mass of the protostars without the MMO (second panel), accretion rate of the MMO with the mean accretion rate of the other protostars (third panel), where the black dashed line is the limit accretion rate $\dot{m}_{lim} = 0.04 M_{\odot}/\text{yr}$, for when a protostar passes to the 'SMS Track'. The radius of the MMO with the mean radii of the other protostars (fourth panel). Finally, the evolution of the collision rates over time (bottom panel).	80
4.1.5	Time evolution of the correlation between the MMO mass together with the masses of the 9 MMOs in the system (top panel), and the distance from the center of the MMOs and the 9 MMOs in the system (bottom panel) for the three 8000 K simulations.	82
4.1.6	Time evolution of the fraction of stars belonging to four categories: (1) single protostars (orange, 'single star'), (2) stars that have collided with and are part of the most massive star in the system (red, 'MMO'), (3) stars that are part of other collision products (green, 'Collision prod.') and (4) escaper star (blue, 'Escaper'). The black dashed line shows the moment when the system is dominated by the protostellar mass. The green dotted lines are the times when the protostars accreted 25%, 50%, 75% and 90% of the gas mass. In all our simulations initially the protostars are single stars. The stars will actively interact with one another as they get larger from the gas they are accreting and in general, we see a fast increase in collisions with the MMO, few collisions with other collision products and a drop in the percentage of single stars. Also zero percentage of escapers.	84

4.1.7	Final mean masses of the MMO for the three simulations from left to right with an initial temperature of 8000 K at 0.35 Myr. The blue color is the mass acquired through collisions and the orange color is the mass obtained by accretion. In all cases MMOs obtain their mass mostly through accretion.	85
4.1.8	Box plot for the three simulations (from left to right) of 8000 K, of the protostar masses that collided with the MMOs. For all three cases the average masses are less than $10 M_{\odot}$	86
4.1.9	The top panels show the time evolution of the mass rate obtained by the MMO through collisions Δm_{coll} and accretion Δm_{acc} . The bottom panels show the increases in the radius of the MMO through collisions and accretion ΔR_{coll} and ΔR_{acc} . We observe that accretion plays a fundamental role in the entire evolution of the MMO for all cases, but it is especially relevant at the beginning of the evolution.	87
4.2.1	Density projections for a simulation with an initial temperature of 500 K at different times of a primordial gas cloud with an embedded protostar cluster. The black dots are the protostars and the red dot is the MMO of the cluster. A slight fragmentation is observed, as well as a rapid collapse after 10000 yr compared to the 8000 K simulations.	88
4.2.2	Efficiency of the MMOs as a function of M_{gas}/M_{Jeans} for the simulations with different temperatures explored in this thesis (red points), Chon and Omukai (2020) (green point), Solar et al. (2022) (blue point) and Reinoso et al. in preparation (orange point).	90
4.2.3	Time evolution of the mass fraction for the simulations with an initial temperature of 300 K, 500 K and 1000 K of the gas (blue zone), stars (red zone) and the mass that escaped (green zone), according to the escape criterion indicated above. The green dotted lines are the times when the protostars accreted 25%, 50%, 75% and 90% of the gas mass and the black solid line is the moment when the system is dominated by the protostars mass.	92
4.2.4	Time evolution of the 90%, 75%, 50%, 30% and 10% Lagrangian radii in the 5000 K simulations. In the top panel the Lagrangian radii for the protostars labeled as 'Stars' are shown, in the middle panel for the gas labeled 'Gas' and in the bottom panel the Lagrangian radii for the total system 'Gas + Stars'. In general we observe a similar behavior to the 8000 K simulations, with slight differences in the gas collapse.	93

4.2.5	Time evolution of the 90%, 75%, 50%, 30% and 10% Lagrangian radii in the 1000 K simulations. In the top panel the Lagrangian radii for the protostars denoted as 'Stars' are shown, in the middle panel for the gas labeled 'Gas' and in the bottom panel the Lagrangian radii for the total system 'Gas + Stars'. Very similar development of the protostars as in the 8000 K simulation, but with a more rapid collapse due to lower pressure.	94
4.2.6	Time evolution of the 90%, 75%, 50%, 30% and 10% Lagrangian radii in the 500 K simulations. In the top panel the Lagrangian radii for the protostars denoted as 'Stars' are shown, in the middle panel for the gas labeled as 'Gas' and in the bottom panel the Lagrangian radii for the total system 'Gas + Stars'. With a very similar development of the protostars as in the 1000 K and 8000 K.	95
4.2.7	Time evolution of the mean gas density and pressure for the simulations with temperatures of 8000 K, 5000 K, 1000 K and 500 K. We observe higher densities and pressures at the beginning of the evolution for the higher temperature simulations.	96
4.2.8	Evolution of the gas and protostellar mass for the simulations Sim4, Sim5 and Sim6 with an initial temperature of 300 K, 500 K and 1000 K (top panel). Comparison the time evolution of the MMO mass and the total mass of the protostars without the MMO (second panel), the accretion rate of the MMO with the mean accretion rate of the other protostars (third panel), where the black dashed line is the limit accretion rate $\dot{m}_{lim} = 0.04 M_{\odot}/\text{yr}$, for when a protostar passes to the 'SMS Track'. The radius of the MMO and the mean radii of the other protostars (fourth panel). Finally, the evolution of the number of collision over time (bottom panel).	98
4.2.9	Time evolution of the fraction of stars belonging to four categories: (1) single protostars (orange, 'single star'), (2) stars that have collided with and are part of the most massive star in the system (red, 'MMO'), (3) stars that are part of other collision products (green, 'Collision prod.') and (4) escaper star (blue, 'Escaper'). The black solid line shows the moment when the system is dominated by the protostars mass. The green dotted lines are the times when the protostars accreted 25%, 50%, 75% and 90% of the gas mass.	100
4.2.10	Final masses of the 10 most massive objects in all simulations performed to 0.25 – 0.35 Myr. The blue color is the mass acquired through collisions and the orange color is the mass obtained by accretion. It is noted that accretion is the predominant means by which massive objects obtain mass for all temperatures explored here.	101
4.2.11	Boxplot for the three 8000 K simulations and the 300 K, 500 K, 1000 K simulations, in this order from left to right for the masses of protostars that collided with the MMOs. There is a slight incline from larger masses to higher temperatures.	102

- 4.2.12 The left panels show the time evolution of the mass obtained by the MMO through collisions Δm_{coll} , accretion Δm_{acc} and the total mass Δm_{Tot} in the time for all simulations. The right panels show the increases in the radius of the MMO through collisions and accretion ΔR_{coll} , ΔR_{acc} and the total radius ΔR_{Tot} in the time for all simulations. 104
- 4.2.13 Parameters of the most massive object as a function of the initial temperature in each simulation. Mass reached at the end of the simulation (upper left), mean radii (lower left), mean accretion rates (upper right), and number of total collisions at the end of the simulation (lower right). 105



Chapter 1

Introduction

1.1 Context

One of the largest enigmas in modern astronomy is the early evolution of the our Universe, particularly the formation of the first Supermassive Black Holes (SMBHs) and the reionization epoch where the neutral intergalactic medium in the Universe was ionized by the first luminous sources. SMBHs are very compact astrophysical objects that can be found in the early Universe and in the local Universe. They can reach large masses of $\sim 10^6 - 10^9 M_{\odot}$ (Volonteri, 2010), until a few $10^{10} M_{\odot}$ (Pacucci et al., 2017; McConnell et al., 2011; Ghisellini et al., 2010). A topic of special interest within the field of compact objects and high energies is the formation of the first black holes, and their evolution to the present day. Over the last years, more than 200 SMBHs with masses $M > 10^9 M_{\odot}$ have been discovered at high redshift $z > 6$ (Fan et al., 2001; Willott et al., 2010; Venemans et al., 2015; Jiang et al., 2016; Bañados et al., 2016; Reed et al., 2017; Matsuoka et al., 2018; Shen et al., 2019). The most massive quasar SDSS J010013.02+280225.8 (Wu et al., 2015) has a mass of $1.2 \times 10^{10} M_{\odot}$ at a redshift of $z = 6.3$. The most distant Quasar known to date is ULAS J1342+0928 with a mass of $7.8 \times 10^8 M_{\odot}$ at $z = 7.54$ (Bañados et al., 2018) when the Universe was 690 Myr old. Fig. 1.1.1 shows the redshifts and inferred masses of the 203 known quasars at $z \geq 6$. With the new generation of telescopes like the James Webb Space Telescope (JWST)¹ (J. P. Gardner et al., 2006) it will be possible to extend these extremely important observations.

¹<https://www.jwst.nasa.gov>

With observations we can detect supermassive black holes that have masses of $10^6 - 10^9 M_\odot$ in the local Universe. In the early Universe probably the smallest detectable mass is more like $10^7 M_\odot$. It is not surprising that SMBHs exist in the local Universe given that black holes from the early Universe have had more than 12 Gyr to evolve. Recently with the Event Horizon Telescope (EHT)², we were able to observe the shadow of Sagittarius A* (Collaboration, 2022), the SMBH at the center of our Galaxy with a mass of $4.5 \times 10^6 M_\odot$ at a distance of $d = 8.4$ kpc (Schodel et al., 2002; Ghez et al., 2008) as well as the SMBH in the center of the elliptical galaxy M87 with a mass of $6.5 \pm 0.7 \times 10^9 M_\odot$ and a distance of 16.8 ± 0.8 Mpc (Event Horizon Telescope Collaboration et al., 2019). Really intriguing is the presence of $> 10^9 M_\odot$ SMBHs at high redshift ($z \geq 6$) because these SMBHs were formed within the first billion years after the Big Bang. Explaining the existence of these objects provides a significant challenge to our cosmological model (D'Amico et al., 2018).

The presence of SMBHs makes us wonder how these objects have grown so much and so quickly. An explanation for the formation of SMBHs in the early Universe is that these were born of BHs from the initial Population III (Pop III) stars, which were produced by primordial gas molecular hydrogen (H_2) cooling and they are the first generation of stars in our Universe. Due to inefficient fragmentation caused by inefficient cooling, the temperature difference between the metal-free primordial gas and the star-forming molecular clouds in the interstellar medium (ISM) of low- z galaxies has led to Pop III stars that were unusually massive.

$$\dot{M}_{\text{Edd}} = \frac{4\pi GM}{\varepsilon \kappa c} \quad (1.1.1)$$

If a BH from these Pop III stars has grown via Eddington-limited accretion by Equation 1.1.1 where G is the universal gravitational constant, M the mass of the central object, ε the radiative efficiency, κ the opacity and c the speed of light. This is the upper limit for spherical accretion of a black hole. The seeds of high- z SMBHs will grow exponentially assuming a radiative efficiency of $\varepsilon \approx 10\%$, from a combination of analytical analysis and observational constraints (Soltan, 1982; Ueda et al., 2003; Elvis et al., 2002; Yu and Tremaine, 2002; Shapiro, 2005). Therefore, if a $100 M_\odot$ Pop III star is considered as a seed BH it would need to

²<https://eventhorizontelescope.org>

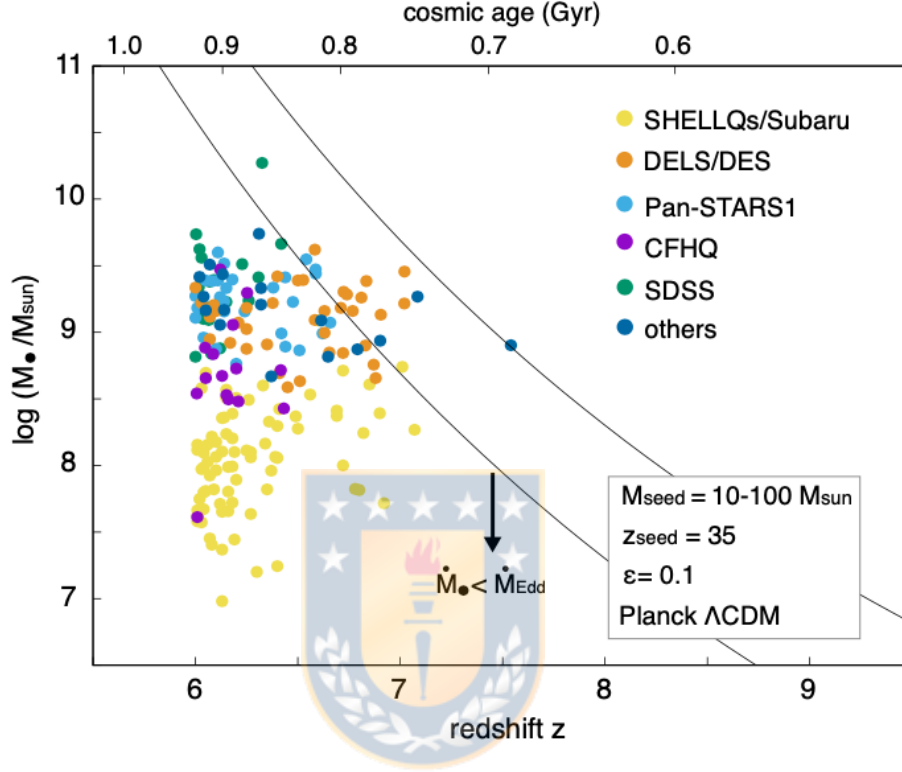


Figure 1.1.1: Masses and redshifts of 203 quasars known at $z \geq 6$. 79 of these 203 quasars are from Bañados 2016. 8 quasars from Pan-STARRS (Mazzucchelli et al. 2017, Tang et al. 2017, Koptelova et al. 2017, Bañados et al. 2018), 3 quasars from VIKING (Decarli et al. 2018, Venemans et al. 2019), 37 quasars from a combination of DES/SDSS, UKIRT, VISTA and WISE (Wang et al. 2016a, Reed et al. 2017, Wang et al. 2017, Reed et al. 2019, Wang et al. 2019, Fan et al. 2019b, Yang et al. 2019), 72 quasars from the SHELLQs and other Subaru surveys (Kashikawa et al. 2015, Matsuoka et al. 2018a,b, 2019b,a) and 4 quasars from a combination of VST-ATLAS and WISE (Carnall et al. 2015, Chehade et al. 2018). Here the masses were estimated from the rest-frame UV luminosity, assuming a constant bolometric correction and Eddington ratio of $f_{\text{Edd}} = 1$. The two black curves illustrate the mass of a BH as a point of comparison. Starting from a seed BH of stellar mass $M_{\bullet} = 10 M_{\odot}$ (lower curve) or $100 M_{\odot}$ (upper curve) at $z = 35$, the mass of a BH constantly increases at the Eddington rate, with a radiative efficiency of $\varepsilon = 0.1$. From Inayoshi et al. (2020).

accrete for ≈ 0.8 Gyr to reach $10^9 M_{\odot}$ if the accretion complies with the relevant Eddington limit. This timescale is comparable to the age of the Universe at $z \approx 6$. If these SMBHs accrete only at sub or near-Eddington rates (Willott et al., 2010; Mazzucchelli et al., 2017; Onoue et al., 2019; Shen et al., 2019; Vito et al., 2019), we need very massive initial seeds of the order of at least $10^4 M_{\odot}$ to reach masses of $10^9 M_{\odot}$, especially when realistic spin parameters and accretion disc models are taken into account (Shapiro, 2005). So to explain the SMBHs that we see today the solutions are very massive seeds or extremely fast growth in extended periods of super-Eddington accretion, which are possible in non-spherically symmetric situations where the Eddington rate can be exceeded, or most likely a blend of the two processes.

1.2 Formation mechanisms of supermassive black holes at high redshift

This chapter provides an overview of the three main pathways for the formation of SMBHs at high redshift originally proposed by Rees (1984), which are: i) Pop III stellar remnants (Bromm et al., 2002; Abel et al., 2000; Yoshida et al., 2006; Gao et al., 2007; Hirano et al., 2014; Hirano et al., 2015; Bowman et al., 2018; Hosokawa et al., 2013; Schleicher et al., 2013; Umeda et al., 2016; Heger et al., 2003; Haemmerlé et al., 2018; Haemmerlé, 2020, 2021), ii) the collapse of a protogalactic gas cloud into a massive black hole or a very massive star, that collapses into a black hole, due to peculiar conditions such as a strong radiation background that photodissociates molecular hydrogen and prevents strong fragmentation of the gas cloud (Bromm and Loeb, 2003; Wise et al., 2008; Latif et al., 2013; Latif et al., 2015; Regan et al., 2017; Grete et al., 2019; Suazo et al., 2019; Chon and Omukai, 2020; Latif et al., 2021), and iii) relatively massive black hole seeds formed in dense stellar clusters via dynamical processes like runaway collisions (Devecchi and Volonteri, 2009; Katz et al., 2015; Yajima and Khochfar, 2016; Sakurai et al., 2017; Reinoso et al., 2018; Vergara et al., 2021; Escala, 2021). We will show a description of the main components that these models must have, including previous work and how previous results support the model that we study in this thesis. Fig. 1.2.1 shows three potential ways to explain the formation of SMBHs in the early Universe considering a critical metallicity and the presence of few

metals.

The presence of SMBHs at $z = 6 - 7$ has led to the development of several theories about their formation to alleviate timescale constraints and help explain their existence. One possibility is that a small fraction of early Pop III seeds may maintain Eddington accretion for most of the history of the Universe. This scenario is unlikely for stellar mass seeds formed in shallow minihalo potentials due to negative feedback processes like radiation and supernova feedback, but may be possible in rare situations of massive halos with $\gtrsim 10^8 M_{\odot}$. Another alternative option is that BH seed formation could be accelerated if a significant time period of growth was due to mergers of compact objects, primarily other BHs. However, one potential problem is that BH mergers can lead to gravitational wave-induced kicks that remove BHs from their gas reservoirs (Haiman, 2004).

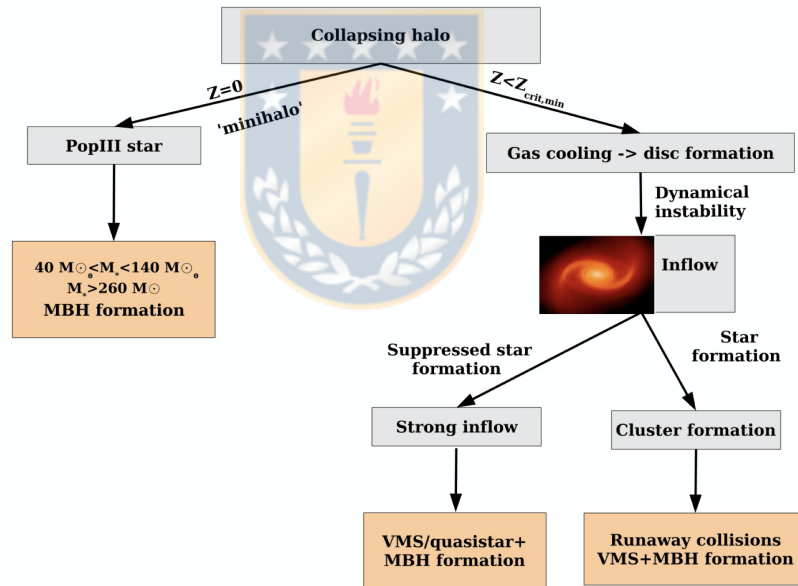


Figure 1.2.1: The image shows three potential ways that SMBH seeds were created in the early Universe. The left-hand route shows how the initial generation of stars collapsed, which were formed from gas with the expected abundances after recombination ($Z = 0$). Alternatively on the right side, both of these scenarios require the presence of few metals ($Z < Z_{\text{crit}}$) in a gas cloud that will form a disc as it cools and then a star cluster that may experience a runaway collision process producing a massive star or black hole. However if star formation is suppressed, a strong inflow of gas is anticipated at the center of the cloud, creating a supermassive star or an IMBH. From Volonteri (2010).

1.2.1 Direct collapse scenario

The most promising scenario to explain the formation of SMBH seeds is via the so-called direct collapse black holes (DCBH) (Rees, 1984; Volonteri and Rees, 2005; Ferrara et al., 2014), where the main idea is the formation of a supermassive star (SMS) with a mass $M \sim 10^5 M_\odot$, which then promptly collapses to a BH with a similar mass. This scenario requires a rapid collapse of the primordial gas in an atomic cooling halo (ACH) with virial temperature $T_{vir} \sim 10^4$ K, which is a metal-free gas and where the formation of molecular hydrogen remains suppressed because the high temperature does not allow the formation of \mathbf{H}_2 . An important ingredient to form a SMS is a rapid accretion rate ($\sim 0.1 - 1.0 M_\odot/\text{yr}$), which requires collapsing warm gas ($\gtrsim 5000$ K).

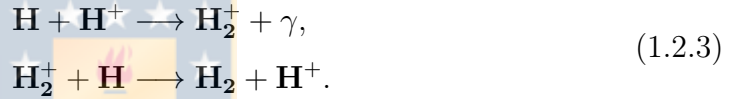
If we consider that accretion is regulated by the self-gravity of the gas, there is the following relationship between the mass inflow rate of a self-gravitating collapsing gas \dot{M} and its thermodynamical characteristics:

$$\dot{M} \sim \frac{M_J}{t_{ff}} \sim \frac{c_s^3}{G} \sim 0.1 M_\odot/\text{yr} \left(\frac{T}{8000 \text{ K}} \right)^{3/2}, \quad (1.2.1)$$

while the Jeans mass M_J is an estimate of the mass of a collapsing gas cloud, t_{ff} the free fall time of the gas cloud, T the gas temperature and c_s the sound speed. From this equation we can see that the accretion rate \dot{M} and the Jeans mass M_J depend strongly on the temperature of the gas and increase with temperature, i.e. the higher the temperature, the higher is the mass inflow. Therefore, the thermodynamic requirement to avoid a large drop in mass is that the gas does not cool to lower temperatures, since then it fragments and will form normal stars. As we know, the chemical composition of the primordial gas determines its cooling, specifically the abundance of \mathbf{H}_2 . In this scenario, the cooling caused by molecular hydrogen can cause the temperature of the gas to fall to ~ 200 K and induce star formation. Conversely, in the absence of molecular hydrogen, the gas remains in its atomic phase and cools mainly through atomic line radiation, maintaining a temperature of ~ 8000 K. So to keep the gas warm, it is necessary to avoid cooling and efficient fragmentation by metals or \mathbf{H}_2 during the collapse of a massive gas cloud. With numerical simulations it has been shown that this can be achieved when a strong radiation background photodissociates the molecular

hydrogen (Bromm and Loeb, 2003; Wise et al., 2008; Latif et al., 2013).

To study the cooling processes of the gas cloud, we need the chemical reactions for the formation of \mathbf{H}_2 in the primordial gas. Two possible ways have been identified to form \mathbf{H}_2 in primordial gas; via the intermediaries \mathbf{H}_2^+ or \mathbf{H}^- , where \mathbf{H}^- is relevant in the collapse of high-redshift objects (Peebles and Dicke, 1968; Hirasawa, 1969; Matsuda et al., 1969). We can see these chemical reactions in the following equation:



\mathbf{H}_2 can be dissociated through several mechanisms including the exposure of ACHs to \mathbf{H}_2 photodissociating UV radiation in Lyman-Werner (LW) bands (Omukai, 2001; Oh and Haiman, 2002; Bromm and Loeb, 2003), suppressed \mathbf{H}_2 cooling (Fernandez et al., 2014), heating the gas or a combination of both (Yoshida et al., 2003; Wise et al., 2019). In particular, we will introduce three distinct mechanisms that could keep the \mathbf{H}_2 fraction at low levels.

1.2.1.1 Photodissociation of \mathbf{H}_2 by LW radiation

\mathbf{H}_2 can be photodissociated by radiation with soft UV photons, in a two-step dissociation process. The photons in the range of $\approx 11 - 15$ eV are absorbed in the LW lines of \mathbf{H}_2 . Approximately $\sim 10\%$ of the excited \mathbf{H}_2 radiatively decay into the split state of two \mathbf{H} atoms, resulting in the dissociation of \mathbf{H}_2 by the so-called Solomon process,





Haiman et al. (1997); Ciardi et al. (2000) found that the first generations of stars (Pop III and Pop II) and BH remnants emitted LW radiation. Due to the large free path for photons with energies < 13.6 eV, it was possible to form a LW background in the early Universe, capable to suppress the formation of \mathbf{H}_2 in low-mass DM halos. The competition between the formation and dissociation timescales defines the critical value of the UV flux, above which the formation of \mathbf{H}_2 remains quenched. Depending on halo mass and redshift, the resulting critical intensity is $J_{crit} \approx (0.01 - 1)$, where the flux is expressed in units of $J_{21} \equiv 10^{21} \text{ erg s}^{-1} \text{ cm}^2 \text{ Hz}^{-1} \text{ sr}^{-1}$ (Haiman et al., 2000; Machacek et al., 2001; Wise and Abel, 2007; O'Shea and Norman, 2008). Therefore, a significant number of minihalos may not contain \mathbf{H}_2 and may not form any stars (Omukai and Nishi, 1999; Haiman et al., 2000; Ciardi et al., 2000; Mesinger et al., 2006).

The problem occurs when we try to calculate the value of J_{crit} for more massive minihalos; for example for "sub-atomic" minihalos ($\sim 10^6 M_\odot$) J_{crit} increases to $\gtrsim 100$ (Regan et al., 2017), due to \mathbf{H}_2 self-shielding. So for ACH the problem is even larger because a very high UV flux is needed to dissociate \mathbf{H}_2 and to prevent its further formation. A higher J_{crit} is necessary since for more massive ACH the density increases ($n_H \approx 10^4 \text{ cm}^{-3}$ (Wolcott-Green and Haiman, 2019)) and J_{crit} depends on the density n_H as $J_{crit} \sim n_H$, since J_{crit} is obtained by balancing the dissociation rate ($\propto J_{LW} n_H$) with the formation rate ($\propto n_H^2$).

In one-zone models which adopt the most up-to-date chemical network, and considering realistic incident spectral shapes from low-metallicity galaxies, one finds $J_{crit} \approx (1000 - 1400)$ (Sugimura et al., 2014) (see also, Agarwal and Khochfar (2014)). Applying it in cosmological simulations we get much larger critical values of the order of 10^4 to 10^5 (Latif et al., 2014; Latif et al., 2015). Adopting the shielding factors from Wolcott-Green et al. (2011), Latif et al. (2015) found a value of J_{21} for spectra of Pop II stars through three-dimensional cosmological simulations and one-zone models, varying the radiation spectra. They found $J_{crit} \approx (2 - 5) \times 10^4$ (see Fig. 1.2.2).

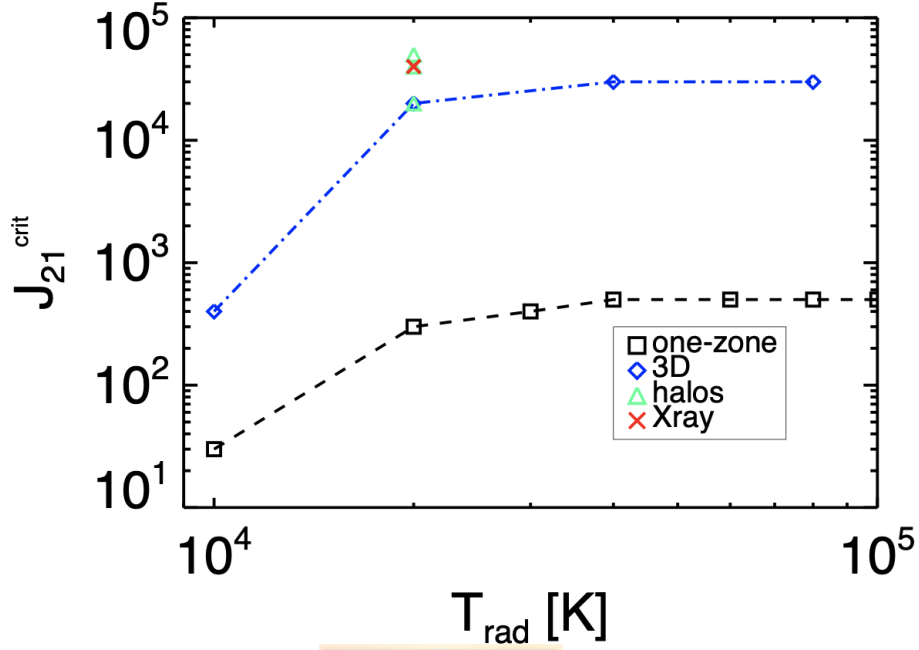


Figure 1.2.2: Conditions for the direct collapse scenario, where the lines represent the radiation flux required to destroy and suppress the formation of H_2 molecules in a $10^7 M_\odot$ gas cloud. The black and blue dashed lines represent one zone and 3D models, along with a red cross including an X-Ray ionization background which however makes little difference. From [Latif et al. \(2015\)](#).

The need for large values of J_{21} that are only possible in rare situations such as in the proximities of a star-forming galaxy, where most of the closest stars must be Population II stars, provides a problem for the direct collapse model ([Dijkstra et al., 2014](#)), since in order to accurately estimate the number of ACHs where seed SMBHs might grow, knowledge of J_{crit} is essential and such large fluxes may not occur frequently enough to explain the observed supermassive black holes ([Dijkstra et al., 2008](#); [Johnson et al., 2012](#)).

1.2.1.2 H^- photodetachment

Due to the lack of strong LW lines, low-energy near-IR and optical photons with energies below $< \sim 11$ eV cannot effectively dissociate H_2 via LW line absorption, but they can indirectly inhibit H_2 production via H^- photo-detachment,



Several studies have calculated J_{crit} assuming a blackbody shape with temperatures of $T \approx 10^5$ K and $T \approx 10^4$ K. For $T \approx 10^4$ K the value of the critical intensity is $10^4 < J_{crit} < 10^5$ and for a temperature of $T \approx 10^5$ K the critical intensity is $J_{crit} \gtrsim 10^5$ (Omukai, 2001; Bromm and Loeb, 2003; Shang et al., 2010).

1.2.1.3 Collisional \mathbf{H}_2 dissociation

Collisional dissociation of \mathbf{H}_2 (the chemical reaction is denoted as Equation 1.2.7) for the formation of BH seeds may be important in hot ($T \approx 8000$ K) and dense regions ($n_H \gtrsim 10^4 \text{ cm}^{-3}$) (Inayoshi and Omukai, 2012). In such regions \mathbf{H}_2 is efficiently collisionally dissociated and defined as the "zone of no return". According to Mayer et al. (2010, 2015); Inayoshi et al. (2015) these regions can be formed through colliding flows in the centers of protogalaxies and/or violent collisions of the galaxies themselves.



Fernandez et al. (2014), in cosmological simulations, confirmed the idea that it is possible to suppress \mathbf{H}_2 formation by collisional \mathbf{H}_2 dissociation, but only if \mathbf{H}_2 formation is artificially suppressed with a high UV background, to allow that the gas in the center of the halo enters the high-temperature and high-density regime, the "zone of no return," where it will remain even if the UV background is turned off, collapsing isothermally. They noted that for ACH with $T_{vir} \approx 80000$ K (atomic cooling threshold), the model is not feasible. However for more massive halos ($T_{vir} > 10^4$ K) the colliding fluxes can still produce high temperatures and densities in the core.

1.2.2 Supermassive black holes from Pop. III stars and supermassive stars

Another mechanism for the formation of SMBH seeds is based on the remnants of the first generation of stars, formed out of zero metallicity gas. The first stars are formed in minihalos with masses $\sim 10^5 - 10^6 M_\odot$ at $z \sim 20 - 25$, where the mass of these minihalos is mainly composed of dark matter, hydrogen and helium. The main cooling mechanism is molecular hydrogen. We note that the typical stellar mass in the early Universe was more massive than we can observe today. This is

because in the early Universe the temperatures of the star formation zones were higher (~ 300 K) than we can observe today (~ 10 K). Therefore, due to these high temperatures, the thermal pressure, and therefore, the Jeans mass of the gas clouds were enhanced by a factor ~ 100 . We recall that the Jeans Mass is the critical mass of a gas cloud above which it becomes gravitationally unstable and collapses

$$M_J = \frac{4}{3}\pi\rho\left(\frac{1}{2}\lambda_J\right)^3 = \frac{\pi^{5/2}}{6}\frac{c_s^3}{\sqrt{G^3\rho}}, \quad (1.2.8)$$

where ρ is the gas density, λ_J the Jeans length, G the gravitational constant and c_s the sound speed. We expect that in the early Universe the typical mass of the Pop III stars was $\sim 100 M_\odot$ (Bromm et al., 1999, 2002; Abel et al., 2000; Yoshida et al., 2006; Gao et al., 2007). So one candidate for the initial seed BHs for rapid accretion are remnants formed through massive Pop III stars (Carr et al., 1984).



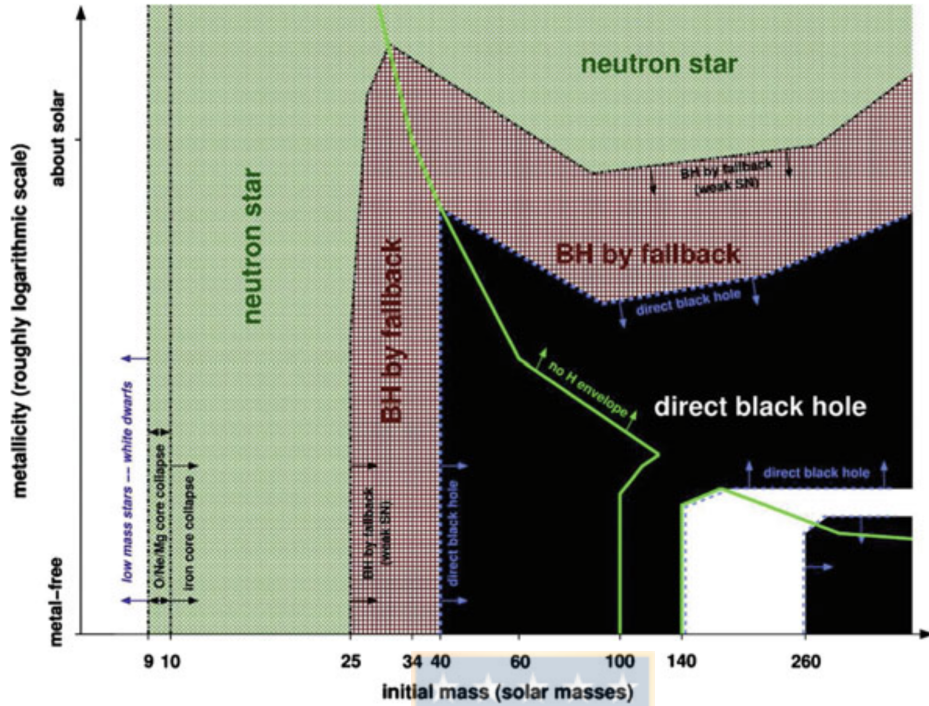


Figure 1.2.3: Final fate of massive single stars as a function of the initial metallicity and initial mass. The green line separates the regimes where the stars keep their hydrogen envelope (left and lower right) from those where the hydrogen envelope is lost. The dashed blue line indicates the border of direct black hole formation (black region). At lower masses and higher metallicities is the regime of BH formation by fallback (red zone) and the green zone indicates the formation of neutron stars. Also note that the white zone between the BH formation zones is a strip of pair-instability supernovae that leave no remnant. From [Heger et al. \(2003\)](#).

The final fate of the remnants of single massive stars depends on their mass. In [Fig. 1.2.3](#), we can see an illustration of the final fate of primordial stars depending on their initial metallicity and initial masses, where each zone represents different remnants of the individual massive stars, with the black region indicating direct BH formation, the red region indicating BH formation via fallback formation, the red region neutron star formation ($9 - 10 M_{\odot}$) and the white region represents a region where no remaining BH is obtained. Low metallicity stars in the mass range of $25 - 140 M_{\odot}$ are expected to form BHs directly, where the final mass would be about half of the mass of the star, $\sim 10 - 25 M_{\odot}$ for stars between $25 - 140 M_{\odot}$ ([Zhang et al., 2008](#)). For stellar masses between $140 - 260 M_{\odot}$ pair-instability supernovae with helium core masses are expected to occur, so a BH would not

be obtained.

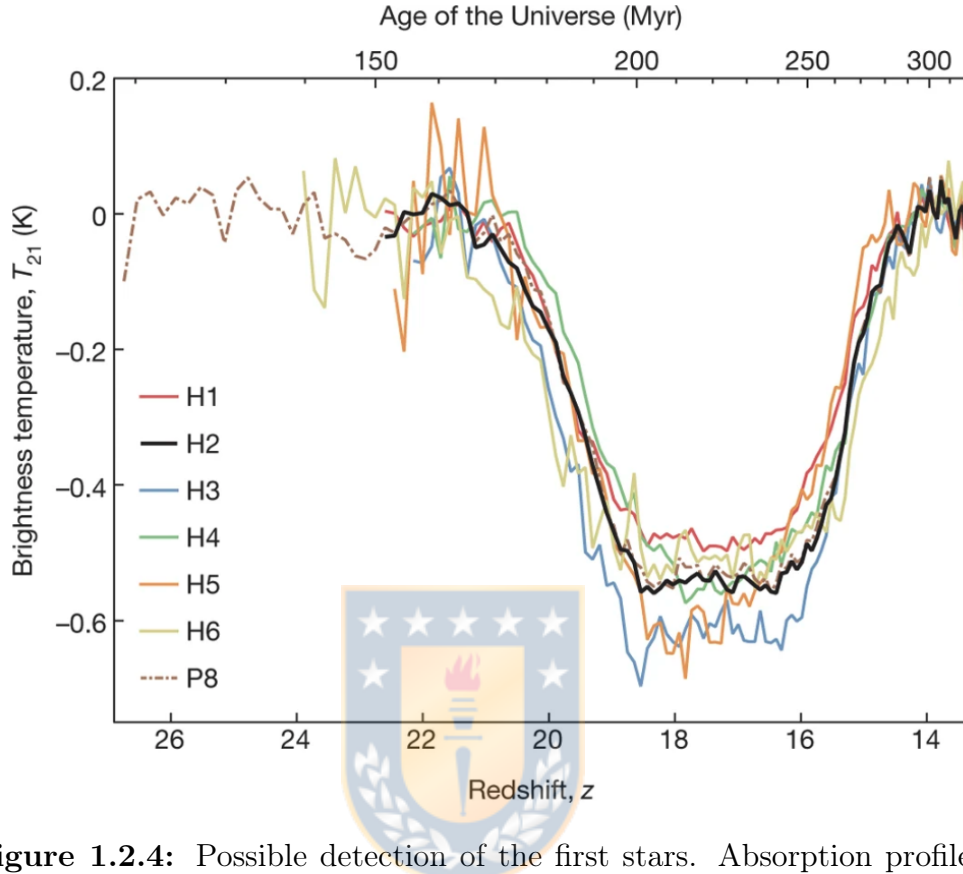


Figure 1.2.4: Possible detection of the first stars. Absorption profile of the 21 cm line plotted against the redshift and the age of the Universe. The signal is absorbed due to the change of the spin of the \mathbf{H} atoms that are around the first stars. The black solid line is the best fit for the hardware and software configurations which yields the best signal-to-noise ratio. From [Bowman et al. \(2018\)](#).

Both observational detections and cosmological simulations appear to be in agreement with existing models for the formation and properties of these stars. Fig. 1.2.4 shows the detections from the EDGES experiment, with the first global detections of these stars via radio observations (this needs further study, given the larger than expected amplitude of the signal), with a very strong absorption feature at $z \approx 20$ followed by rapid heating at $z \approx 16$. The Fig. 1.2.5 shows cosmological simulations of early structure formation, where the evolution of 1540 star-forming gas clouds is followed.

The calculations were performed using 3D simulations that include all pertinent cooling mechanisms for both \mathbf{H}_2 and \mathbf{H} . In their cosmological simulations the star

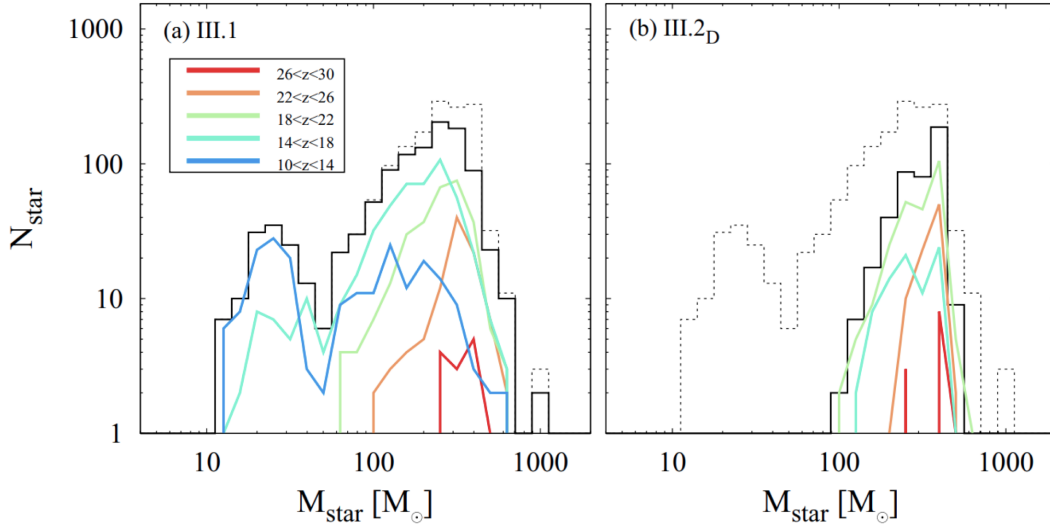


Figure 1.2.5: Resulting mass distributions of Pop III.1 (left) and III.2D (right) stars for different redshifts. The different colours represent different redshift ranges. The black solid lines show the total distributions over all redshifts for each population and the dotted lines show the sum of them. From [Hirano et al. \(2015\)](#).

formation is characterized by different star populations, the so-called Population III.1 stars and Population III.2D stars, which are primordial stars formed under the influence of far-ultraviolet radiation. Mainly through the efficiency of different types of cooling, depending on the densities reached at different stages of the evolution, it is possible to reach a density of $\sim 10^{16} \text{ cm}^3$ with a temperature of $\sim 3000 \text{ K}$. At this point the cloud becomes completely opaque and forms an adiabatic core, giving birth to a central protostar with a mass of $\sim 0.2 - 0.07 M_{\odot}$. The simulations show high accretion rates $\dot{M} \sim 10^{-3} - 10^{-2} M_{\odot}/\text{yr}$. After this the protostar grows to a SMS ($\gtrsim 10^5 M_{\odot}$) via rapid accretion, it eventually collapses through the general relativistic instability and becomes a SMBHs seed at high redshift ([Janka, 2002](#)).

We can see that the capacity to form a SMS depends to a great extent on the accretion rate. [Hosokawa et al. \(2012, 2013\)](#) have studied the evolution of protostellar radii at different accretion rates $\dot{M} \sim 10^{-6} - 6 \times 10^{-3} M_{\odot}/\text{yr}$ through a spherical model. They found that for Pop III stars with accretion rates $\dot{M} \approx 10^{-3} M_{\odot}/\text{yr}$ the star initially expands as it gains mass, then when it reaches a mass of $M \sim 10 M_{\odot}$ it contracts by radiative diffusion cooling (Kelvin-Helmholtz contraction). On the other hand, for higher accretion rates $\dot{M} \gtrsim 0.03 M_{\odot}/\text{yr}$ the protostar does not experience any Kelvin-Helmholtz contraction and continues

to expand steadily (Hosokawa et al., 2012, 2013). Since the ionizing flux in an inflated atmosphere is considerably reduced due to its temperature ($T \sim 5000$ K), the accretion rates are not diminished by UV feedback which could lead to masses of $100 M_{\odot}$ or higher (Hirano et al., 2014; McKee and Tan, 2008; Hosokawa et al., 2011). This effect is relevant only when the mass reaches $M \gtrsim 10^5 M_{\odot}$ where the GR instability induces collapse (Hosokawa et al., 2013).

If a SMS exceeds a certain critical mass M_{GR} , it will collapse directly to a BH through the GR instability (Chandrasekhar, 1964; Zeldovich and Novikov, 1971; Shapiro and Teukolsky, 1983). The critical mass is of the order of $\sim 10^5 - 10^6 M_{\odot}$, depending on the properties of the star. Recent studies suggest that rapid mass accretion onto SMSs drastically changes their stellar structure (Hosokawa et al., 2013; Haemmerlé et al., 2018). Also Umeda et al. (2016) found that the critical mass M_{GR} increased monotonically with the stellar accretion rate (see also Woods et al. (2017)).

1.2.3 Massive black holes via runaway collisions in a dense star cluster

An alternative pathway to the mechanisms mentioned above is the formation of a BH seed through runaway collisions, which has been less investigated in the early Universe. The main idea of the model is that a very massive star (VMS) could be formed through repeated stellar collisions and mergers; then if the star is massive enough, it can collapse into an intermediate mass black hole (IMBH).

Fragmentation cannot be avoided in the presence of a modest amount of metals or dust grains (Schneider et al., 2006; Clark et al., 2008; Omukai et al., 2008; Schneider and Omukai, 2010; Bovino et al., 2014; Peters et al., 2014; Grassi et al., 2017) or even for a metal-free gas; the formation of a stellar cluster is thus a much more likely outcome than a single central object.

Dense environments are especially favorable for runaway collisions. Compared to galaxies formed today, higher densities were reached in the early Universe, so it is possible that the first star clusters were denser than those observed today. In our local Universe the most extreme stellar systems can reach densities of $\sim 10^5 M_{\odot}/\text{pc}^3$ (Espinoza et al., 2009), where it is expected that collisions and stellar mergers will be recurrent. In the early Universe fragmentation can occur at

very high densities like $n_{\text{H}} \sim 10^{11-13} \text{ cm}^3$ for metal-poor gas clouds ($Z \gtrsim 10^5 Z_{\odot}$), leading to initial fragment masses of around $\sim 0.5 M_{\odot}$. Therefore these gas clouds can result in ultradense clusters of low-mass stars (Omukai et al., 2008; Devecchi and Volonteri, 2009; Schleicher et al., 2022). Finally due to these extreme densities of $\sim 10^{9-11} M_{\odot}/\text{pc}^{-3}$ clusters can undergo core collapse, leading to a fraction of non-negligible runaway stellar collision resulting in central IMBHs with a mass of up to $\sim 10^4 M_{\odot}$.

Studies found that the conditions for runaway collisions are more favorable in dense and massive clusters once they experience core collapse due to changes in the kinetic energies triggered by close stellar encounters within the cluster (Lynden-Bell and Wood, 1968; Cohn, 1979; Spitzer, 1987; Breeden et al., 1994). Baumgardt and Klessen (2011) conducted a study evaluating the importance of collisions in current protostellar clusters, discovering that 0.1 – 1 % of protostars collide in typical clusters. This implies that for a sufficiently large number of stars collisions could be potentially more important. Similar investigations have been pursued by Moeckel and Clarke (2011); Oh and Kroupa (2012); Fujii and Portegies Zwart (2013); Bonnell et al. (1998); Clarke and Bonnell (2008) showing that collisions are also important for the formation of massive stars.

Once the cluster has been formed, the most massive stars tend to sink towards the center due to energy equipartition, which increases the collision probability in the cluster, since in the center there is a higher densities of massive stars and the cross sections of these stars are much larger than for their lower-mass counterparts, thus favoring collisions. After a collision the cross section of the new star is even larger, which leads to higher probabilities of future mergers. This is a runaway process, because once stars collide so their masses and radii increase, therefore their cross sections causes the subsequent collision rate to grow. The star cluster will continue to evolve normally without many more collisions, once the timescale of the collisions is longer than the lifetime of the VMS in the main sequence. Finally, depending on its mass and metallicity, the VMS collapses directly to an IMBH with minimal mass loss (Heger et al., 2003).

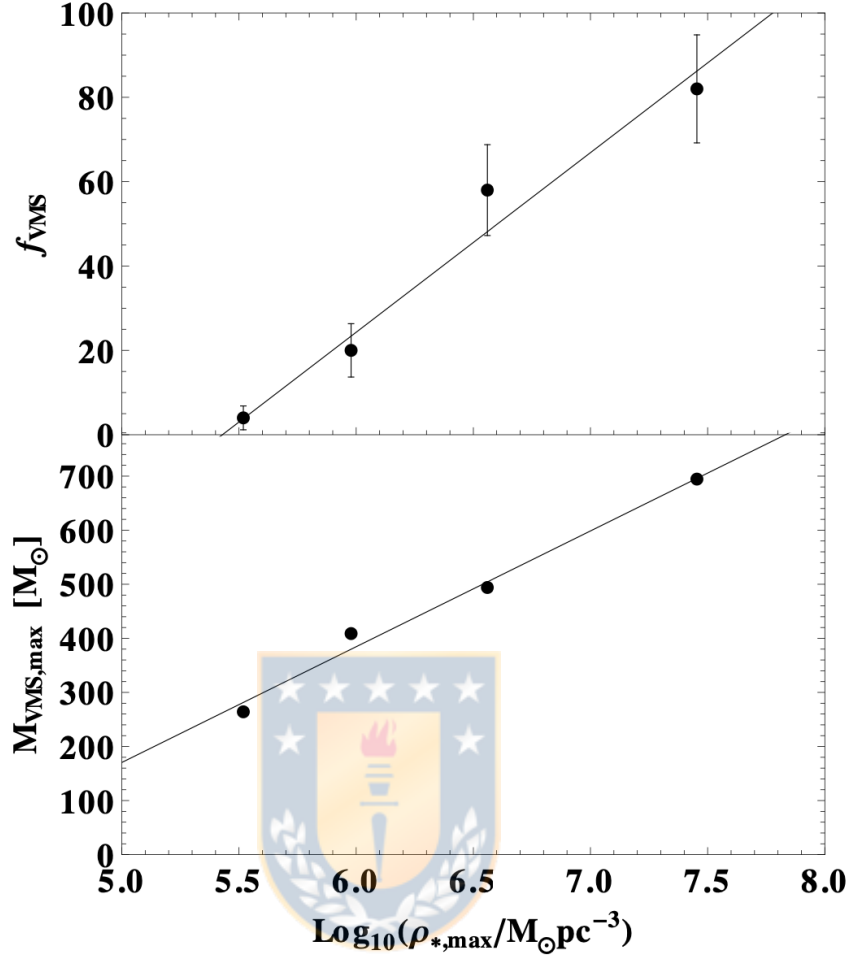


Figure 1.2.6: Percentage of realizations which produce a VMS (f_{VMS})(top) and the most massive VMS ($M_{\text{VMS,max}}$)(bottom) as a function of the initial central stellar mass density for the top-heavy Salpeter IMF assuming $S = 0$ and $b = 0$. From [Katz et al. \(2015\)](#).

[Katz et al. \(2015\)](#) showed through a combination of high-resolution cosmological hydrodynamical zoom-in simulations and N-body simulations that it is possible to form a VMS with masses as high as $300 - 1000 M_{\odot}$ that can directly collapse to a intermediate-mass black hole, via stellar runaway collisions in the center of nuclear Pop. II star clusters at high redshift (where the neighborhood was enriched with metals by nearby companions). They also found that the initial mass and initial central density of the nuclear star cluster (NSC) has a significant impact on the eventual mass of the VMS that develops. This is clearly reflected in Fig. 1.2.6, where as a function of the initial central density, the mass of the most massive VMS that developed as well as the percentage of clusters that created a VMS is

shown. With an increase in the initial central density, the mass of the VMS and its formation probability both grow.

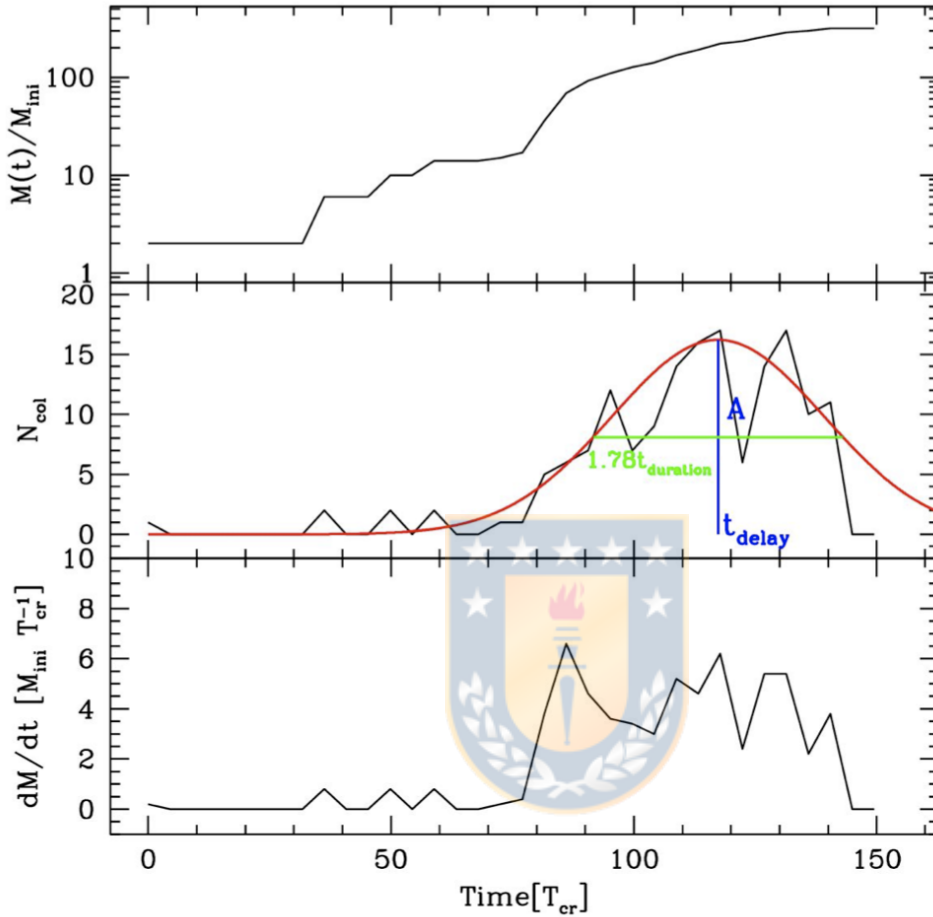


Figure 1.2.7: The top panel shows the mass evolution of the runaway star ($M_{\max}(t)/M_{\text{ini}}$) in a cluster with $N = 5000$ stars, where each star has an initial mass of $M_* = 2 M_{\odot}$ and an initial radius of $R_* = 200 R_{\odot}$. The middle panel shows the number of collisions (N_{col}) as a function of the crossing time of the cluster, and the red line is the best Gaussian fit. The bottom panel is the mass growth rate dM/dt in $M_{\text{ini}} T_{\text{cr}}^{-1}$. From [Reinoso et al. \(2018\)](#).

[Yajima and Khochfar \(2016\)](#) studied the formation of SMBH seeds through compact clusters that formed in mergers of the first galaxies. They show that these clusters are susceptible to core collapse and can generate VMSs of $\sim 1000 M_{\odot}$ in their centers. Then the VMS collapses into a BH and grows by swallowing $\sim 90\%$ of the stars in their neighborhood. Additionally, they discovered that the BH mass is sensitive to the radius and mass of the host star clusters, which control the core collapse and stellar relaxation time-scales.

Sakurai et al. (2017) from cosmological N-body simulations showed that in halos of $\gtrsim 10^7 M_\odot$ with star clusters of $\sim 10^5 M_\odot$ the masses of the most massive central star can become as high as $\sim 400 - 1900 M_\odot$ through collisions. Reinoso et al. (2018) studied in detail the collisions in massive Pop. III clusters, showing how the properties of the cluster affect the number of collisions and the mass of the most massive object. They showed that the resulting BHs could have masses up to $600 M_\odot$. In Fig. 1.2.7 we can see the results of the evolution of one of the simulations.

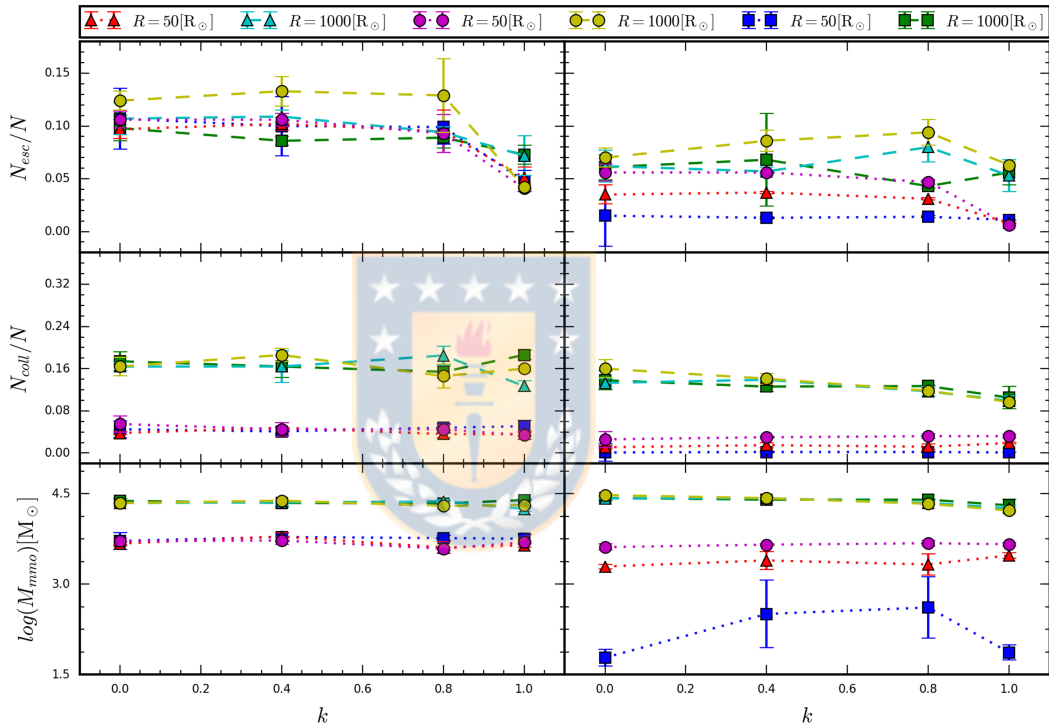


Figure 1.2.8: Evolution of different types of the shape of the model cluster (A, B, and C clusters) represented by triangles, circles, and squares, respectively, with $N = 10^3$ stars on the left side and $N = 10^4$ on the right side (for more information about the A, B and C cluster see Table 1 in Vergara et al. (2021)). Results are given for initial stellar radii $R = 50, 1000 R_\odot$ as a function of rotation factors (k -factor). Top panel: Normalized number of escaper. Middle panel: Normalized number of collisions with the most massive object. Bottom panel: Mass of the most massive object. From Vergara et al. (2021).

A more recent study is Vergara et al. (2021), who performed research on the dynamical evolution of flattened and rotating star clusters following a Miyamoto-Nagai distribution (Miyamoto and Nagai, 1975) via N-body simulations. They found that the collisions strongly depend on the number of stars and their initial

radii. Properties like rotation and flattening do not seem to have much impact on the number of collisions. However, as we can see in the top panel of Fig. 1.2.8 rotation helps to keep a larger number of stars in the system, thus reducing the number of escapers. We note that the escapers are constant for rotations $k = 0$, 0.4 , 0.8 , but decrease for $k = 1$.

1.3 Previous work

For BH formation also a 'hybrid' scenario is possible, which considers both gas-dynamical and star-dynamical processes; in particular the newborn dense star cluster may still be embedded in a dense gas cloud. It is known that the combination of these processes can favor the formation of massive objects (Baumgardt and Klessen, 2011). As we have seen before, due to accretion the radii of the protostars are increasing and so does the probability of collisions (Hosokawa et al., 2012, 2013; Schleicher et al., 2013). Likewise, the dynamics of runaway collapse can be favored by large gas flows that increase the gravitational potential, causing a higher probability of collisions (Davies et al., 2011).

Boekholt et al. (2018) explored the formation of SMBH seeds considering the interaction between stellar-dynamical and gas-dynamical processes, demonstrating the interaction of collisions with accretion in a compact primordial cluster within a primordial gas cloud. This was done through N-body simulations, considering a compact stellar cluster embedded in a gas reservoir simulated as a potential from which the protostars accreted mass. They defined 6 different models for the accretion rates, where the accretion depends on the gas availability and the position of the protostars (see Table 1 in Boekholt et al. (2018)). Fig. 1.3.1 shows the evolution of the most massive objects for the different accretion models, reaching a range of $\sim 10^4 - 10^5 M_{\odot}$. They concluded that the accretion-induced collisions in Pop. III clusters are a viable mechanism to explain SMBH seeds. Das et al. (2021b) studied the impact of analytical accretion rates such as Bondi-Hoyle-Lyttleton accretion, Eddington accretion and constant accretion, finding that the evolution of the system is highly sensitive to the initial conditions and the accretion recipe. The final SMS masses are $\sim 10^3 - 10^5 M_{\odot}$ for the three accretion scenarios considered.

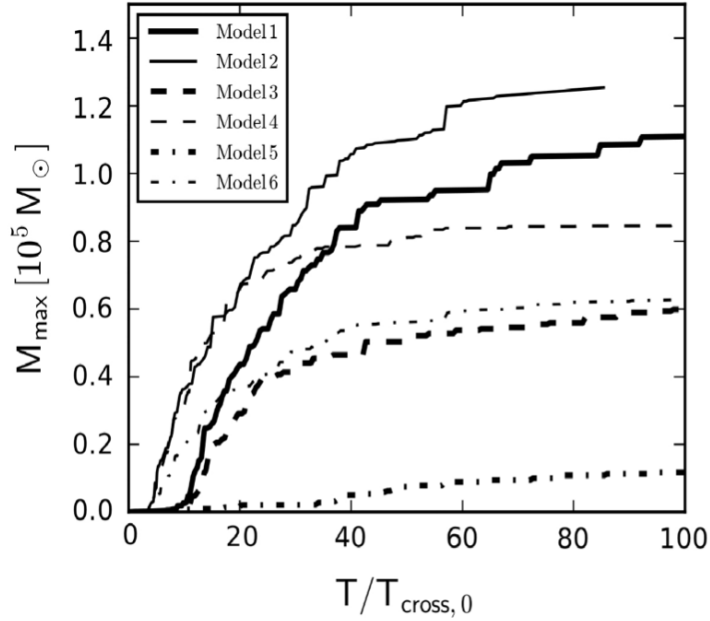


Figure 1.3.1: Time evolution of the maximum mass in the system, for six different accretion models and standard set of parameters. All models efficiently convert at least half of the initial gas mass into one single massive object, except for the model 5. From [Boekholt et al. \(2018\)](#).

Additionally [Alister Seguel et al. \(2020\)](#) has extended this analysis by including mass loss during collisions. This was done including both constant mass loss fractions and analytical models. They concluded that the mass loss strongly impacts the final mass of the SMBH seeds, in some cases losing between 60 - 80% of the final mass; nevertheless, masses of the order of $10^4 M_{\odot}$ were still obtained, being massive enough to be viable candidates for SMBH seeds (see also [Das et al. \(2021a\)](#), who analyzed the mass loss through stellar winds.)

In a recent study [Schleicher et al. \(2022\)](#) estimated the mass of the most massive central object (MMO) formed by collisions and accretion, where the extreme cases of a logarithmically flat initial mass function (IMF) and a Salpeter IMF were considered. They found that for cases where the radiative feedback is inefficient, masses of $10^4 M_{\odot}$ can be reached, while when the accretion time is limited by feedback it is possible have masses of $\sim 10^3 M_{\odot}$. Finally it is possible to form BHs with masses of $\sim 10^4 M_{\odot}$ or more. In Fig. 1.3.2, we can see a sketch of this new hybrid path for the formation of SMBH seeds.

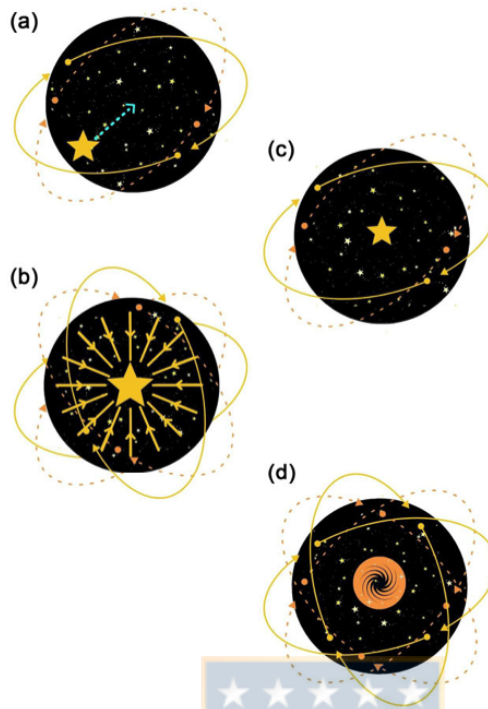


Figure 1.3.2: The expected evolution of the stellar cluster during the formation of a central massive object. At the times A-B the most massive star sinks to the center. At time C) the most massive star in the center accretes material through both stellar collisions and gas reservoir. Finally at time D) the supermassive star collapses into a very massive black hole. From [Schleicher et al. \(2022\)](#).

1.4 This project

In our investigation, presented in this thesis, we explore the evolution of a Pop. III star cluster embedded in a gas cloud with metallicity $Z < 10^{-5}$ incorporating a hydrodynamic treatment and exploring its sensitivity to different temperatures. This is a first exploration of the SMBH seed formation scenario through accretion and collisions incorporating a self-consistent hydrodynamic treatment and more sophisticated accretion routines. In addition, this work is an extension of the PhD. work realized by Bastian Reinoso where we provide a first investigation of the sensitivity of the evolution of the system (star cluster and gas cloud) at different temperatures and how it impacts the formation of a SMBH seed.

We present a description of the different formation scenarios of SMBHs in Chapter 1. The numerical methods as well as the codes and recipes used to perform our simulations are described in Chapter 2. In Chapter 3 we present our setup and the

development of the previous steps for its implementation. The main results are presented in Chapter 4. We summarize our work, providing the main conclusions and discussion in Chapter 5.



Chapter 2

Numerical Method

2.1 AMUSE

2.1.1 The AMUSE framework

To integrate the motion of the gas particles and the protostars in our star cluster, we use the Multi-purpose Software Environment (AMUSE) (Portegies Zwart et al., 2009; Portegies Zwart et al., 2013; Pelupessy et al., 2013; Portegies Zwart et al., 2018). AMUSE is a PYTHON framework which was designed for performing multi-physics simulations in which different existing codes from various domains in astrophysics can be coupled, allowing a complete study of different phenomena, as required here. The first version of AMUSE, called MUSE (Portegies Zwart et al., 2009a) was developed at Leiden Observatory under the supervision of Simon Portegies Zwart. AMUSE is free to download and there is a version of AMUSE on github that is available for debugging by the community where the users can ask for help related to the installation and the use of the software.

AMUSE provides a very simple PYTHON interface to existing codes, allowing computational tools for different physical domains and scales (see Fig. 2.1.1) to be easily combined into a single task. It also handles unit conversions so the user can focus more on the coupling strategies for performing multi-physics simulations.

AMUSE consists of a variety of community codes which are written in a variety of languages such as C, C++, Java and Fortran reflecting the programming backgrounds and preferences of their authors. These codes are usually free source

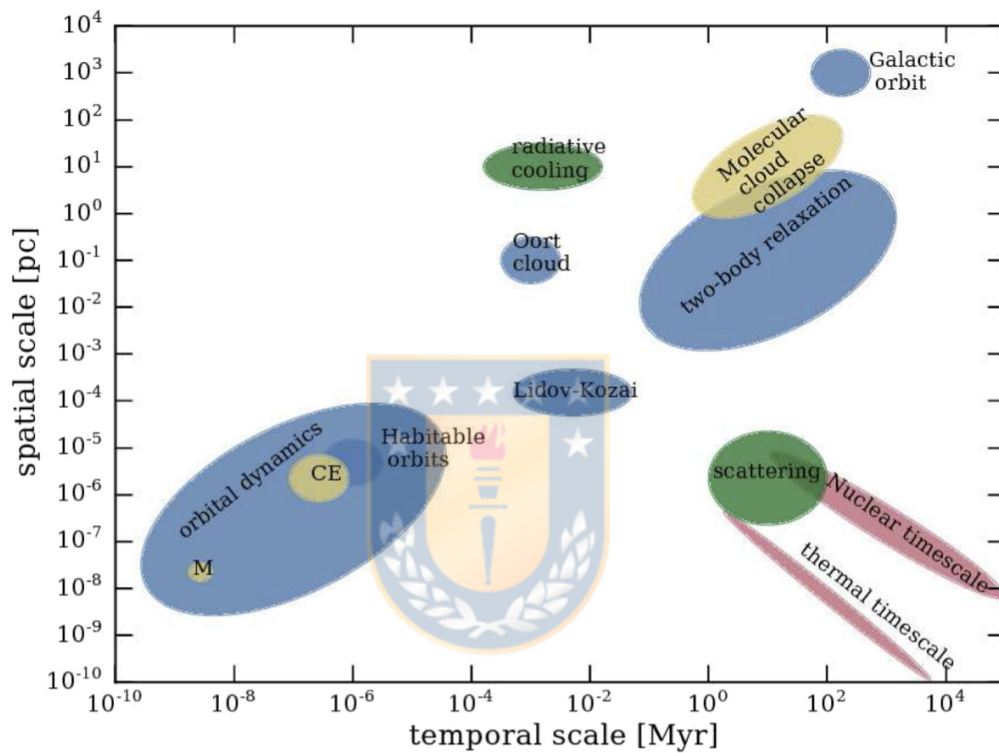


Figure 2.1.1: The physical domains of AMUSE represent typical temporal and spatial scales for a number of astronomical phenomena. The ellipses indicate specific astrophysical regimes, the colors indicate physical domains, where blue refers to gravity, red to stellar evolution, yellow to hydrodynamics, and green to radiative processes. Several domains are identified by name, such as the collapse of a giant molecular cloud (top right, in yellow), and the range of habitable planet orbits (blue circle at lower left). Gravity and hydrodynamics span a broad range of temporal and spatial scales, whereas radiative processes and stellar evolution exhibit much narrower ranges. Figure from [Portegies Zwart and McMillan \(2018\)](#).

codes such as PH4 or MESA. The community codes have two interface functions where the one on the AMUSE side is written in PYTHON and is called the proxy (they are loaded and initialized giving them the initial conditions with generic functions). The interface on the community code side is called the partner and is written in the native language of the code. These two interfaces communicate via the standard Message Passing Interface protocol (MPI, [Gropp et al. \(1996\)](#)) and SmartSockets ([Maassen and Bal, 2007](#)).

The AMUSE code has three functionalities:

1. A homogeneous, physically motivated interface for existing astronomical simulation codes.
2. The incorporation of multiple community codes from four fundamental domains (stellar evolution, gravitational dynamics, hydrodynamics, and radiative transfer).
3. The ability to design new simulation experiments by combining one or more of the community codes in various ways.

Parameters that depend on the community code are managed by the AMUSE framework, as are the acquisition and mining of simulation data. The fundamental physical solvers that can be combined in AMUSE are stellar dynamics, hydrodynamics, stellar evolution and radiative transfer. [Fig. 2.1.2](#) illustrates schematically the philosophy of AMUSE, with the central AMUSE framework surrounded by its four fundamental physical solvers. AMUSE can be extended by including other new hybrid codes combining community codes using PYTHON and domains, which can then be contributed to the AMUSE repository. The user can select from a variety of gravitational N-body solvers (symplectic N-body codes, direct N-body codes, and tree codes) by changing a single word in the script. The same holds for stellar evolution codes (parameterized and Henyey codes), hydrodynamics solvers (smooth particle hydrodynamics and adaptive mesh refinement codes), and radiative transfer codes (Monte Carlo photon transport codes, and tessellated photon flow solvers).

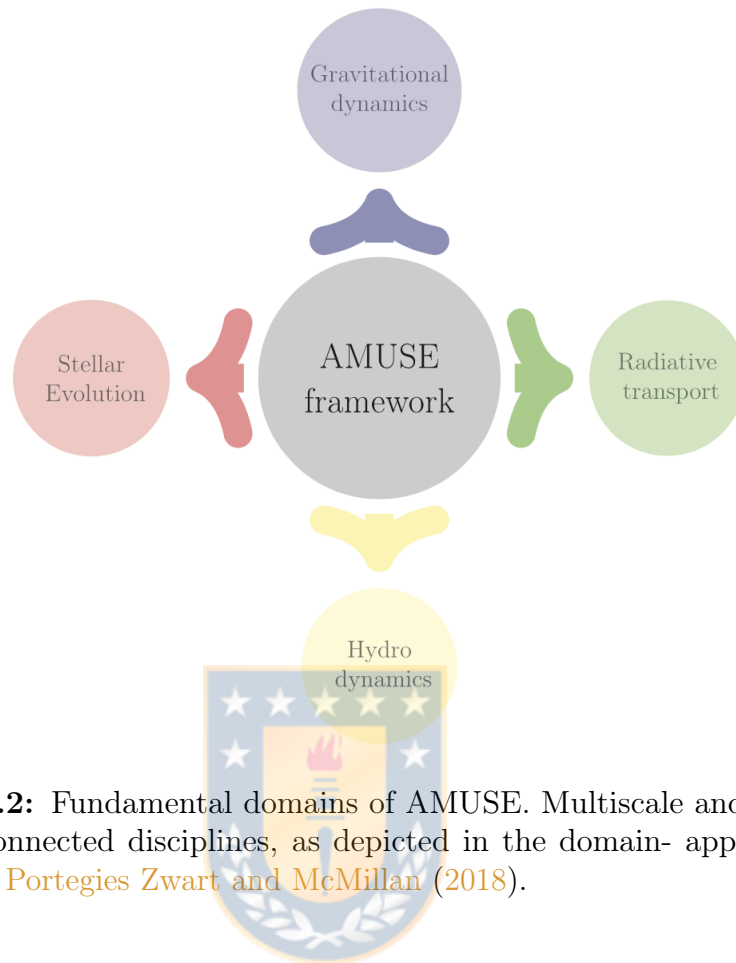


Figure 2.1.2: Fundamental domains of AMUSE. Multiscale and multiphysics codes are connected disciplines, as depicted in the domain- application plane. Figure from [Portegies Zwart and McMillan \(2018\)](#).

2.2 The Bridge Method

Many simulations entail combinations of physical domains with different length and time scales. Typically when two dynamical systems interact, the smaller system (having the smaller length or time scale) dictates the time resolution and time step, while the larger system (having larger length or time scale) consumes more resources, such as computer time, memory capacity, communication bandwidth, and storage space. These scale differences are often resolved with a semi-analytical model. In many dynamical cases, the spatial and temporal scales of the smaller and larger systems are well separated; then we can split the underlying Hamiltonian for the combined system into rapidly and slowly changing parts. The evolution of the two systems can then be followed by adopting a kick–drift–kick algorithm, allowing both scales to be integrated separately and the results to be combined into a consistent solution ([Portegies Zwart and McMillan, 2018](#)).

The BRIDGE method is a symplectic mapping for the gravitational evolution in

cases where the dynamics of a system can be split into different regimes. The method was first used by [Fujii et al. \(2007\)](#) to model a fully self-consistent N-body simulation of star clusters in their parent galaxy. The star clusters need high accuracy, while galaxies need a fast scheme because they consist of a large number of particles. Then the internal motion of the star cluster is calculated using a direct Hermite scheme with individual timesteps, the galaxy dynamics with the tree algorithm with a second-order leapfrog integrator and the interaction between the galaxy and the star cluster with the tree algorithm. The Hamiltonian of the system (the galaxy being the system A and the star cluster being the system B) is

$$H = \sum_{i \in A \cup B} \frac{p_i^2}{2m_i} + \sum_{i \neq j \in A \cup B} G \frac{m_i m_j}{|r_i - r_j|}. \quad (2.2.1)$$

The Hamiltonian can be separated as

$$H = \sum_{i \in A} \frac{p_i^2}{2m_i} + \sum_{i \neq j \in A} G \frac{m_i m_j}{|r_i - r_j|} + \sum_{i \in B} \frac{p_i^2}{2m_i} + \sum_{i \in B} G \frac{m_i m_j}{|r_i - r_j|} + \sum_{i \in A, j \in B} G \frac{m_i m_j}{|r_i - r_j|}, \quad (2.2.2)$$

$$H = H_A + H_B + H_{int}, \quad (2.2.3)$$

where H_A and H_B are the Hamiltonians of the subsystems A and B, respectively, and the interaction Hamiltonian H_{int} only depends on the separation of the systems. Therefore the main idea of the Bridge method is to perform a time evolution of the system A using a fast tree method and a more accurate time evolution of the system B using a direct method, whereas the interaction is treated as pure momentum kicks. In AMUSE we can use different codes for treating systems A and B, and these momentum kicks are computed with a Leapfrog scheme.

2.3 Hydrodynamics

Gas dynamical processes play an important role in the evolution of astrophysical systems on all scales from individual stars, the evolution of close binaries, the

interstellar medium in births and deaths of stars, flows onto neutron stars and black holes to larger scales where the gas is crucial for the formation of galaxies through cooling and heating processes.

To treat hydrodynamic effects, we generally use numerical techniques, since analytic treatments are restricted to problems with high degrees of symmetry or to situations where we can apply linear perturbation theory.

We can solve the hydrodynamical equation with two types of methods, the Eulerian and Lagrangian methods, each with advantages and disadvantages. The Eulerian methods use grid-based and finite volume schemes, where the equation of motion of a fluid can be resolved on a grid. A common approach are so-called [Godunov and Bohachevsky \(1959\)](#) schemes to solve the partial differential equations at the inter-cell boundary with conservative finite-volume method. The grid-based methods are not Galileo invariant, therefore we could have problems with Kelvin-Helmholtz or other shear instabilities. This can be resolved increasing the resolution and reducing the truncation error, though it is expensive in terms of computer resources. The main disadvantages of grid-based methods are the complexity of coding, optimization and large memory requirements.

On the other hand we have the Lagrangian methods, where we follow the motion of the fluid element when it moves through space and time. In the Lagrangian method the fluid is represented by particles and it preserves the Galilean invariance. The different properties of the particles that represent the fluid such as density, temperature, etc. are calculated by kernel estimation from nearby particles. The physical laws, such as Newton's laws, conservation of mass and energy, apply directly to each particle. Each particle can be smoothed due to the level of approximation and resolution necessary, hence, this method is generally known as Smoothed Particle Hydrodynamics, or SPH ([Gingold and Monaghan, 1977](#); [Lucy, 1977](#)).

The gas is modeled using the code Fi ([Hernquist and Katz, 1989b](#); [Portegies Zwart et al., 2009b](#); [Pelupessy et al., 2004](#); [Gerritsen and Icke, 1997](#)) which is a derivative of the N-body/SPH code TREESPH ([Hernquist and Katz, 1989a](#); [Gerritsen, 1997](#); [Bottema, 2003](#)). To resolve the self gravity, Fi calculates the gravitational forces using the Barnes-Hut algorithm ([Barnes and Hut, 1986a](#)).

2.3.1 Barnes-Hunt treecode

For the study of any astrophysical system one of the most important processes is gravity. In our system, gravity does not only affect the stellar component, but it also affects the self-gravitation of the gas and how it interacts with the stars. In general gravity affects any component with mass. It is important to have a consistent method to treat the gravitational interactions for gas, because in clusters the gaseous components could initially possess the largest amount of the total mass of the cluster.

Since we model gas as particles, we may be drawn to use one of the simplest solutions for calculating gravity, calculating the force through a direct sum of the pairwise gravitational forces. So to calculate the gravitational accelerations we use the Ph4 code as we do it for stars; however typical SPH simulations use thousands to millions of particles to model the gas consistently. Keeping this in mind, using a direct N-body code that needs $O(N^2)$ operations per force calculation is not viable. Therefore, for SPH simulations, an approximate method is needed, which sacrifices accuracy for speed.

One of the most widely used approximation methods, which also uses the FI code, is the Barnes-Hunt tree method (Barnes and Hut, 1986a). The basic idea of the method is that when calculating the force of the farthest particles, we do an approximation considering mass and quadrupole moment of the particle distribution, while for the closest particles we use direct summation.

The hierarchical organization of the particles is through a 3D oct-tree, i.e. the code decides for which of the distant particles it performs the approximation by consecutively dividing the space into eight zones (called parent nodes). Then, if a node contains more than one particle, the parent node is divided into eight children nodes of equal size until each child node contains only one particle. Note that empty nodes are dropped and the tree is built for each time step in the simulation.

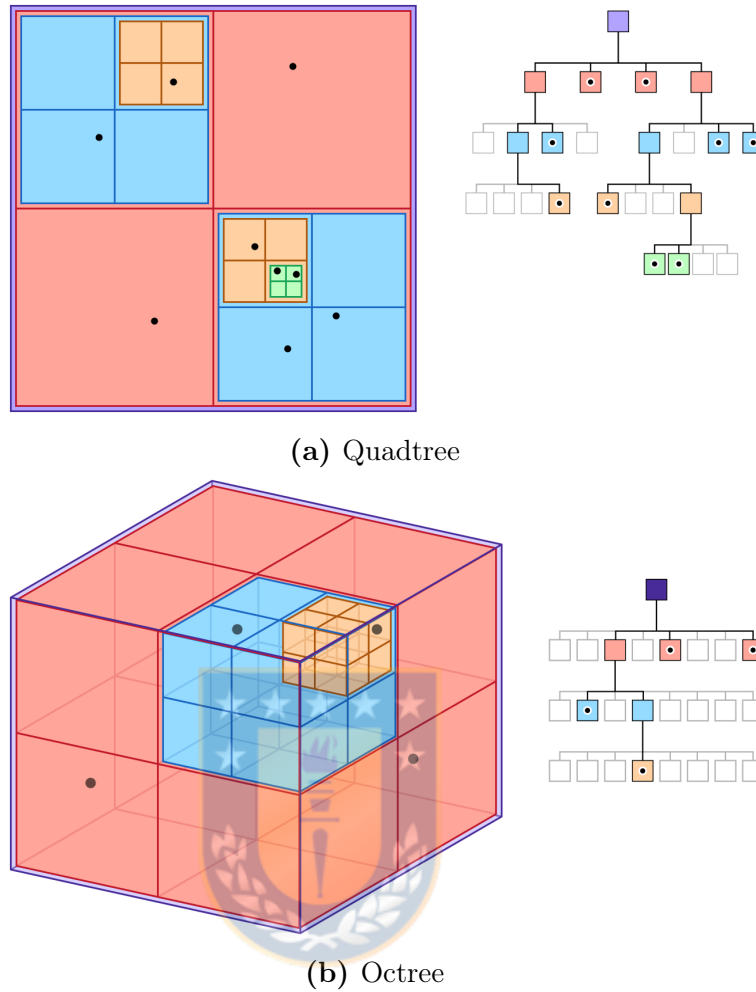


Figure 2.3.1: 2D y 3D example of the construction of the hierarchical tree. From Apple Developer Documentation.

The recursive opening of the nodes in the tree is conditional to a comparison of the size l of the node and the distance d to the center of mass of the node

$$\frac{l}{d} > \theta, \quad (2.3.1)$$

where θ controls the accuracy of the calculated gravitational force. If this criterion is passed, the force is calculated using the center of mass of the node, otherwise the node is opened and the formula 2.3.1 is evaluated on the children nodes recursively, see Fig. 2.3.1 for a example of the algorithm.

The Barnes-Hunt tree method has been widely used in numerical N-body simulations because the operations per force calculation are $O(N \log N)$ and the

method can be applied to any mass distribution as in cosmological simulations and star formation simulations. Salmon and Warren (1994) noted that the classical Barnes-Hunt opening criterion can fail. Later Springel et al. (2001) has shown that the 2.3.1 criterion could fail if the particles are subject to large canceling forces from the rest of the system and this will give large fractional force errors. The Fi code implements an alternative criterium proposed by Springel et al. (2001),

$$Ml^4 > \alpha |\mathbf{a}| d^6, \quad (2.3.2)$$

where M is the total mass contained in the node, α is the parameter controlling the accuracy of the force calculation and \mathbf{a} is an estimate of the acceleration, which in practice corresponds to the acceleration of the last time step.

2.3.2 Smoothed Particle Hydrodynamics Method

As we have seen in SPH we use a Lagrangian representation and the fluid is modeled as a collection of fluid elements. We select a set of N fluid elements which are represented by particles. Here the method assumes that the particle mass density is proportional to the mass density of the fluid ρ . So, according to the laws of hydrodynamics, ρ can be estimated from the local density of particles.

If the domain is not yet discretized into particles, the mean value of a physical field can be determined by

$$\langle f(r) \rangle = \int_{\Omega} f(r') W(r - r', h) dr', \quad (2.3.3)$$

where Ω is the domain of the neighbor particles, $W(r - r', h)$ is the smoothing kernel and h is the smoothing length that defines the length of the kernel function. The kernel function acts as a "smoother" of the physical properties involved in the computation.

As we can see in equation 2.3.3, the kernel function depends on two length scales which are intrinsic to SPH: the distance between particles, $r - r'$, and the smoothing length h . The kernel function should satisfy the following conditions:

$$\int_{\Omega} W(r - r', h) = 1 , \quad (2.3.4)$$

$$\langle f(r) \rangle \longrightarrow f(r), \quad \text{for } h \longrightarrow 0 . \quad (2.3.5)$$

The smoothing kernel is normalized as 2.3.4 and $W(r)$ peaks about $r = 0$, therefore follows the same definition as Dirac's delta function $\delta(r - r')$ for $h \rightarrow 0$. We have

$$\lim_{h \rightarrow 0} W(r - r', h) = \delta(r - r') . \quad (2.3.6)$$

Most SPH implementations use spherical kernel functions as we can see in 2.3.7. To reduce computational calculations by not including the relatively minor contributions of distant particles, often defined by a distance proportional to h defined by s , we truncate the kernel after a finite value. So for a general kernel $W(\vec{r}, \vec{h})$ we have

$$W(\vec{r}, \vec{h}) \equiv W(r, h) \quad \text{with } r = |\vec{r}| \quad , \quad h = |\vec{h}| \quad (2.3.7)$$

and

$$W(r, h) = 0 \quad \text{when } r > s \cdot h. \quad (2.3.8)$$

As we have already said, the basic principle of the SPH method is to divide the fluid into a discrete set of particles, so equation 2.3.3 can be approximated as

$$\langle f(r_i) \rangle = \sum_{j=1}^N f(r_j) W(r_i - r_j, h) dV_j , \quad (2.3.9)$$

where the summation is over all other particles within the kernel domain, usually called neighbors (see Fig. 2.3.2). V_j is the volume of the particles j and r_i denotes the position of the particle.

If we use the following relationship between the volume, density and mass,

$$V_j = \frac{m_j}{\rho_j}, \quad (2.3.10)$$

equation 2.3.9 transforms as

$$\langle f(r_i) \rangle = \sum_{j=1}^N f(r_j) W(r_i - r_j, h) \frac{m(r_j)}{\rho(r_j)}, \quad (2.3.11)$$

which is the equation to obtain the property $f(r_i)$ of the particle at position r_i , which is calculated from the contribution of each neighbor particle within the smoothing length h and weighed according to the kernel function $W(r_i - r_j, h)$. Now for example for the density ρ , we must replace $f(r_i)$ with the density $\rho(r_i)$ and we get the following equations,

$$\langle \rho(r_i) \rangle = \sum_{j=1}^N \frac{m(r_j)}{\rho(r_j)} \rho(r_j) W(r_i - r_j, h), \quad (2.3.12)$$

$$\langle \rho(r_i) \rangle = \sum_{j=1}^N m(r_j) W(r_i - r_j, h) = \sum_{j=1}^N m_j W_{ij}, \quad (2.3.13)$$

where the density ρ of the particle in position r_i is equal to the sum of the masses from the neighbors particles, weighing for the Kernel function.

The kernel function $W(r_i, r_j, h)$ for the FI code is the spline kernel of [Monaghan and Lattanzio \(1985\)](#), where in this case only the particles within $2h$ of a given point will contribute to the smoothed estimates:

$$W(r_i, h) = \frac{1}{\pi h^3} \begin{cases} 1 - \frac{3}{2} \left(\frac{r_i}{h}\right)^2 + \frac{3}{2} \left(\frac{r_i}{h}\right) & , \quad 0 \leq r_i \leq h \\ \frac{1}{4} \left(2 - \frac{r_i}{h}\right)^3 & , \quad h \leq r_i \leq 2h \\ 0 & , \quad \text{otherwise} . \end{cases} \quad (2.3.14)$$

The equations of motion for the particles (Equation 2.3.15) in the SPH method are derived from the discretized Lagrangian for a compressible non-dissipative flow, with adiabatic index γ (see [Rasio and Lombardi \(1999\)](#) for a complete derivation.). Another way is substituting 2.3.13 into the equations of gas dynamics

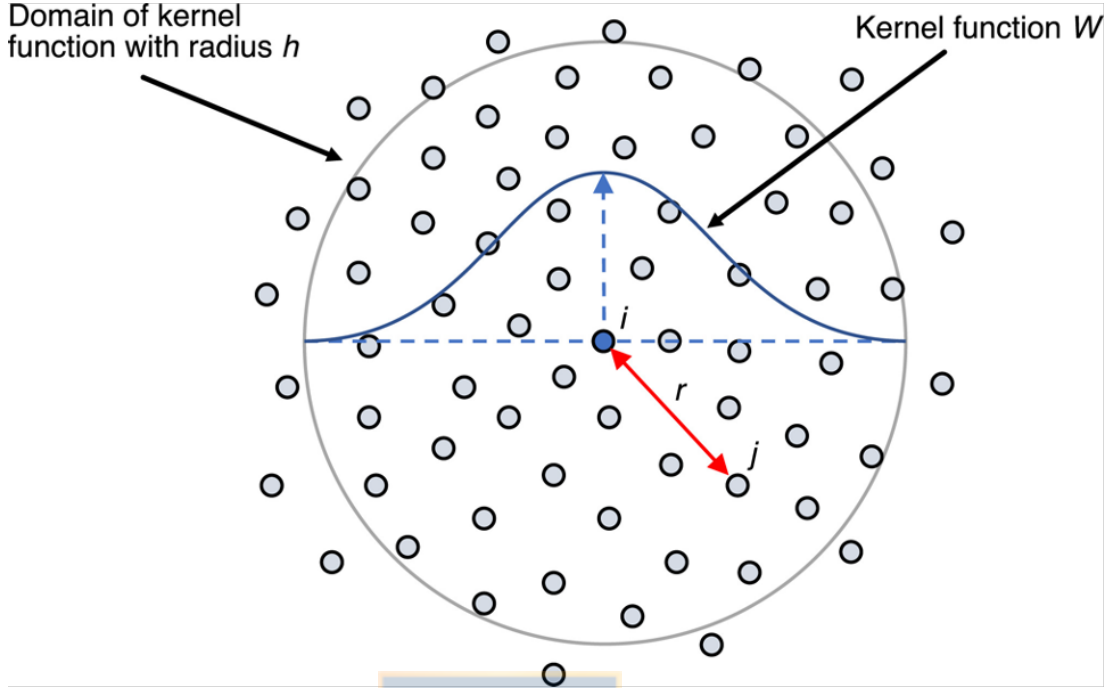


Figure 2.3.2: Schematic image of the SPH method. Domain of particle i with kernel function W which shows the influence of neighbouring particles j , determined by the smoothing length limit h . Particle j is at a distance r from particle i . From Duckworth et al. (2021).

$$L = \sum_i m_i \left(\frac{1}{2} v_i^2 + \frac{1}{\gamma - 1} A_i \rho^{\gamma-1} \right), \quad (2.3.15)$$

where m_i is the mass of each particle, v_i is the velocity and A_i is the entropic function that is defined by $P_i = A_i \rho^\gamma$, with P_i the pressure. In the FI code the internal energy u_i for an adiabatic gas is obtained from the entropic function as

$$u_i = \frac{A_i}{\gamma - 1} \rho^{\gamma-1}, \quad (2.3.16)$$

but for the case we are studying, we consider an isothermal gas, where the state equation is $P = c_s^2 \rho$. Through Equation 2.3.17 we impose an initial temperature on the gas,

$$u_i = \frac{k_B T_{init}}{(\gamma - 1)\mu}. \quad (2.3.17)$$

2.3.3 Smoothing lengths

The smoothing length is an important parameter within the SPH method. Equation 2.3.13 is subject to two interpretations of h that are analogous for computational calculations. We will now explain the basic ideas of the 'scatter' and 'gather' which are two possible interpretations of the smoothing length.

2.3.3.1 Scatter interpretation

The most traditional one is the scatter interpretation. It assumes that each particle has a corresponding mass and that it is distributed according to W and h in space. Then, to obtain the density of a point in space, we sum the contributions from the density profiles of neighboring particles within a given distance (see Fig. 2.3.3a).

2.3.3.2 Gather interpretation

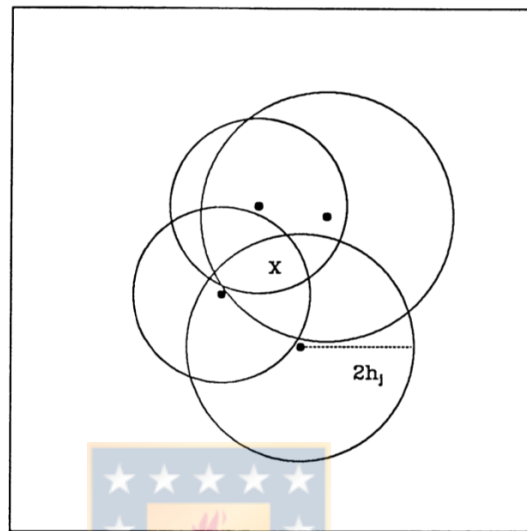
On the other hand we have the gather interpretation, where the local properties of a point in space are obtained by sampling all the neighboring particles and weighting the contribution of each according to W (Hernquist and Katz, 1989a).

In the SPH method an adaptive smoothing length h_i is usually used, such that a fixed mass is contained within the smoothing volume which is the same as saying that the number of neighbors within the smoothing length is more or less constant (Equation 2.3.18). But this introduces errors in the conservation of energy and/or the conservation of entropy. To avoid the inclusion of the error due to the variability of h_i , FI considers h_i as a dynamic variable in the Lagrangian that introduces restrictions that determine the variable (Springel and Hernquist, 2002). We consider the set of N constraints determined by Equation 2.3.19,

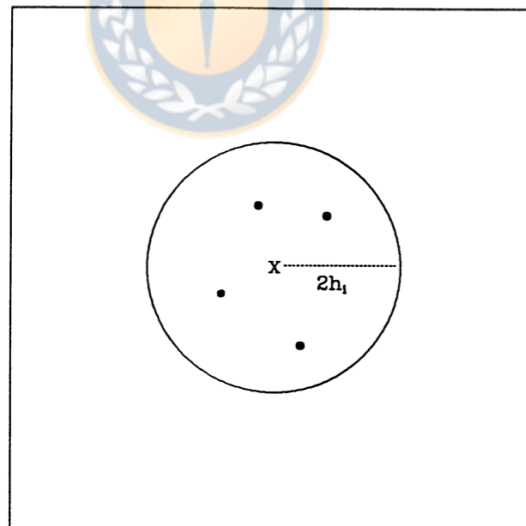
$$M_{sph} = \frac{4\pi}{3} h_i^3 \rho_i , \quad (2.3.18)$$

$$\phi_i(q) \equiv \frac{4\pi}{3} h_i^3 (\rho_i + \tilde{\rho}) - M_{sph} = 0 , \quad (2.3.19)$$

where $M_{sph} = \bar{m} N_{sph}$ relates the mass M_{sph} to the typical number N_{sph} of smoothing neighbors (usually between 50 to 60 particles) for an average particle mass \bar{m} . Compared to the original equation given by Springel and Hernquist



(a) Scatter



(b) Gather

Figure 2.3.3: In (a) we illustrate the “scatter” interpretation. In (b) the “gather” interpretation is demonstrated (Hernquist and Katz, 1989a).

(2002), in FI a $\tilde{\rho}$ is added to limit the smoothing length h_i , since without this extra term when $\rho_i \rightarrow 0$ then $h_i \rightarrow \infty$.

In this way the extra ∇h is solved, introducing it implicitly in the equations of motion. So from the equation 2.3.19 we can get a definition of h_i as

$$h_i^3 = \frac{3}{4\pi} \frac{N_{sph} \bar{m}}{(\rho_i + \tilde{\rho})}. \quad (2.3.20)$$

2.4 Gravity

In AMUSE we can find several families of algorithms that have been developed to solve the N-body problem that span most dynamic regimes except the support for large scale cosmological simulations is limited. They are divided into three types of N-body codes which are: pure N-body codes, direct N-body codes and approximate N-body codes. The codes in these categories scale as $O(N \log N)$ (Barnes and Hut, 1986b), some scale better, $O(N)$ (Ambrosiano et al., 1988; Dehnen, 2014), some much worse, $O(N^4)$ (Boekholt and Portegies Zwart, 2015). In this study we used pure N-body codes mainly, so if you need to get more information about the another N-body codes, you can look at Portegies Zwart and McMillan (2018).

Ph4, Hermite, Brutus, HiGPUs, PhiGRAPE, SmallN are pure N-body codes that solve Newton's equations of motion with no free physical parameters with Hermite time stepping schemes. Most have some capacity to flag special events, such as close encounters or binary dynamics. The only adjustable quantity in a pure N-body code is the time-stepping criterion used to integrate the equations of motion and some are tooled to use hardware (GRAPE or GPU) accelerated force calculation.

2.4.1 Equations of motion for a self-gravitating system

The N-body problem consists of following the evolution of a system formed by N bodies interacting under their mutual gravity. To get this we need to solve the equations of motion described in the Philosophiæ Naturalis Principia Mathematica, Newton (1687) in his chapter Axiomata Sive Leges Motus (the Axioms or Laws of Motion). In Newtonian gravity, the gravitational acceleration a_i of an object

(subscript i) due to a group of objects (subscript j) is calculated by

$$a_i \equiv \ddot{r}_i = G \sum_{j \neq i}^N m_j \frac{r_j - r_i}{|r_j - r_i|^3}. \quad (2.4.1)$$

G is the gravitational constant, and m_j and r_j are the mass and position of particle j . This equation is a set of coupled, second-order, nonlinear, singular ordinary differential equations. The solutions of Equation 2.4.1 can consist of a variety of complex, often chaotic motions, and Newton's equations of motion are applicable in most of the scales. Only for a few cases ($N = 2$ and some special cases with $N = 3$) the N -body problem can be solved analytically. For a larger number of particles, the solution has to be found numerically and gravitational dynamics or N -body codes need to be involved.

We use an N -body code to evolve the stellar dynamics because we want to follow in detail the dynamical evolution of the protostars, i.e. their position, velocity, mass, etc. step by step.



2.4.2 Ph4 Code

Ph4 is a 4th order Hermite predictor-corrector (Makino and Aarseth, 1992) N -body code, compatible with GPU acceleration and written in C++. The Hermite scheme is based on Hermite interpolation with a predictor-corrector scenario. This means with an extrapolation of the equations of motion, we get a predicted position and velocity at some time; then with this information we calculate new accelerations, and finally we do a correction of the predicted values using interpolation, based on finite difference terms.

In the Hermite Individual Timestep Scheme each particle i has its own time (t_i), timestep (Δt_i), position ($r_{i,0}$) and velocity (v_i) at time t_i , and acceleration (a_i) and time derivative of acceleration (\dot{a}_i) calculated at time t_i . The acceleration and its time derivative for each particle due to all other particles are given by:

$$a_{0,i} = \sum_{j \neq i}^N G \frac{m_j}{r_{ij}^3} r_{ij}, \quad (2.4.2)$$

$$\dot{a}_{0,i} = \sum_{j \neq i}^N Gm_j \left[\frac{v_{ij}}{r_{ij}^3} + \frac{3(r_{ij} \cdot v_{ij})r_{ij}}{r_{ij}^5} \right], \quad (2.4.3)$$

where G is the gravitational constant, m_j the mass of the j th particle, where $r_{ij} = r_j - r_i$ and $v_{ij} = v_j - v_i$.

The integration is done based on the following steps:

- (a) Select particles i with a minimum $t_i + \Delta t_i$.
- (b) Predict the positions and the velocities of all particles at time t using r , v , a and \dot{a} .
- (c) Calculate the acceleration (a_i) and it's time derivative (\dot{a}_i) for particle i at time t , using the predicted positions and velocities.
- (d) Calculate $a_i^{(2)}$ and $a_i^{(3)}$ using a Hermite interpolation based on a and \dot{a} , then add the corrections to the position and velocity of particle i . Calculate the new timestep and update t_i .
- (e) Go back to step a).

Then we predict the positions and velocities of all particles. These predicted values are obtained from the Taylor expansion

$$r_{p,i} = r_i + (t - t_i)v_i + \frac{(t - t_i)^2}{2}a_i + \frac{(t - t_i)^3}{6}\dot{a}_i, \quad (2.4.4)$$

$$v_{p,i} = v_i + (t - t_i)a_i + \frac{(t - t_i)^2}{2}\dot{a}_i. \quad (2.4.5)$$

Now using the positions and velocities predicted by Equations 2.4.4 and 2.4.5 we obtain the accelerations a_i and its derivatives for the particles i using equations 2.4.2 and 2.4.3 incorporating a softening parameter ϵ ,

$$a_i = \sum_{j \neq i}^N Gm_j \frac{r_{ij}}{(r_{ij}^2 + \epsilon^2)^{3/2}}, \quad (2.4.6)$$

$$\dot{a}_i = \sum_{j \neq i}^N Gm_j \left[\frac{v_{ij}}{(r_{ij}^2 + \epsilon^2)^{3/2}} + \frac{3(r_{ij} \cdot v_{ij})r_{ij}}{(r_{ij}^2 + \epsilon^2)^{5/2}} \right], \quad (2.4.7)$$

where

$$r_{ij} = r_{p,j} - r_{p,i}, \quad (2.4.8)$$

$$v_{ij} = v_{p,j} - v_{p,i}. \quad (2.4.9)$$

The corrector is based on the third-order Hermite interpolation constructed using a and \dot{a} at times t_i and $t_i + \Delta t_i$. The third-order Hermite interpolation polynomials for the acceleration terms are expressed as:

$$a_i = a_{0,i} + \dot{a}_{0,i}\Delta t_i + \frac{\Delta t_i^2}{2}a_{0,i}^{(2)} + \frac{\Delta t_i^3}{6}a_{0,i}^{(3)}, \quad (2.4.10)$$

$$\dot{a}_i = \dot{a}_{0,i} + a_{0,i}^{(2)}\Delta t_i + \frac{\Delta t_i^2}{2}a_{0,i}^{(3)}, \quad (2.4.11)$$

where $\Delta t = t - t_i$, a_0 and \dot{a}_0 are the acceleration and its derivative calculated at time t_i . We don't know the derivatives $a_{0,i}^{(2)}$ and $a_{0,i}^{(3)}$, therefore we cannot calculate the accelerations directly from the positions and velocities. However with the equations 2.4.2 and 2.4.3 we can calculate $a_{p,i}$ and $\dot{a}_{p,i}$ using the predicted values of $r_{p,i}$ and $v_{p,i}$ calculated from the initial values using the equations 2.4.4 and 2.4.5. When we have $a_{p,i}$ and $\dot{a}_{p,i}$ we replace them in Equation 2.4.10 and have

$$a_{0,i}^{(2)} = \frac{-6(a_{0,i} - a_{p,i}) - \Delta t_i(4\dot{a}_{0,i} + 2\dot{a}_{p,i})}{\Delta t_i^2}, \quad (2.4.12)$$

$$a_{0,i}^{(3)} = \frac{12(a_{0,i} - a_{p,i}) + 6\Delta t_i(\dot{a}_{0,i} + \dot{a}_{p,i})}{\Delta t_i^3}, \quad (2.4.13)$$

where $a_{p,i}$ and $\dot{a}_{p,i}$ are the acceleration and its derivative at time $t_i + \Delta t_i$. Now if we extend the equations 2.4.4 and 2.4.5 by two more orders we have the correction formulae for the position and velocity,

$$r_{1,i} = r_{p,i} + \frac{\Delta t_i^4}{24}a_{0,i}^{(2)} + \frac{\Delta t_i^5}{120}a_{0,i}^{(3)}, \quad (2.4.14)$$

$$v_{1,i} = v_{p,i} + \frac{\Delta t_i^3}{6} a_{0,i}^{(2)} + \frac{\Delta t_i^4}{24} a_{0,i}^{(3)}. \quad (2.4.15)$$

Now, we need to calculate the next timestep for particle i . It is calculated with the standard formula (Aarseth, 1985)

$$\Delta t_i = \sqrt{\eta \frac{|a_{1,i}| |a_{1,i}^{(2)}| + |\dot{a}_{1,i}|^2}{|\dot{a}_{1,i}| |a_{1,i}^{(3)}| + |a_{1,i}^{(2)}|^2}}, \quad (2.4.16)$$

where η is a dimensionless accuracy parameter which controls the error. The timestep is proportional to $\sqrt{\eta}$ and the integration error is expected to be proportional to η^2 . The values of $a_{1,i}$ and $\dot{a}_{1,i}$ are already known, the value $a_{1,i}^{(3)}$ is the same as that of $a_{0,i}^{(3)}$, because it was used in the third-order interpolation. The second-order derivative, $a_{1,i}^{(2)}$ is given by:

$$a_{1,i}^{(2)} = a_{0,i}^{(2)} + \Delta t_i a_{0,i}^{(3)}. \quad (2.4.17)$$

The choice of the timestep in N-body simulations is very important, because if we allow the timestep to change in time it can offer a great saving in computational cost, but variable-size time steps usually imply a substantial degradation in energy conservation. Hut et al. (1995) present a 'meta-algorithm' for choosing time steps in such a way as to guarantee time symmetry in any integration scheme, thus allowing improve energy conservation for orbital calculations with variable time step.

2.4.2.1 The Ahmad-Cohen scheme

In particle codes we generally have to find a balance between precision and computational cost, thus even if the code can reach high precision in the calculation of the positions and velocities of the particles, the full calculation of a_i (2.4.6) and \dot{a}_i (2.4.7) for each particle due to the contribution of all the other particles is very time-consuming, especially if the simulations have a large N.

Therefore we need a method to speed up this calculation while maintaining the collisional approach. The Ahmad-Cohen scheme (ACS) is used in ph4 to solve this problem. The main idea of the ACS is that the gravitational force on a particle

is divided into two components, one from its neighbors (a_n) and the other from distant (a_d) particles:

$$a_i = a_{i,n} + a_{i,d}. \quad (2.4.18)$$

2.5 Sink particles

Star formation can occur through different processes and in different scenarios that are generally related to binary or multiple systems (Duquennoy and Mayor, 1991). A complete theory of star formation must account for the formation of binary and multiple systems. On the other hand, to obtain the most important aspects of the interactions between protostars and their neighbors, it is necessary to sacrifice the internal details of the protostars. Fragmentation is a possible mechanism to explain the formation of most binary systems, where a large number of calculations concentrates on the isothermal collapse of low-mass molecular cloud cores, as well as in cases of fragmentation of spherical clouds, collapse of elongated clouds and protostellar disc. Often such calculations are forced to stop after the formation of fragments, since the time-step to follow the evolution becomes very small. As fragments typically contain a small percentage of the cloud mass, it becomes impossible to compare the results of fragmentation calculations with observations, since the final properties of the binaries will depend on the accretion or the interaction with the rest of the cloud material (see Bate et al. (1995)). To solve the timestep problem and to study the fragmentation of the SPH cloud, a non-gaseous, accreting particle was introduced, allowing a cloud to collapse beyond fragmentation. This is called a 'Sink Particle'.

The sink particles were first developed by Bate et al. (1995) to follow fragmentation using smoothed particle hydrodynamics (SPH). The main idea was to follow the fragmentation of a gas cloud for a longer time, since in the SPH method the collapse and fragmentation generates high-density zones that are represented by many particles with a small spacial separation. The main problem is that regions of high density require small time-steps, making the simulation time very long, limiting the time for which we can continue the simulation. So we never can resolve the fragmentation of the cloud and compare it with the stellar system. A solution is to replace these high density zones with a single particle that only interacts

gravitationally with the gas. Since we are not interested in the internal properties of the protostars, the SPH particles in a very dense zone are replaced by a sink particle, which has the combined mass of the SPH particles, linear momentum and the spin of the particles it replaces. The typical sink particles are mass-points with an accretion radius r_{acc} , which determines the limit at which an SPH particle is considered to be accreted or not. Incorporating sink particles in an SPH method is relatively simple given the Lagrangian nature of SPH, so to incorporate sink particles we need:

- A method of accreting infalling gas.
- A method for the dynamic creation when a protostellar fragmentation is created.
- Boundary conditions between the sink particles and the neighboring SPH particles.

The correct implementation of these boundary conditions is very important as ideally the sink particle should not affect the gas evolution outside the accretion radius. One effect is that a non-spherical gravitational potential is replaced by a spherical-point-mass potential, although this should only cause small changes. More important is the effect of the discontinuity in the number of particles across the accretion radius due to particles inside being accreted, because this affects the pressure and viscosity forces of the SPH particles outside (see section 2.2.3 in [Bate et al. \(1995\)](#) and the sections 'THE OldSink ALGORITHM' and 'THE UrSink ALGORITHM' in [Hubber et al. \(2013\)](#)).

Fig. 2.5.1 demonstrates the importance of boundary conditions for the correct implementation of sink particles in SPH simulations. It is observed that the volume of the SPH particle near the boundary has an area with missing neighbors (side 1) and another unaffected area (side 2). This causes need for larger smoothing lengths for SPH particles near the boundary, to keep ≈ 50 neighbor SPH particles. The properties of the SPH particles near the boundary (such as density) are underestimated due to the missing neighbors on side 1. The SPH particles near the boundary will be attracted to the accretion hole due to the null pressure from the missing SPH particles. And the standard SPH artificial viscosity suffers from bulk and shear viscosity components.

In this work we used the sink algorithm for the creation and evolution of sink

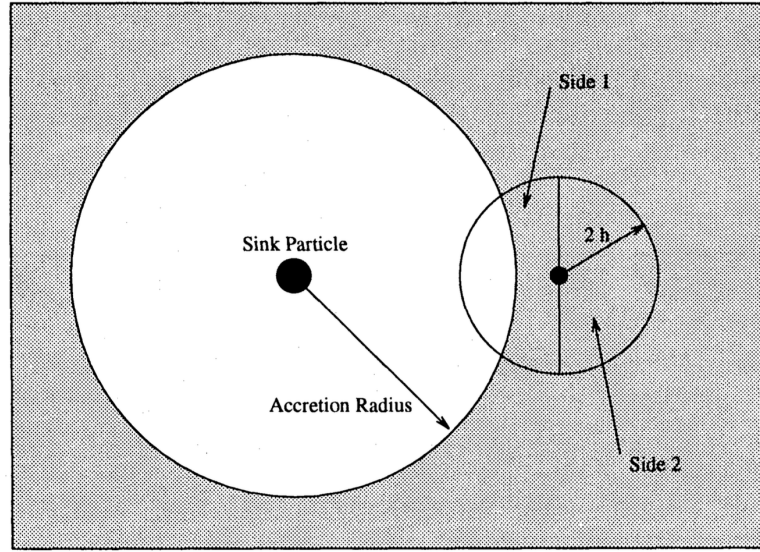


Figure 2.5.1: Configuration of a SPH particle near the accretion radius of a sink particle. The volume that contains SPH particles is shaded, and the white volume is the inside of the accretion radius contains no gas particles. From [Bate et al. \(1995\)](#).

particles in SPH simulations proposed by [Hubber et al. \(2013\)](#), where some important aspects are: (i) It avoids the spurious creation of sinks. (ii) It regulates the accretion of matter onto a sink so as to mitigate non-physical perturbations in the vicinity of the sink. (iii) When the sink accretes matter the associated angular momentum is returned to the surrounding medium. In the next section we will explain the accretion method for sinks and later the creation method will be explained.

2.5.1 Sink accretion

The force $F(x)$ on a particle of mass m_s at position x is generated by the gravitational attraction of a mass distribution $\rho(x')$. With Newton's inverse-square law of gravitation, it may be obtained by summing the small contributions

$$\delta F(x) = Gm_s \frac{x' - x}{|x' - x|^3} \delta m(x') = Gm_s \frac{x' - x}{|x' - x|^3} \rho(x') d^3 x' \quad (2.5.1)$$

to the overall force from each element of a volume $d^3 x'$ located at x' . Thus the force per unit mass is given as

$$F(x) = m_s g(x), \quad (2.5.2)$$

where the gravitational field is

$$g(x) \equiv G \int d^3x' \frac{x' - x}{|x' - x|^3} \rho(x'). \quad (2.5.3)$$

If we define the gravitational potential $\Phi(x)$ by

$$\Phi(x) \equiv -G \int d^3x' \frac{\rho(x')}{|x' - x|}, \quad (2.5.4)$$

and using

$$\nabla_x \left(\frac{1}{|x' - x|} \right) = \frac{x' - x}{|x' - x|^3}, \quad (2.5.5)$$

we may write $g(x)$ as

$$g(x) = \nabla_x \int d^3x' \frac{G\rho(x')}{|x' - x|} = -\nabla\Phi. \quad (2.5.6)$$

Now if we take the divergence of Equation 2.5.3 we have

$$\nabla \cdot g(x) = -G\rho(x) \int d^2\Omega = -4\pi G\rho(x), \quad (2.5.7)$$

and substituting $g(x)$ with the equation 2.5.6, we obtain Poisson's equation relating the potential Φ to the density ρ :

$$\nabla^2\Phi = 4\pi G\rho. \quad (2.5.8)$$

Integrating both sides of Equation 2.5.8 over an arbitrary volume containing total mass M , and applying the divergence theorem, we obtain

$$4\pi GM = 4\pi G \int d^3x \rho = \int d^3x \nabla^2\Phi = \int d^2S \cdot \nabla\Phi. \quad (2.5.9)$$

We used Gauss's theorem, which states that the integral of the normal component of $\nabla\Phi$ over any closed surface equals $4\pi G$ times the mass contained within that surface.

2.5.1.1 Timescale for spherically symmetric radial accretion

For spherical systems we have a mass of

$$M(r) = 4\pi \int_0^r dr' r'^2 \rho(r'), \quad (2.5.10)$$

where the total gravitational potential may be considered to be the sum of the potentials of spherical shells of mass

$$dM(r) = 4\pi\rho(r)r^2 dr, \quad (2.5.11)$$

so the rate at which mass flows inwards across a spherical surface at radius r is

$$\dot{M}(r) = -4\pi r^2 \rho(r) v_{RAD}(r). \quad (2.5.12)$$

Now for an SPH implementation at the position of an SPH particle j in the interaction-zone of sink particle s , we can rewrite vectorially

$$r^2 = r_{js}^2 = |\Delta r_{js}| \Delta r_{js} \quad (2.5.13)$$

and for all the components we have

$$\dot{M}_j = -4\pi |\Delta r_{js}| \Delta r_{js} \cdot \Delta v_{js} \rho(r). \quad (2.5.14)$$

The time scale for radial accretion is obtained by dividing the total mass of the SPH particles in the interaction zone by a weighted sum of the inflow rates, thus:

$$\langle t_{RAD} \rangle_s = \sum_j \frac{M_j}{\dot{M}_j}, \quad (2.5.15)$$

$$\langle t_{RAD} \rangle_s = \frac{\sum_j \{m_j\} w}{4\pi \sum_j \{|\Delta r_{js}| \Delta r_{js} \cdot \Delta v_{js} m_j W(|\Delta r_{js}|, H_s)\}}, \quad (2.5.16)$$

where W is the kernel function. The smoothing length of the sink H_s is adjusted so that the extent of the kernel function equals R_s , and w ensures that the sum is accurately normalised,

$$w = \sum_j \{m_j W(|\Delta r_{js}|, H_s) / \rho_j\}. \quad (2.5.17)$$

2.5.1.2 Timescale for disc accretion

The model for disc accretion is based on the [Shakura and Sunyaev \(1973\)](#) prescription, which parameterizes all possible mechanisms of angular momentum transport with a single variable, α_{ss} . For a low-mass disc with a star of mass M_* , the accretion timescale at radius R is

$$t_{DISC} \sim \alpha_{ss}^{-1} (GM_* R)^{1/2} a^{-2}, \quad (2.5.18)$$

with a the local sound speed and with the kernel-weighted mean over all the SPH particles in the interaction-zone,

$$\langle t_{DISC} \rangle = \frac{(GM_s)^{1/2}}{\alpha_{SS}} \sum_j \left\{ \frac{|\Delta r_{js}|^{1/2}}{a_j^2} \right\}, \quad (2.5.19)$$

$$\langle t_{DISC} \rangle = \frac{(GM_s)^{1/2}}{\alpha_{SS} w} \sum_j \left\{ \frac{|\Delta r_{js}|^{1/2} m_j W(|\Delta r_{js}|, H_s)}{\rho_j a_j^2} \right\}. \quad (2.5.20)$$

Note that the index j denotes the SPH particles in the interaction zone. From theoretical ([Hartmann, 1998](#)) and observational ([Forgan et al., 2011](#)) estimates of the accretion disk it is suggested that $\alpha_{SS} \approx 0.01$ as a default value, but with large uncertainties.

2.5.1.3 Net timescale for accretions models

In the model proposed by [Hubber et al. \(2013\)](#) the equation for the calculation of the timescale for the accumulation of mass that gives the correct limiting behavior

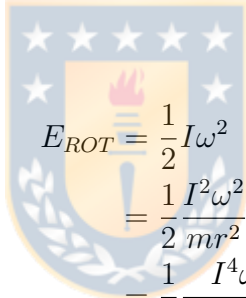
is

$$t_{ACC} = \langle t_{RAD} \rangle_s^{(1-f)} \langle t_{DISC} \rangle_s^f. \quad (2.5.21)$$

If the SPH particles inside the sink are in rotational equilibrium, the accretion timescale takes the form $t_{ACC} \rightarrow \langle t_{DISC} \rangle_s$. If they are not rotating at all, $t_{ACC} \rightarrow \langle t_{RAD} \rangle_s$. f has the following form

$$f = MIN \left\{ \frac{2E_{ROT}}{|E_{GRAV}|}, 1 \right\}, \quad (2.5.22)$$

with E_{ROT} the net rotational energy and E_{GRAV} the net gravitational energy of the SPH particles in the interaction-zone relative to the sink particle s . Then from the definition of rotational energy we have



$$\begin{aligned} E_{ROT} &= \frac{1}{2} I \omega^2 \\ &= \frac{1}{2} I^2 \omega^2 \\ &= \frac{1}{2} \frac{I^2 \omega^2}{mr^2} \\ &= \frac{1}{2} \frac{I^4 \omega^4}{mr^2 I^2 \omega^2} \\ &= \frac{1}{2} \frac{I^4 \omega^4}{m|r \cdot I\omega|^2}. \end{aligned} \quad (2.5.23)$$

Writing the rotational energy for all SPH particles in the interaction-zone of a point-mass s ,

$$E_{ROT} = \sum_j \frac{|I_j \omega_{js}|^4}{2m_j |\Delta r_{js} \cdot I_j \omega_{js}|^2}, \quad (2.5.24)$$

where

$$L_{INT} = \sum_j I_j \omega_{js} = \sum_j \{m_j \Delta r_{js} \times \Delta v_{js}\}, \quad (2.5.25)$$

with L_{INT} the net angular momentum of the gas particles in the interaction-zone relative to the sink particle, i.e.

$$E_{ROT} = \frac{|L_{INT}|^4}{2 \sum_j \{m_j |\Delta r_{js} \cdot L_{INT}|^2\}}. \quad (2.5.26)$$

Now we can derive the gravitational energy from the Lagrangian formulation, where the self-gravitating gas is given by

$$L = \sum_{j=1}^N m_j \left(\frac{1}{2} v_j^2 - \Phi_j - u_j \right), \quad (2.5.27)$$

with Φ the gravitational potential and u the thermal energy per unit mass. Now from the gravitational part of the Lagrangian we can derive an adaptive softening length formalism

$$L_{grav} = - \sum_j m_j \Phi_j, \quad (2.5.28)$$

where from [Dehnen \(2001\)](#) we adopt a general formulation for force softening. Then the modified gravitational potential per unit mass is

$$\Phi(r) = -G \sum_{j=1}^N m_j \phi(|r - r_j|, h), \quad (2.5.29)$$

therefore we can write the gravitational part of the Lagrangian as

$$L_{grav} = -\frac{G}{2} \sum_j \sum_{j' \neq j} m_j m_{j'} \phi(|r_j - r_{j'}|, h_j). \quad (2.5.30)$$

Now swapping indices in the double summation, we have

$$\begin{aligned} \phi(|r_j - r_{j'}|, h_j) &= \frac{\phi(|r_j - r_{j'}|, h_j) + \phi(|r_j - r_{j'}|, h_j)}{2} \\ &= \frac{\phi(|r_j - r_{j'}|, h_j) + \phi(|r_{j'} - r_j|, h_{j'})}{2}, \end{aligned} \quad (2.5.31)$$

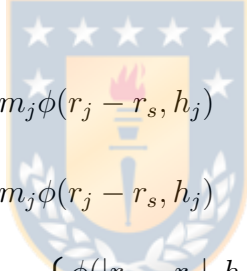
and we have the equivalent to the averaging of the softening kernels in the Lagrangian with the form

$$L_{grav} = -\frac{G}{2} \sum_j \sum_{j' \neq j} m_j m_{j'} \left\{ \frac{\phi(|r_j - r_{j'}|, h_j) + \phi(|r_{j'} - r_j|, h_{j'})}{2} \right\}, \quad (2.5.32)$$

with $|r_j - r_{j'}| = |r_{j'} - r_j| = |\Delta r_{jj'}|$, so

$$L_{grav} = -\frac{G}{4} \sum_j \sum_{j' \neq j} m_j m_{j'} \{ \phi(|\Delta r_{jj'}|, h_j) + \phi(|\Delta r_{jj'}|, h_{j'}) \}. \quad (2.5.33)$$

We also need the gravitational energy from the interaction of the sink particles with the SPH particles, so we can do a similar procedure to calculate its potential and incorporate it into the total gravitational energy. The gravitational part of the Lagrangian of the interaction between the SPH and the sink is given by



$$\begin{aligned} L_{grav} &= -G \sum_j M_s m_j \phi(r_j - r_s, h_j) \\ &= -GM_s \sum_j m_j \phi(r_j - r_s, h_j) \\ &= -GM_s \sum_j m_j \left\{ \frac{\phi(|r_j - r_s|, h_j) + \phi(|r_s - r_j|, H_s)}{2} \right\} \\ &= -GM_s \sum_j m_j \left\{ \frac{\phi(|\Delta r_{js}|, h_j) + \phi(|\Delta r_{js}|, H_s)}{2} \right\} \\ &= -\frac{GM_s}{2} \sum_j m_j \{ \phi(|\Delta r_{js}|, h_j) + \phi(|\Delta r_{js}|, H_s) \}, \end{aligned} \quad (2.5.34)$$

so the gravitational energy can be written as

$$\begin{aligned} E_{GRAV} &= \frac{GM_s}{2} \sum_j m_j \{ \phi(|\Delta r_{js}|, h_j) + \phi(|\Delta r_{js}|, H_s) \} \\ &\quad + \frac{G}{4} \sum_j \sum_{j' \neq j} m_j m_{j'} \{ \phi(|\Delta r_{jj'}|, h_j) + \phi(|\Delta r_{jj'}|, h_{j'}) \}, \end{aligned} \quad (2.5.35)$$

where the relative distance of the particles and the smoothing length are usually

included in the kernel function as $\frac{|\Delta r_{jj'}|}{h_j}$. The gravitational energy becomes

$$E_{GRAV} = \frac{GM_s}{2} \sum_j m_j \left\{ \phi \left(\frac{|\Delta r_{js}|}{H_s} \right) + \phi \left(\frac{|\Delta r_{js}|}{h_j} \right) \right\} + \frac{G}{4} \sum_j \sum_{j' \neq j} m_j m_{j'} \left\{ \phi \left(\frac{|\Delta r_{jj'}|}{h_j} \right) + \phi \left(\frac{|\Delta r_{jj'}|}{h_{j'}} \right) \right\}. \quad (2.5.36)$$

Taking into account the continuous density field, the softening kernel for the gravitational potential in the lagrangian for the self-gravity of the SPH is given by the gravitational potential kernel ϕ (Price and Monaghan, 2007):

$$\phi(r, h) = 4\pi \left(-\frac{1}{r} \int_0^r W(r', h) r'^2 dr' + \int_0^r W(r', h) r' dr' - \int_0^{r_{max}} W(r', h) r' dr' \right), \quad (2.5.37)$$

where the last term is the constant of integration, determined by $\phi \rightarrow 0$ as $r \rightarrow \infty$.

2.5.2 Sink update

To update the different properties of the sink particles at the end of the timestep δt , such as mass M_s , position r_s , velocity v_s and angular momentum L_s , we take into account the accretion, so the updated mass is

$$M'_s = M_s + \sum_j \delta m_j, \quad (2.5.38)$$

the updated position is

$$r'_s = M_s'^{-1} \left(M_s r_s + \sum_j \delta m_j r_j \right), \quad (2.5.39)$$

the updated velocity is

$$v'_s = M_s'^{-1} \left(M_s v_s + \sum_j \delta m_j v_j \right), \quad (2.5.40)$$

and the updated angular momentum is

$$L'_s = L_s + M_s \Delta r_{ss'} \times \Delta v_{ss'} + \sum_j \delta m_j \Delta r_{js'} \times \Delta v_{js'}. \quad (2.5.41)$$

These are the updated values of the properties of the sink particles, and j is the sum for all SPH particles in the interaction zone that lose mass δm_j to the point-mass. If the mass of an SPH particle is zero, it is completely removed from the set of particles.

2.5.3 Angular momentum feedback from a sink particle

Normally the standard sink particles in SPH simulations adopt all the angular momentum from the SPH particles that are accreted, so the sink would spin so fast that it could not reach stellar densities. The standard sink particles are unrealistic in this respect, because they are sinks of both mass and angular momentum. In a more realistic model, material flowing toward a protostar with high angular momentum first falls onto an accretion disk and then continues spiraling inward, transferring the bulk of its angular momentum to material further out in the disk.

Therefore, to try to simulate this more realistic behavior, an angular momentum feedback from the sink particles to the SPH particles is incorporated following [Hubber et al. \(2013\)](#). This is achieved by reducing the angular momentum of the sink particle, transferring part of it to the SPH particles in the surrounding interaction zone. Since the transfer of angular momentum is assumed to be through viscous torques in an accretion disk, the amount of angular momentum transferred is given by

$$|\delta L_s| = |L_s| \left\{ 1 - \exp \left(-\frac{\delta t_s}{t_{DISC}} \right) \right\}, \quad (2.5.42)$$

where each SPH particle j receives a velocity impulse in the interaction-zone of s . From the angular momentum conservation between the sink particle and one SPH particle, we have

$$\begin{aligned}
L_s &= L_j, \\
\Delta r_{js} \times p_s &= \Delta r_{js} \times p_j, \\
|\Delta r_{js}| |p_s| \sin(\theta_s) &= |\Delta r_{js}| |p_j| \sin(\theta_j), \\
||\Delta r_{js}| |p_s| \sin(\theta)| &= ||\Delta r_{js}| |p_j| \sin(\theta)|, \\
|\delta L_s| &= ||\Delta r_{js}| |m_j \delta v_j| \sin(\theta)|, \\
|\delta v_j| &= \frac{|\delta L_s|}{|\Delta r_{js} m_j \sin(\theta)|}, \\
|\delta v_j| &= \frac{|\delta L_s| |L_s| |\Delta r_{js}|}{|\Delta r_{js} m_j \sin(\theta)| |L_s| |\Delta r_{js}|}, \\
|\delta v_j| &= \frac{|\delta L_s| |L_s| |\Delta r_{js}|}{|m_j \Delta r_{js} (L_s \times \Delta r_{js})|}, \\
|\delta v_j| &= \frac{|\delta L_s| |L_s| |\Delta r_{js}| \sin(\theta_s)}{|m_j \Delta r_{js} (L_s \times \Delta r_{js})| \sin(\theta_s)}, \\
\delta v_j &= \frac{|\delta L_s| |L_s \times \Delta r_{js}|}{|m_j \Delta r_{js} \times L_s \times \Delta r_{js}|}.
\end{aligned} \tag{2.5.43}$$

Now for all SPH particles in the interaction-zone,

$$\delta v_j = \frac{|\delta L_s| |L_s \times \Delta r_{js}|}{|\sum_j \{m_j \Delta r_{js} \times L_s \times \Delta r_{js}\}|}. \tag{2.5.44}$$

This velocity impulse is proportional to the distance of the SPH particles from the rotation axis of the point-mass. As the momentum and angular momentum have to be conserved, to compensate the impulses of velocity, the point-mass receives impulses of momentum and angular momentum corresponding to

$$\delta v_s = -M_s^{-1} \sum_j \{m_j \delta v_j\}, \tag{2.5.45}$$

$$\delta L_s = -\sum_j \{m_j \Delta r_{js} \times \delta v_j\}. \tag{2.5.46}$$

Since angular momentum is accurately conserved, the amount of angular momentum acquired by the spin of the point-mass is small, because it is transferred to the SPH particles within the interaction zone. This ensures that

the implemented model is not an angular momentum sink.

2.5.4 Stellar collisions

To solve the collisions between two protostars we adopt the sticky-sphere approximation, which means that a collision occurs when the separation d between two stars is smaller than the sum of the radii of the stars ($R_{\min} \leq R_1 + R_2$). So, when this condition is satisfied, we replace the two colliding stars by a single object at their center of mass.

In first instance we don't consider a mass loss, so we assume that during the collision the total mass is conserved, therefore we will add both masses linearly and the mass of the new single object is

$$m_{\text{new}} = m_1 + m_2. \quad (2.5.47)$$

We assume that the new object reaches a new internal equilibrium, in which the density corresponds to that of an unperturbed star of the same mass.

The different properties of the new star are inherited from its colliding parents, where the new position and velocity are the center of mass of the colliding stars, so

$$\vec{r}_{\text{new}} = \frac{m_1 \cdot \vec{r}_1 + m_2 \cdot \vec{r}_2}{m_1 + m_2}, \quad (2.5.48)$$

$$\vec{v}_{\text{new}} = \frac{m_1 \cdot \vec{v}_1 + m_2 \cdot \vec{v}_2}{m_1 + m_2}. \quad (2.5.49)$$

We also consider that there is conservation of angular momentum in each of its components, so \vec{L}_{new} follows the equation,

$$\vec{L}_{\text{new}} = \vec{L}_1 + \vec{L}_2. \quad (2.5.50)$$

We assume that the properties of the NewSink routine that the new sink inherits, such as the interaction radius and the accretion rate, are equal to the maximum of the two colliding protostars, i.e.

$$R_{\text{int,new}} = \text{MAX}(R_{\text{int},1}, R_{\text{int},2}), \quad (2.5.51)$$

$$\dot{m}_{\text{new}} = \text{MAX}(\dot{m}_1, \dot{m}_2). \quad (2.5.52)$$

Once the mass and accretion rate of the new sink particles have been updated, we calculate their radius through the Hosokawa parameterization, which we will describe in the next section.

2.5.5 The Mass-Radius Parametrization

If in the process of collapse of a primordial molecular cloud an SMS was formed, it inevitably had to collapse into a very massive black hole (BH) initiated by the general relativistic (GR) instability. Then these could grow further via subsequent mass accretion and mergers (Wiklind et al., 2012), and finally become a SMBH. Bromm et al. (2009) argue that SMS development should be understood in the context of primordial star formation; additionally, theoretical works analyze how massive these primordial stars are, through the late evolutionary stages of protostar mass accretion. The first stars are most likely to be less massive than $10^3 M_{\odot}$. But, on the other hand, SMSs with $M_* \gg 10^3 M_{\odot}$ could form through a non-standard mode of primordial star formation, one example being the suppression of H_2 molecule formation, leading to a near-isothermal collapse of a primordial cloud due to the cooling of atomic hydrogen, leading to the formation of a SMS via either spherical infall or through disks. The evolution of accreting SMSs is fundamental for understanding their formation process, because the final mass of the SMS depends of its evolution before the rapid mass accretion stops. Therefore it is very important to study the evolution of primordial stars growing under rapid mass accretion.

To characterize the primordial stars growing under rapid mass accretion we derive a mass-radius parameterization based on Hosokawa and Omukai (2009); Hosokawa et al. (2012, 2013). To simplify the calculation of the properties of protostars we classify them into three different tracks depending on their accretion rate \dot{m} , these are 'SMS', 'VMS' and 'NORMAL'. Initially all protostars start in the *protostar* state and we will describe each track below.

2.5.5.1 PROTOSTAR STAGE

2.5.5.1.1 'SMS' Track Any *protostar* over a critical accretion rate falls within this regime, where the radius of the 'SMS' is very large and increases monotonically with the stellar mass. It is determined for the critical accretion rate $\dot{m}_{crit} = 0.04 \text{ M}_\odot \text{ yr}^{-1}$ from Hosokawa et al. (2013). Therefore for every *protostar* in the 'SMS' track the radius is

$$R_* = 2600 \left(\frac{M_*}{100\text{M}_\odot} \right)^{1/2} R_\odot. \quad (2.5.53)$$

From Sakurai et al. (2015); Schleicher et al. (2013), who studied the evolution of such an 'SMS' growing by rapid mass accretion, the *protostars* will follow this mass-radius relationship until the accretion rate \dot{m} is below \dot{m}_{crit} for more than 100 KH timescales, where the KH timescale is

$$t_{KH} = \frac{GM^2}{RL}, \quad (2.5.54)$$

with M the mass, R the radius and L the luminosity of the *protostars*. In the equations we can see that to calculate the KH timescale of the *protostars* we need the luminosity. From Hosokawa and Omukai (2009) we have a parametrization of the luminosity in different mass ranges. The luminosity is estimated as follows as long as the mass is $\leq 10 \text{ M}_\odot$,

$$L_* = 0.6L_\odot \left(\frac{M_*}{\text{M}_\odot} \right)^{11/2} \left(\frac{R_*}{R_\odot} \right)^{-1/2}. \quad (2.5.55)$$

For $M_* > 10 \text{ M}_\odot$, the luminosity is given by:

$$L_* = 10L_\odot \left(\frac{M_*}{\text{M}_\odot} \right)^3. \quad (2.5.56)$$

For $M_* > 70 \text{ M}_\odot$, the luminosity approaches the Eddington limit in the following manner:

$$L_* = 3.8 \times 10^6 L_\odot \left(\frac{M_*}{100\text{M}_\odot} \right). \quad (2.5.57)$$

After reaching a mass of $600 M_{\odot}$, the *protostar* enters the *supermassive star* stage. Note that if the accretion rate \dot{m} of a *protostar* in the 'SMS' track is below \dot{m}_{crit} for more than 100 KH timescales, the protostar will enter a new evolutionary track based on its previous \dot{m} . From Sakurai et al. (2015) the time during which a 'SMS' *protostar* remains inflated after its accretion rate falls below \dot{M}_{crit} can vary between 10 – 100 KH timescales. We consider the most optimistic scenario adopting 100 KH timescales.

2.5.5.1.2 'VMS' Track We consider a protostar to be in the 'VMS' track, as long as its accretion rate is within the range $10^{-6} \leq \dot{m} < 0.04 M_{\odot}\text{yr}^{-1}$. To characterize this track we use three phases which were described by Hosokawa and Omukai (2009), the *adiabatic accretion phase*, the *swelling*, and the *Kelvin Helmholtz contraction*. First the *adiabatic accretion phase* holds as long as the mass of the *protostar* is $\leq m_{ad}$ which is given by:

$$m_{ad} = 0.9 \left[\left(\frac{\dot{m}}{4.2 \times 10^{-8} M_{\odot}\text{yr}^{-1}} \right) \left(\frac{\dot{m}}{10^{-3} M_{\odot}\text{yr}^{-1}} \right)^{-0.41/2} \right]^{2/9.27}. \quad (2.5.58)$$

For the luminosity in this phase we use Equation 2.5.55 again, and the radius is

$$R_* = 26 \left(\frac{M_*}{M_{\odot}} \right)^{0.27} \left(\frac{\dot{m}}{10^{-3} M_{\odot}\text{yr}^{-1}} \right)^{0.41} R_{\odot}. \quad (2.5.59)$$

To describe the *swelling phase* and the *Kelvin Helmholtz contraction phase* it is useful to define two parameters α and β as:

$$\alpha = 26 \left(\frac{m_{ad}}{M_{\odot}} \right)^{-4.73} \left(\frac{\dot{m}}{10^{-3} M_{\odot}\text{yr}^{-1}} \right)^{0.41}, \quad (2.5.60)$$

$$\beta = \alpha \left(1.2 \frac{m_{ad}}{M_{\odot}} \right)^{7.5}. \quad (2.5.61)$$

Protostars with masses between $m_{ad} \leq m < 1.2m_{ad}$ are in the *swelling phase*. The luminosity in this phase is determined by Equation 2.5.55 and the radius is determined as

$$R_* = \alpha \left(\frac{M_*}{M_\odot} \right)^5 R_\odot. \quad (2.5.62)$$

For the *Kelvin Helmholtz contraction phase* it is useful to define a new parameter of mass, m_{ms} , for which we can define a range of masses where the *protostar* is in the *Kelvin Helmholtz contraction*,

$$m_{\text{ms}} = \left(\frac{\beta}{0.97} \right)^{1/3.07}. \quad (2.5.63)$$

So, a *protostar* is in the *Kelvin Helmholtz contraction* if its mass is in the range $1.2m_{\text{ad}} \leq m < m_{\text{ms}}$. The luminosity is given by Equation 2.5.56 and the radius by

$$R_* = \beta \left(\frac{M_*}{M_\odot} \right)^{-2.5} R_\odot. \quad (2.5.64)$$

A *protostar* in the 'VMS' track enters the *star* stage if its mass is greater than m_{ms} . If a *protostars* in the 'VMS' track has an accretion rate \dot{m} of less than $10^6 M_\odot \text{yr}^{-1}$ for more than a KH timescale, the *protostar* will enter the 'NORMAL' track.

2.5.5.1.3 "NORMAL" Track If a *protostar* has an accretion rate $\dot{m} < 10^{-6} M_\odot \text{yr}^{-1}$ it is on the 'NORMAL' track. The luminosity is determined by Equation 2.5.55 as long as the mass is less than $0.8 M_\odot$, and the radius is given by

$$R_* = 0.86 \left(\frac{M_*}{M_\odot} \right)^{0.27} R_\odot. \quad (2.5.65)$$

Therefore if the mass is $\geq 0.8 M_\odot$ the *protostar* enters the *star stage*. When a sink particle is in the *protostar stage*, it has the ability to switch between the three tracks mentioned above. In the evolution of the M-R relationship for the *protostar* there are processes that are more relevant than others, therefore there is a hierarchy, where the 'SMS' track is in the highest hierarchy and the 'NORMAL' track in the lowest hierarchy. If the accretion rate \dot{m} is high enough, a *protostar* can move to a higher hierarchy track; however, it can only move to a lower hierarchy track if the accretion rate \dot{m} remains lower than the critical accretion rate, \dot{m}_{crit} , for the current track for a time longer than a KH timescale

or 100 KH timescales for *protostars* in the 'SMS' track.

2.5.5.2 STAR STAGE

We calculate the radius and luminosity of a particle in the *star stage* adopting the properties of a star on the main sequence. Therefore from Equation 2.5.57 we have the luminosity and the radius determined as:

$$R_* = 0.97 \left(\frac{M_*}{M_\odot} \right)^{0.57} R_\odot. \quad (2.5.66)$$

In this routine we assume that a particle in the *star stage* will not expand in radius even if the accretion rate is $\dot{m} \geq 0.04 M_\odot \text{yr}^{-1}$, therefore a *star stage* particle will always have the same M-R relationship.

2.5.5.3 SUPERMASSIVE STAR STAGE

When a particle is in the *supermassive star stage*, we get the luminosity from Equation 2.5.57 and the radius is given by Equation 2.5.53. Note that it is not necessary for a particle to always be in the *supermassive star state*, since it can still contract if the accretion rate falls below the critical accretion rate during time scales greater than 100 KH. So the particle would change from a *supermassive star state* to a *star state*.

Chapter 3

Development of the Setup

3.1 Previous steps for the implementation

To explore the formation of supermassive black holes through the hybrid pathway via mergers and accretion we need to extend the domains of the codes beyond their limits. Even though AMUSE is very versatile, it presents problems when trying to solve the proposed scenarios in this study. For this reason we believe it is important to detail the intermediate steps in the development of the model.

3.2 Initial temperature

One of the objectives in this study is to analyze the collapse of an isothermal gas cloud at different temperatures, corresponding to different efficiencies of cooling. As we use an isothermal equation of state, it is necessary to change the initial temperature to model the collapse under different assumptions for the cooling. While in the Fi code it is possible to change the initial temperature easily, in the version implemented within AMUSE it cannot be done directly. So we need to apply alternative ways to change the initial temperature of the gas. From thermodynamics we know that for a gas the thermal energy is directly related to the initial temperature through the following equation:

$$u = \frac{k_B T_{init}}{(\gamma - 1)\mu}, \quad (3.2.1)$$

where u is the thermal energy of the SPH particles, k is the Boltzmann constant, T_{init} the initial temperature, γ the adiabatic index (as we are simulating a monoatomic gas $\gamma = 5/3$) and μ the mean molecular weight, assumes 75% mass in **H** and 25% mass in **He**.

```
T_ini=8.e3      |units.K
gamma=5./3.
meanmwt=1.23   |units.amu
gas.u=constants.kB*T_ini/((gamma-1.)*meanmwt)
```

Now through Equation 3.2.1 we can consistently change the initial temperature of the SPH particles from the initial conditions.

3.3 External pressure

In physics and science in general, the boundary conditions are very important for the self-consistency of the methods. Unfortunately the Fi version within AMUSE does not have its full capabilities, so some modifications must be made to ensure the consistency of the code. Particularly we initially had problems with the external pressure in the gas cloud. So for the external pressure implementation to work within the code some adjustments must be made. Initially, the gas cloud expands because the pressure outside the cloud is not high enough, causing an outward pressure gradient (see Fig. 3.3.1).

To reverse this, some modifications must be made to the momentum equation within the code, then from the phase space evolution of particle i which is given by Euler's equation,

$$\frac{dr_i}{dt} = v_i, \quad (3.3.1)$$

we have the momentum equation

$$\frac{dv_i}{dt} = -\frac{1}{\rho_i} \nabla P_i + a_i^{\text{visc}} - \nabla \Phi_i, \quad (3.3.2)$$

where Φ_i , is the gravitational potential, a_i^{visc} , the artificial viscosity and P_i is the pressure. For the implementation of the external pressure we are only interested

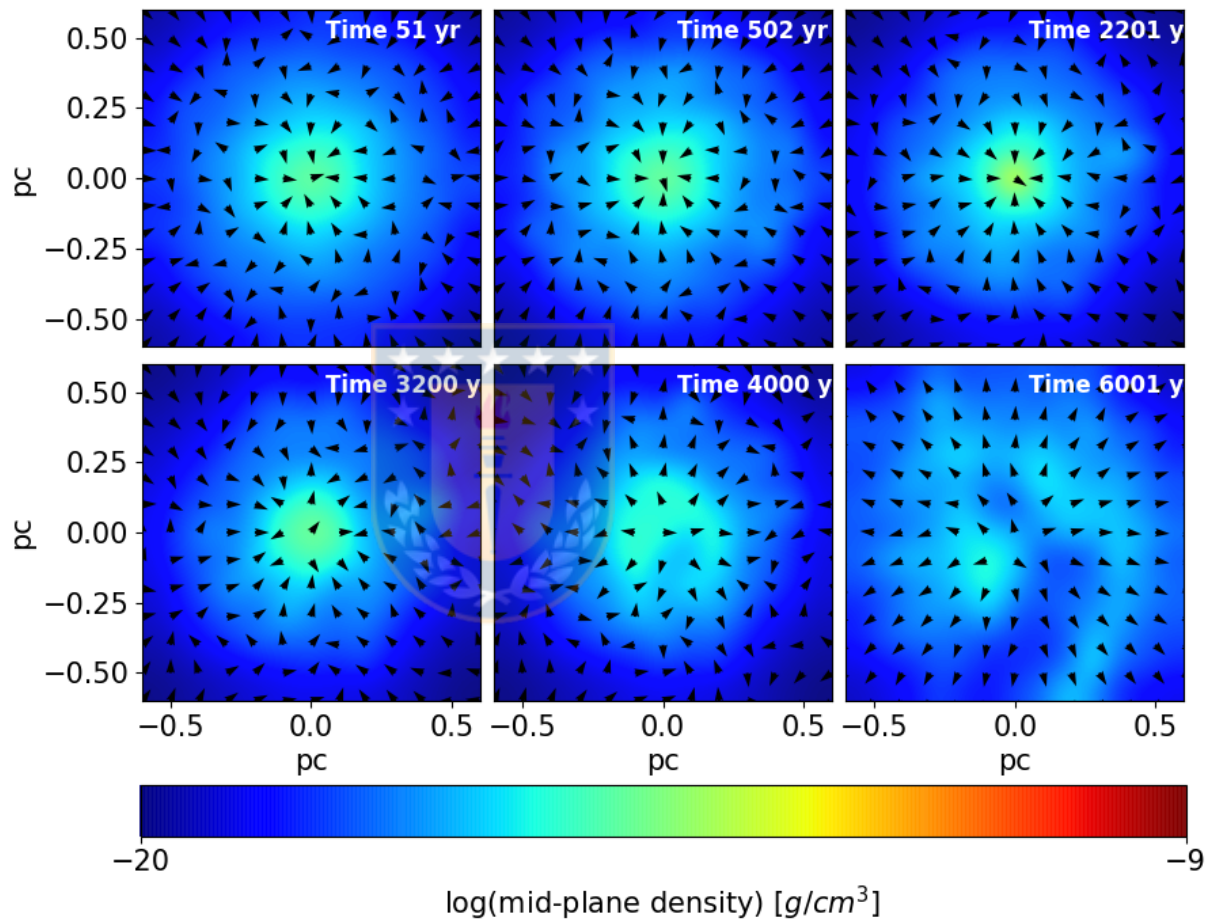


Figure 3.3.1: Different snapshots for the time evolution of the gas cloud density with a mass of $M = 3 \times 10^4 M_{\odot}$ and radius $R = 0.14$ pc, without the external pressure implementation. The red arrows represent the gas velocity field.

in the first term, so for simplicity it can be written as:

$$\begin{aligned}
\frac{dv_i}{dt} &= - \sum_{j=1}^{N_i} m_j \left(\frac{P_i}{\rho_i^2} + \frac{P_j}{\rho_j^2} \right) \nabla_i W(r_{ij,h_{ij}}), \\
&= - \sum_{j=1}^{N_i} m_j \left(\frac{P_i}{\rho_i^2} \nabla_i W(r_{ij,h_i}) + \frac{P_j}{\rho_j^2} \nabla_i W(r_{ij,h_j}) \right), \\
&= - \sum_{j=1}^{N_i} m_j \left(\frac{c_s^2}{\gamma \rho_i} \nabla_i W(r_{ij,h_i}) + \frac{c_s^2}{\gamma \rho_j} \nabla_i W(r_{ij,h_j}) \right).
\end{aligned} \tag{3.3.3}$$

Now adding an external pressure term P_{ext} of the form P_{ext}/ρ^2 , Equation 3.3.3 becomes

$$\frac{dv_i}{dt} = - \sum_{j=1}^{N_i} m_j \left(\left[\frac{c_s^2}{\gamma \rho_i} - \frac{P_{ext}}{\rho_i^2} \right] \nabla_i W(r_{ij,h_i}) + \left[\frac{c_s^2}{\gamma \rho_j} - \frac{P_{ext}}{\rho_j^2} \right] \nabla_i W(r_{ij,h_j}) \right). \tag{3.3.4}$$

To calculate the external pressure, we go through the following steps:

- Make a simulation with the initial conditions for a short period of time ~ 20 yr.
- Calculate the average pressure at the boundary of the simulated gas cloud and convert it to code units.
- The script *entdot.f90* inside the FI file must be modified (an example of the path is: `/home/amuse/src/amuse/community/fi/src/entdot.f90`).
- in the file *entdot.f90* the following equation must be changed three times,

```

aij=fi*lcsound**2/(gamma*lrho)*dwmass+ &
fnbi*csound(nb)**2/(gamma*rho(nb))*dwmass1

```

by the following modified equation,

```

aij=fi*(lcsound**2/(gamma*lrho) -p_ext/(lrho*lrho))*dwmass+ &
fnbi*(csound(nb)**2/(gamma*rho(nb)) -p_ext/(rho(nb)*rho(nb)))*dwmass1

```

where "p_ext" is the external pressure that was calculated earlier.

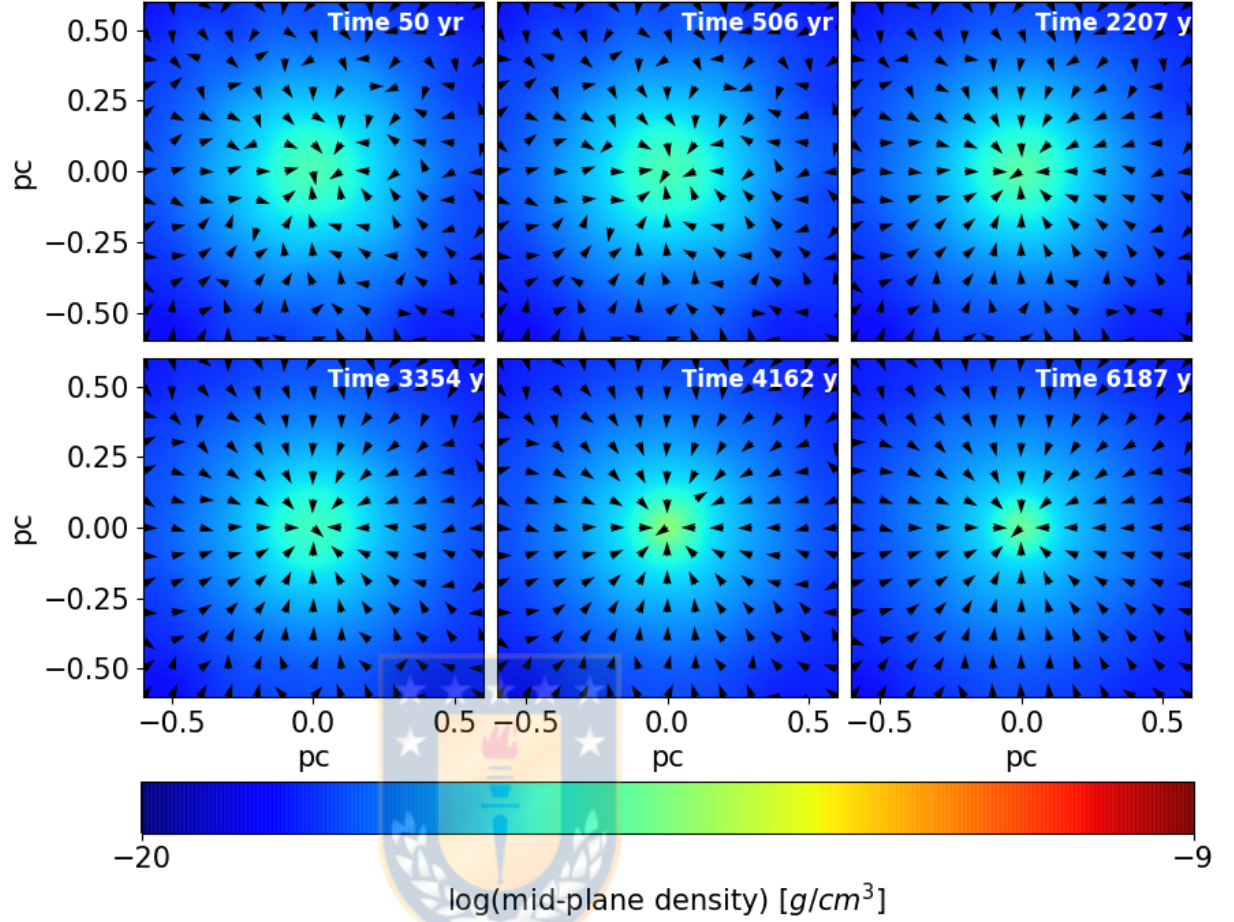


Figure 3.3.2: Different snapshots for the time evolution of the gas cloud density with a mass of $M = 3 \times 10^4 M_{\odot}$ and radius $R = 0.14$ pc, with the external pressure implementation. The red arrows represent the gas velocity field.

- Finally, the FI code must be compiled.

3.4 High density limitation

One of the most important limitations of the numerical sciences today is the ability to solve phenomena on different scales simultaneously. For example it is very difficult to solve the dynamics of a star cluster and at the same time the hydrodynamics inside them. Although the SPH method has many advantages, it also has disadvantages such as to solve for the evolution in low density zones. On the other hand at very high densities, the distance between the particles is very small and therefore the calculation time is very extended.

Specifically in the most massive systems that we analyze in this work it is possible

to reach very high gas densities, generally close to the most massive object in the center of the system. Since the average density is approx. $1 \times 10^{-11} \text{ g/cm}^3$ and the densest zones reach approximately solar densities ($\sim 1 \text{ g/cm}^3$), the code tries to resolve very different distance scales and it becomes extremely slow, making the evolution of the system impossible. To solve this resolution problem we implement two routines that we will explain next.

3.4.1 Adiabatic implementation

Initially the collapse of the gas cloud is modeled with an isothermal equation of state, therefore the temperature remains constant while it collapses. An isothermic state equation is:

$$PV = \text{constant} . \quad (3.4.1)$$

As the collapse for an isothermic cloud is much faster than an adiabatic one, we quickly reach high densities in the gas cloud, producing one of the main problems within the SPH method, which is: to solve very high density systems. To reduce the rapid collapse and give more time for the sink accretion, we implement a local change from the isothermal state equation to an adiabatic equation of state,

$$PV^\gamma = \text{constant} , \quad (3.4.2)$$

where γ is the adiabatic index ($\gamma = 5/3$). Then for some critical density ρ_{crit} we can approximate the equation of state including a change from an isothermal behavior to an adiabatic one. To incorporate this in the code, we must modify the internal energy equation as follows:

$$u = u_0 \left(1 + \frac{\rho}{\rho_{crit}} \right)^{\gamma-1} , \quad (3.4.3)$$

where u_0 is the initial internal energy, ρ the density of the SPH particles and ρ_{crit} the limit density to make the transition from an isothermal behavior to an adiabatic one. For $\rho < \rho_{crit}$ the gas behaves isothermally and it is approximately adiabatic for $\rho \geq \rho_{crit}$ (see Fig. 3.4.1).

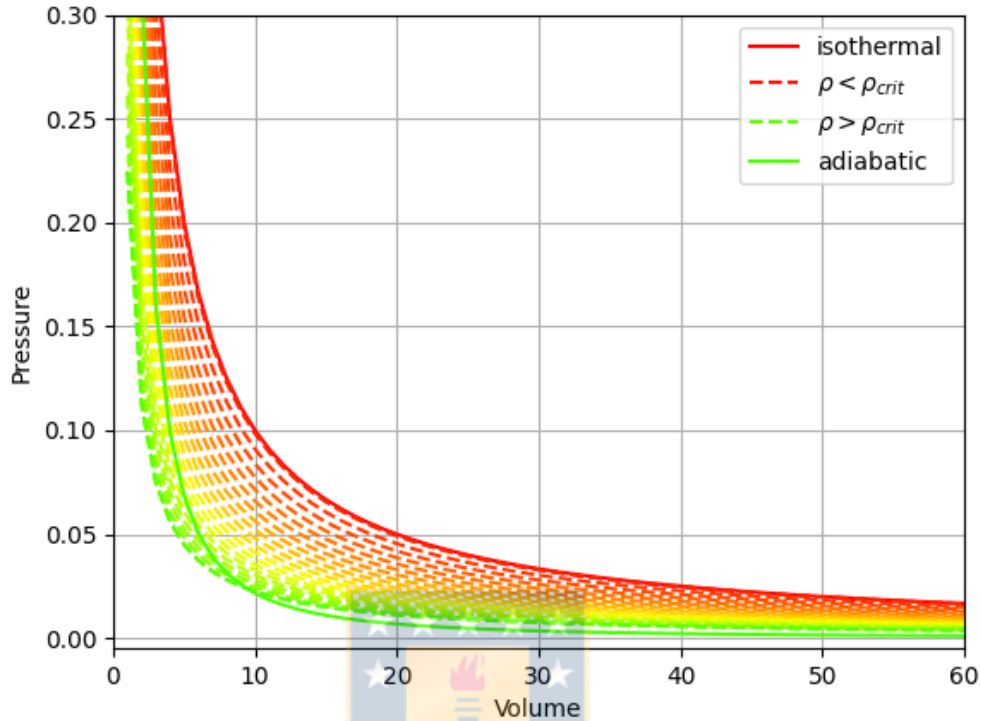


Figure 3.4.1: Pressure vs Volume for an isothermic equation of state (red line), an adiabatic state equation (green line) and an equation of state according to the equation proposed in 3.4.3 for different densities (dashed lines).

The selection of the critical density ρ_{crit} depends on the temperature, so we need to have a critical density for a certain temperature T where the gas behaves approximately adiabatic. For this we use the behavior for low metallicity ($Z/H < -5$) in Omukai et al. (2005) shown in the Fig. 3.4.2.

To use this implementation in the code, the following steps must be followed:

- Tabulate the critical density ρ_{crit} for a temperature T and pass it to code units.
- With the temperature T calculate the internal energy u_0 and pass it to code units.
- The script *ethstep.f90* in the FI file must be modified (an example of the path is: `/home/amuse/src/amuse/community/fi/src/ethstep.f90`).
- Within the file *ethstep.f90* the following equation must be commented (!)

twice,

```
call exstepp(p,dt,eth,deth,drad,lerad,lhe,imax,jmax)
```

and add the following modified equation,

```
eth = u_0*(1. + (rho(p)/rho_crit)**gamma1)
```

where 'u_0' is the internal energy and 'rho_crit' is the critical density.

- Finally, the FI code must be compiled.

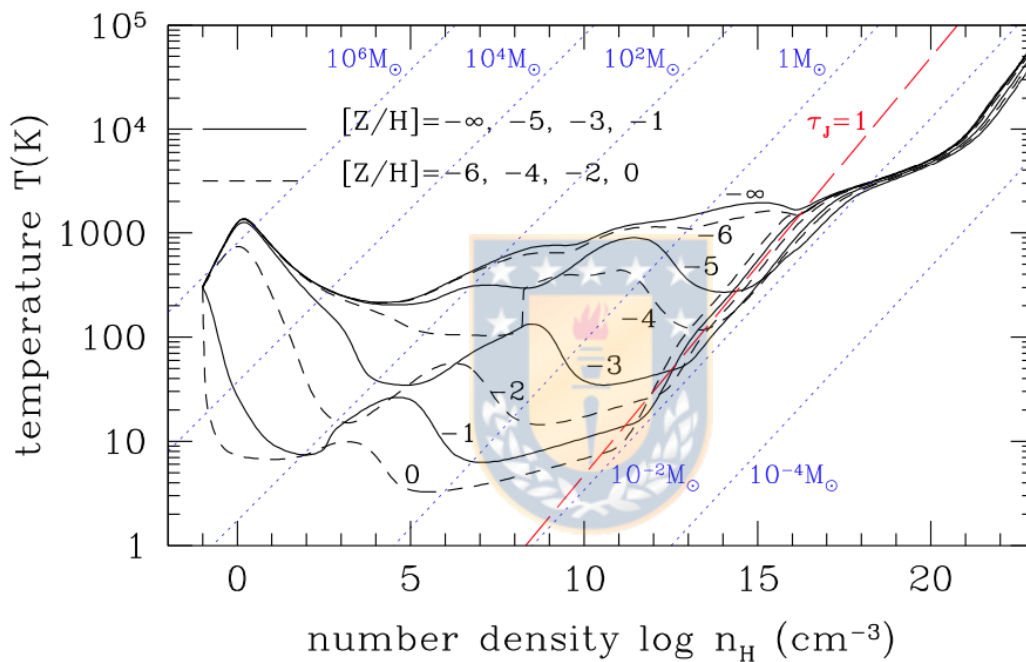


Figure 3.4.2: Temperature evolution of prestellar clouds with different metallicities. The metallicities $[Z/H] = -\infty$ ($Z = 0$), -5 , -3 , -1 and -6 , -4 , -2 , 0 are shown by solid and dashed lines. The lines for constant Jeans mass are indicated by thin dotted lines. From Omukai et al. (2005).

3.4.2 Sink creation

As we already mentioned, a disadvantage of the SPH method is the treatment of the zones of high and low density. One way to solve the problem of high densities to model accretion and reduce the computational charge, is the implementation of sink particles. Particularly if we want to follow the evolution of the system, we need the creation of sink particles to be able to resolve the zones of high densities that are reached due to the collapse and accretion of the gas. As we mentioned

earlier in this study, we implemented the NewSink model proposed by [Hubber et al. \(2013\)](#), where we employed four consistent criteria that allow us to model the formation of new sink particles.

The basic idea in creating a new sink particle s is that it is triggered by an SPH particle i with a smoothing length h_i , which reaches a density limit ρ_{sink} . Once this critical density is reached, the SPH particle is replaced by a new sink particle s , with the same mass, position and velocity of the SPH particle i . The new interaction radius of the new sink particle is calculated as

$$R_s = X_{sink} h_i , \quad (3.4.4)$$

where X_{sink} is a user defined parameter which is chosen so that all neighbors of the candidate SPH are accreted when the new sink particle is created. We choose $X_{sink} = 4$, noting that with this choice we get a smoother accretion but coarser resolution.

3.4.2.1 Density criterion

The first criterion for the formation of a new sink particle is that one SPH particle i with a position r_i and a density $\rho_i \equiv \rho_{SPH}(r_i)$ should exceed a user-defined density threshold, ρ_{sink} , i.e.

$$\rho_i > \rho_{sink} , \quad (3.4.5)$$

where we use the value $\rho_{sink} \geq 2^{-8} \text{ g cm}^{-3}$ for the density threshold ([Becerra et al., 2018](#)).

3.4.2.2 Sink-overlap criterion

The second criterion describes that for the formation of a new sink particle s , the candidate SPH particle i that satisfies the first criterion must not be in superposition or within of the interaction-zone of another pre-existing protostar s' , i.e.

$$|r_i - r_{s'}| > X_{sink} h_i + R_{s'} , \quad (3.4.6)$$

where $R_{s'}$ and $|r_i - r_{s'}|$ are the radius of the candidate SPH and its distance from the pre-existing protostar.

3.4.2.3 Gravitational potential minimum criterion

The third criterion is the condition that the gravitational potential ϕ_i , of the candidate SPH particle i should be smaller than that of all its neighbors j , i.e the particle is at a minimum of the gravitational potential.

$$\phi_i < \text{MIN}\{\phi_j\} . \quad (3.4.7)$$

This criterion was introduced by [Federrath et al. \(2010\)](#), and ensures that the new sink particles are only created near resolved potential minima and hence, presumably, resolved density peaks.

3.4.2.4 Hill Sphere criterion

The fourth criterion says that all pre-existing sink particles s' must satisfy the Hill condition

$$\rho_i > \rho_{Hill} \equiv \frac{3X_{Hill}(-\Delta r_{is'} \cdot \Delta a_{is'})}{4\pi G|\Delta r_{is'}|^2} , \quad (3.4.8)$$

where $\Delta a_{is'}$ is the acceleration vector for the preexisting sinks s' and X_{Hill} is a user-defined parameter for which we use the default value $X_{Hill} = 4$. The condition ensures that a potential new sink particle in a region where a sink particle already exists in its center, but which is larger than the accretion radius of that sink for example a condensation of a Kelvin-Helmholtz contraction, can only be formed in the outskirts of the condensation if there is a local density peak at r_i that dominates the local gravitational field surrounding the potential new sink.

3.5 Setup

To explore the effects of how the gas-dynamics and star-dynamics affect the evolution of a SMBH seed we model a star cluster inside of a compact gas cloud in virial equilibrium. As we mentioned in the previous chapter the gas is modeled consistently through SPH particles, with a total of 2^{17} SPH particles per simulation.

In all simulations the mass of the gas cloud is $M_{gas} = 3 \times 10^4 M_{\odot}$, with a virial radius of 0.14 pc . The protostars were simulated by sink particles that interact only through gravity with themselves and with the gas. The initial sink particle number is 256 and they all have masses of $0.1 M_{\odot}$, which are compatible with protostar masses that emerged from atomic cooling halos (Becerra et al., 2015). Both the protostars and the gas particles follow a plummer distribution (Plummer, 1911), with a half-mass radius of 0.1 pc and a cut-off radius of 5 Plummer radii for each model. The initial velocity of the gas particles is zero and for the protostars the velocities follow a virial equilibrium condition. We simulate isothermal gas clouds with different temperatures and we assume a primordial composition of 75% atomic hydrogen and 25% helium. In the following table we summarize the initial conditions for all simulations performed for this study.

N_{SPH}	$M_{tot,gas}$ [M_{\odot}]	R_{gas} [pc]	$M_{0,gas}$ [M_{\odot}]	T [K]	N_{star}	$M_{tot,star}$ [M_{\odot}]	$M_{0,star}$ [M_{\odot}]
2^{17}	3×10^4	0.14	~ 0.23	300	256	25.6	0.1
2^{17}	3×10^4	0.14	~ 0.23	500	256	25.6	0.1
2^{17}	3×10^4	0.14	~ 0.23	1000	256	25.6	0.1
2^{17}	3×10^4	0.14	~ 0.23	8000	256	25.6	0.1

Table 3.5.1: Summary of the initial conditions.

3.6 Computational resources

The simulations were performed on the hybrid cluster Kultrun hosted at the Department of Astronomy at the University of Concepción, Chile. Kultrun provides tools for analysis of observational data. Also Kultrun was built to perform three-dimensional simulations of star-forming regions, black-holes, galaxy formation and evolution including chemistry and microphysics. Kultrun is managed via a system called SLURM and monitored via Ganglia.

In Kultrun we can find three queues with different architecture, number of cores, and processors. All queues (MAPU, KO_SM and KUTRAL_AMD) have SuperMicro components and it have the following components:

- 1 Headnode
- 1 Shared memory machine
- 18 INTEL Computing nodes

- 2 AMD Computing nodes
- 1 Backup/Storage server
- 48 ports 10 GbE Switch

In this thesis we used the distributed memory cluster MAPU with 18 intel nodes with a total of 576 cores, 64 GB RAM and 4 TB scratch space per node. Each node has 2 x Intel 6130 (Xeon Gold) processors, 32 cores and 2.1 GHz.



Chapter 4

Results

The main goal of our study is to understand the possibility of SMBH seed formation through collisions and accretion. For this we perform simulations with the conditions described in Table 3.5.1. Additionally we explore the evolution of the gas cloud assuming cooling at different temperatures considering an isothermal evolution.

In the same way, another objective of this study is to analyze which of the different components (stellar-dynamical or gas-dynamical processes) of the system most affect the formation of the most massive object (MMO) in the cluster and analyze the mechanisms by which the MMO accumulates mass.

First we will show the results considering a cloud of warm gas, with only the presence of hydrogen and later we show the simulations for colder gas clouds, assuming the presence of molecular hydrogen.

4.1 Runaway collisions and accretion simulations

We first show the results of the evolution of simulations assuming a gas cloud only with the presence of atomic hydrogen lines, with a temperature of $T = 8000$ K. The simulation is stopped at approximately ~ 35000 yr, because at this point most of the gas has already been accreted and the creation of a supermassive object at the center of the cluster is clearly established, which includes most of the mass of the system.

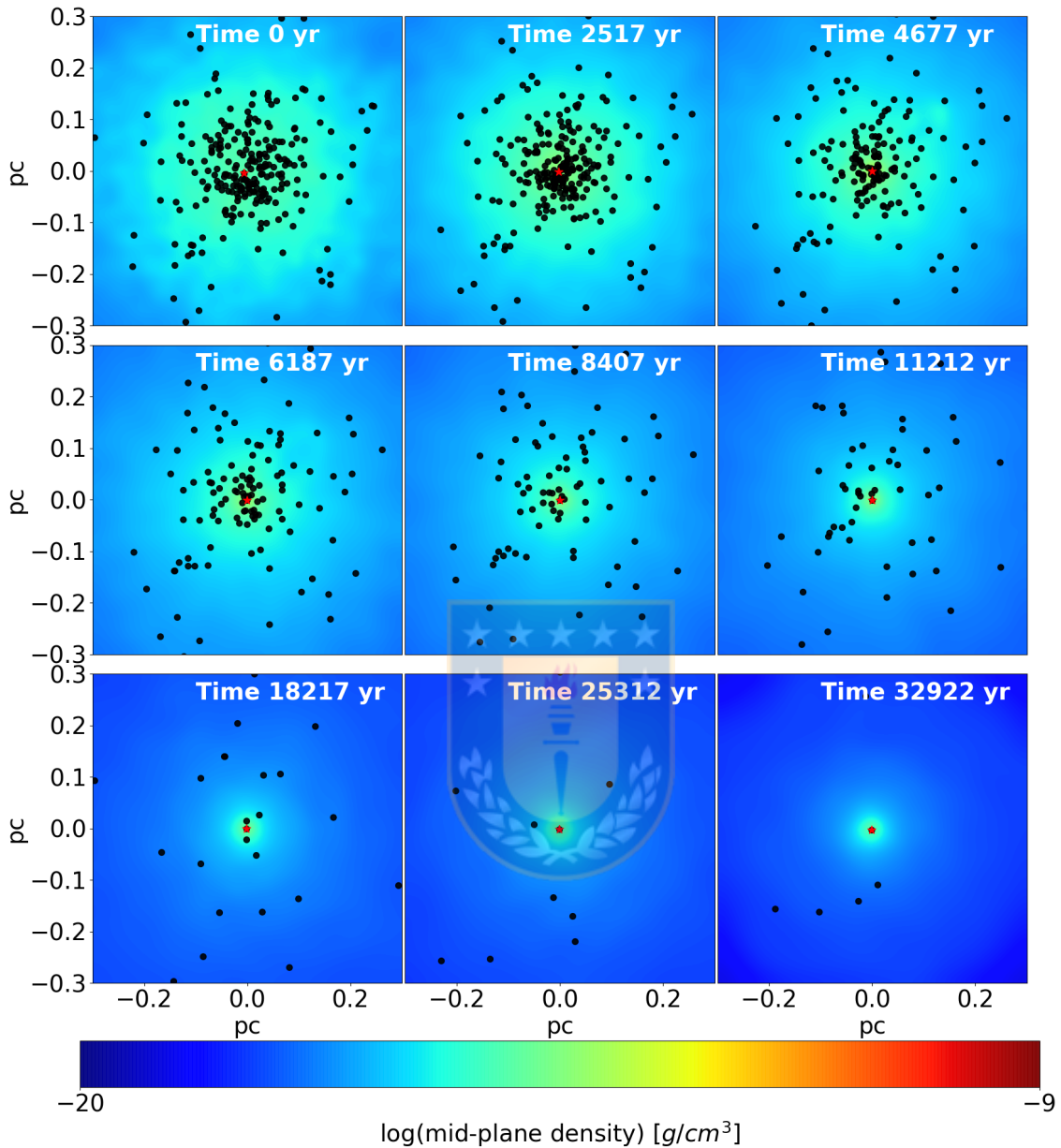


Figure 4.1.1: Density projections for simulations with an initial temperature of 8000 K at different times of a primordial gas cloud with an embedded protostar cluster. The black dots are the protostars and the red dot is the MMO of the cluster. The collapse of the gas cloud and the migration of the MMO towards the cluster center are observed.

In Fig. 4.1.1 we show the evolution of one of our simulations in different snapshots from left to right and from top to bottom. The gas is represented through a density projection and the protostars through black dots. We clearly observe an overdensity in the center of the cluster at the beginning, followed by a rapid

collapse by the protostars, leading to the formation of an MMO in the center of the cluster.

Table 4.1.1 shows an overview of the results obtained for our simulations with an initial temperature of $T = 8000$ K. The mean final mass of the MMO at the end of the simulation, calculated from several random simulations, is show in Table 4.1.1. The evolution of the clusters is very similar, and in all cases the formation of a massive object is achieved. The value of the mean final mass for the most massive central object at the end of the simulations is $29699.8 M_{\odot}$, corresponding to $\sim 99\%$ of the mass of the system. We see that most of the protostars collide ($\sim 95\%$), allowing for the formation of one or more massive objects.

ID	M_{MMO} [M_{\odot}]	\dot{m}_{MMO} [M_{\odot}/yr]	%	M_{gas} [M_{\odot}]	T_{mean} [K]	N_{star}	M_{star} [M_{\odot}]	N_{coll}	M_{esc} [M_{\odot}]
1	29610.5	0.714	98	413.3	8023.4	13	29612.3	243	0
2	29754.5	0.637	99	269.6	8011.8	15	29756.0	241	0
3	29734.4	0.736	99	289.5	8000.2	13	29736.1	243	0

Table 4.1.1: Summary of the simulations. From left to right the columns correspond to the simulation name, final mass of the MMO, mean accretion of the MMO, percentage of the MMO final mass as a function of the total mass of the system, the final gas mass, mean temperature, final star number, final star mass, number of collisions and the total escaped mass.

A large fraction of the total mass of the system is transferred from the gas to the protostars via accretion and later to the MMO by accretion and collisions of massive protostars. Fig. 4.1.2 shows the evolution of the mass fraction for all systems, where most of the gas mass ($\sim 90\%$) is transferred to the protostars (0.2 Myr) for all cases, allowing the possibility of the formation of one or several massive objects. We note that the total mass that escapes (green color) from the system is zero, i.e. the entire initial mass of the system remains gravitationally bound and mostly in the protostars.

Although the mass exchange between stars and gas can be seen directly and very quickly, the collapse of the cluster occurs in parts. This is reflected in Fig. 4.1.3 where the Lagrangian radii of 10%, 30%, 50%, 75% and 90% of the 'STARS', 'GAS' and 'GAS + STARS' components of the system are shown. In the upper and middle panels, the protostars collapse rapidly towards the center of the cluster together with the core of the gas cloud due to the deep gravitational potential,

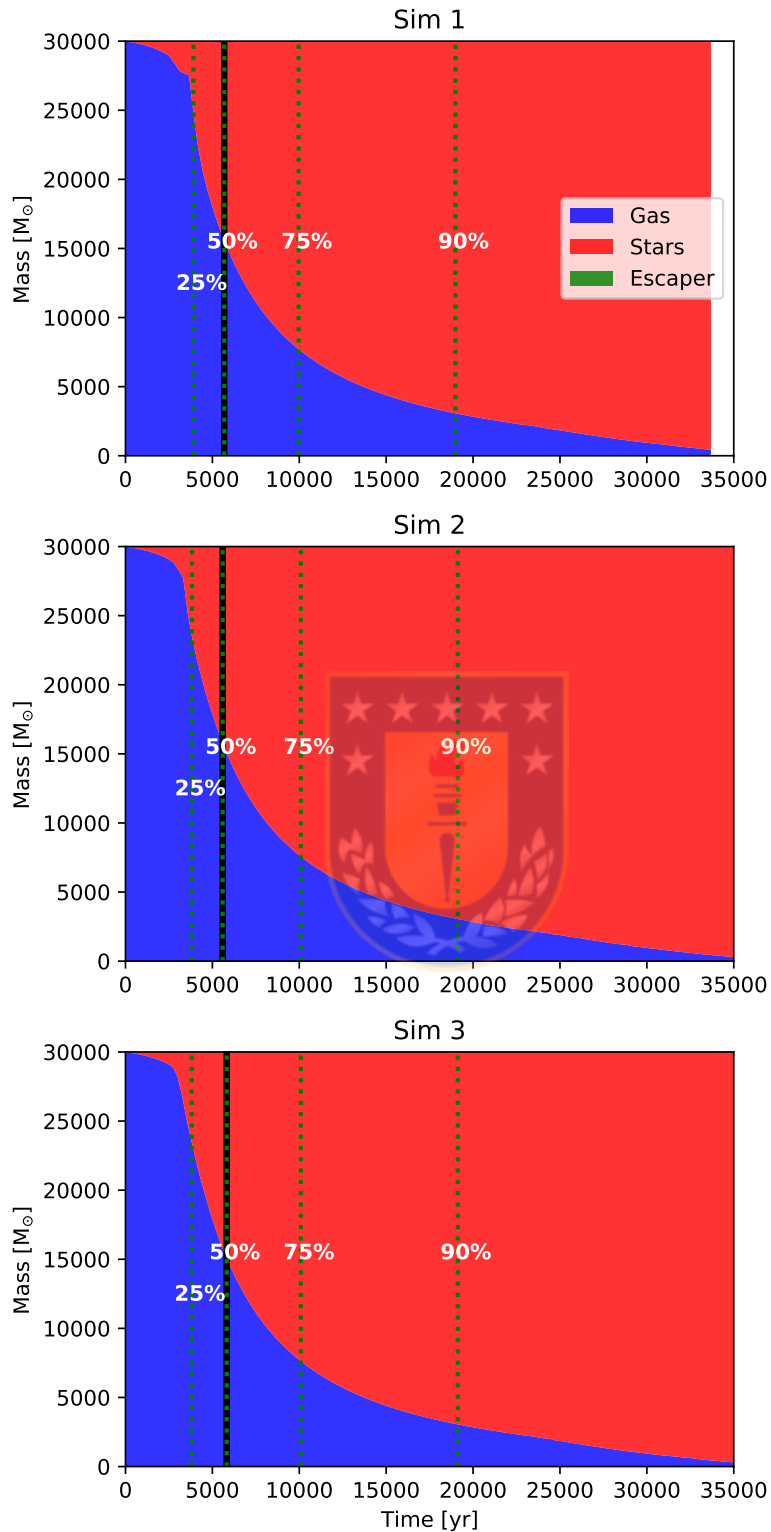


Figure 4.1.2: Time evolution of the mass fraction for the simulations with an initial temperature of 8000 K of the gas (blue zone), stars (red zone) and the mass that escapes (green zone), according to the escape criterion. The green dotted lines are the times when the protostars accreted 25%, 50%, 75% and 90% of the gas mass.

which leads to the formation of a massive object before ~ 5000 yr. After the rapid collapse of the core, the other Lagrangian radii continue contracting, leading to the formation of a massive object with a mass of $\gtrsim 90\%$ of the total mass before 0.2 Myr. The reason that the gas apparently collapses slower than the total mass of the system is due to the high accretion rate in the center of the system caused by high densities and a deep gravitational potential. Therefore the gas fraction is rapidly reduced, causing an expansion of the Lagrangian radii, as we can see in the middle panel.

Now we know that most of the gas is accreted by the protostars, forming very massive protostars and these collide rapidly, possibly forming a single massive object. To understand the evolution of the system and the most important processes in the formation of an MMO we need to study in more detail the evolution of the gas, the MMO and the protostars. Therefore Fig. 4.1.4 shows the gas mass fractions and the protostar mass fractions (upper panels) and the correlation with the collision rate (lower panels), the mass of the MMO and the total mass of the remaining protostars (second panels), the radius of the MMO and the mean radius of the remaining protostars (third panels).

In the first panel we again observe the evolution of the total mass of the gas and the protostars, where the intersection of the curves corresponds to the moment when the dynamics of the system is dominated by the protostars and not by the gas. We observe that this occurs very quickly, approximately at ~ 5000 yr, which indicates that the gas was accreted very quickly and therefore could not be very relevant in the general evolution of the system or just play a determining role at the beginning. From the second panels of Fig. 4.1.4 we observe the formation of a single massive object (red line), which consumes most of the mass and the remaining protostars (blue line) only reach masses less than a few dozen at hundreds of solar masses; possibly due to the short accretion time triggered by a deep potential that led to early collisions.

We can observe from the third panels of Fig. 4.1.4 that the initial phase of the evolution of the system is marked by high accretion rates for both the MMOs and the other protostars. Even when in simulations 1 and 3 the MMO is a protostar already present in the initial conditions and in simulation 2 the MMO is a protostar that forms later, its formation is marked by very high accretion rates, which indicates the following possibilities: (i) The protostars that finally

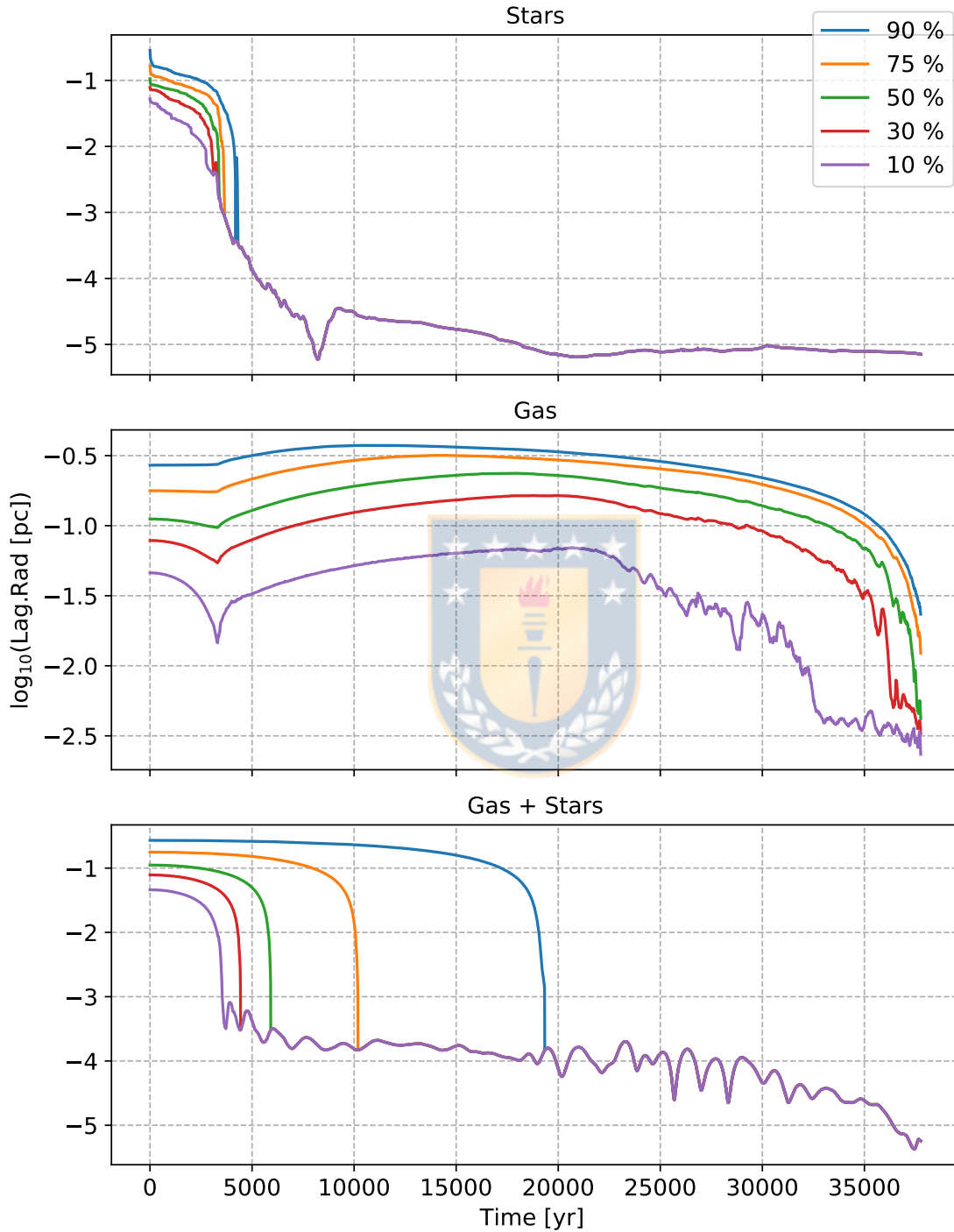


Figure 4.1.3: Time evolution of the 90%, 75%, 50%, 30% and 10% Lagrangian radii in one of our 8000 K simulations. In the top panel the Lagrangian radii for the protostars labeled as 'Stars' are shown, in the middle panel for the gas 'Gas' and in the bottom panel the Lagrangian radii for the total system 'Gas + Stars'.

become the MMO quickly fall to the center of the cluster, where thanks to the high gas concentration we can explain their high accretion rates. (ii) The most central protostars in the cluster are the protostars that become the MMO thanks to a gas-rich environment, causing high accretion rates. (iii) Due to the rapid collapse of the gas towards the center of the cluster, a protostar forms very quickly thanks to the high densities and abruptly consumes the surrounding gas. It is necessary to highlight that the difference between these possibilities will depend on the initial distribution of the protostars in the cluster, where if there are more protostars near the center, it is more likely that they will become the MMO of their system. On the other hand, if the central region of the cluster has only a small population of protostars or they were momentarily ejected by gravitational kicks, it is more likely that the MMO is a new protostar born from the high densities in the center of the cluster.

The high accretion rates of the protostars are caused by a combination of 2 phenomena. First, the collapse of the protostars and the gas to the center of the cluster leads to an increase in the protostar radii and thus higher accretion rates. Second, as protostars swell due to high accretion rates, their radius is larger, which causes their cross sections to increase, leading to higher collision rates (as seen in the lower panels of Fig. 4.1.4), increasing the radius and repeating the cycle again.

This process is similar for the MMO evolution, where its initial phase is determined by very high accretion rates that quickly make it the most massive object in the cluster, leading to a swelling of its radius over $> 1000 R_{\odot}$ that causes it to become the object with the highest probability of collisions, because it has the largest cross section. This explains why the system tends to form only one massive object, since there is a big difference between the mass of the MMO and the mass of the other protostars in the cluster. This also explains the high collision rates observed in the fourth panel of Fig. 4.1.4.

We also note that the time of the formation of the MMO is close to the time of the highest collisions rate, leading to a decrease of the mean accretion rates and the mean radii of the protostars different to the MMO, as observed in the third and fourth panels of Fig. 4.1.4. Naturally, the decay of the properties of the other protostars is due to the fact that the protostars that collided to form the MMO are the most massive ones in the cluster so far, probably because they are protostars

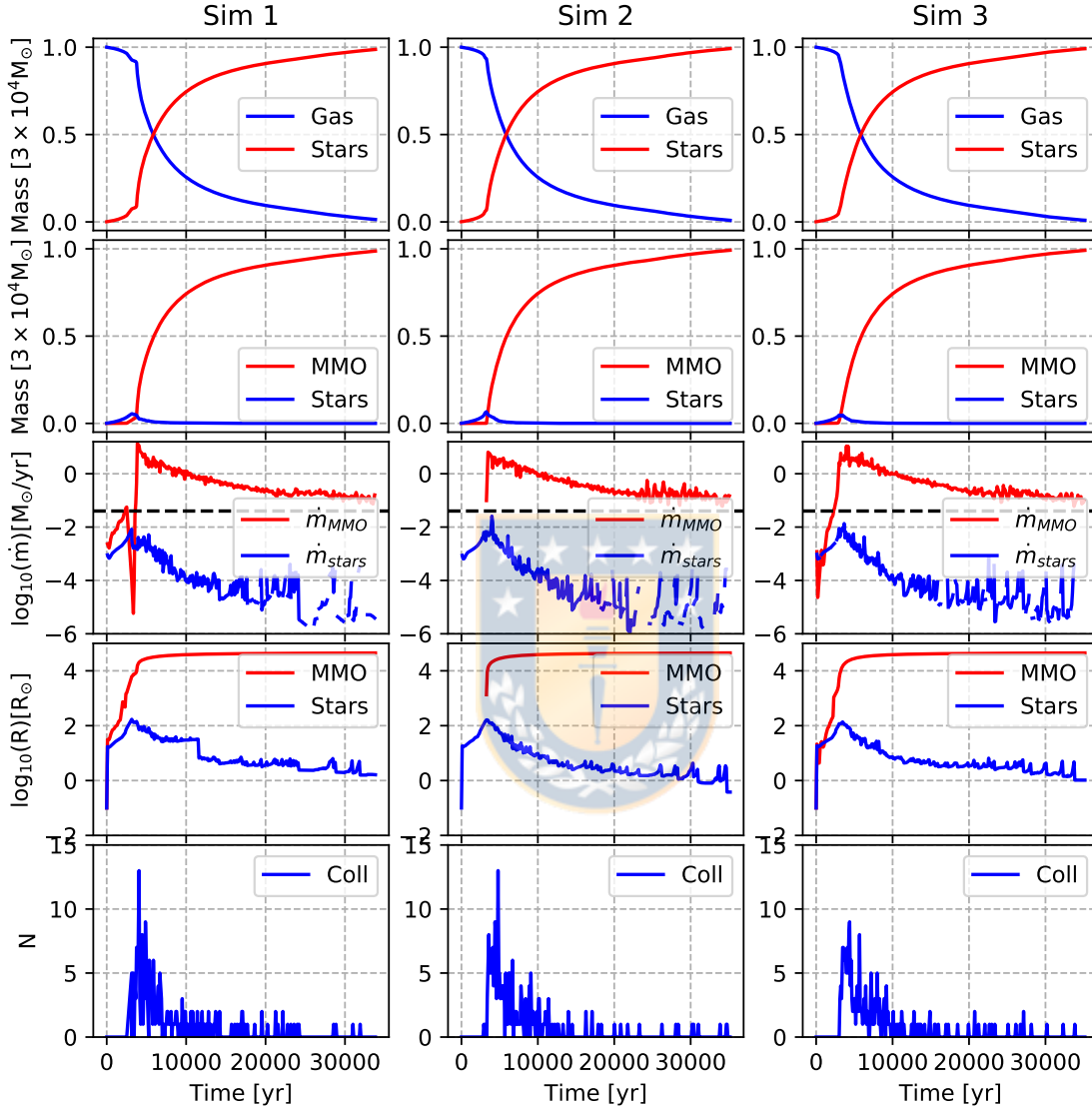


Figure 4.1.4: Evolution of the gas and protostellar mass for the simulations Sim1, Sim2 and Sim3 with an initial temperature of 8000 K (top panel). Comparison of the time evolution of the MMO mass and the total mass of the protostars without the MMO (second panel), accretion rate of the MMO with the mean accretion rate of the other protostars (third panel), where the black dashed line is the limit accretion rate $\dot{m}_{lim} = 0.04 M_{\odot}/\text{yr}$, for when a protostar passes to the 'SMS Track'. The radius of the MMO with the mean radii of the other protostars (fourth panel). Finally, the evolution of the collision rates over time (bottom panel).

near the center of the cluster and therefore have enough gas to accrete and increase their radii. Combining this with the fact that due to gravitational collapse, both gas and protostar densities increase, you get a higher collision probability leading to runaway collisions and a rapid absorption of these massive protostars by the MMO. As a result of the central collisions, only peripheral protostars survive in environments with less gas.

The moment when the system changes from being dominated by gas to being dominated by stellar masses corresponds to the formation of the MMO in the system, which occurs rapidly in a time less than 0.1 Myr. This could indicate that the system is not very sensitive to the initial configurations of the protostars or the gas.

As mentioned above, the high accumulation rates of the central objects are driven by a strong gas inflow, triggered by the general contraction of the gas cloud. As shown in the third panels of Fig. 4.1.4, the accretion rates of the MMOs in all simulations exceed for a long period of time the critical accretion rate $\dot{m}_{crit} = 0.04 M_{\odot}/\text{yr}$ determined by the black dashed line. At the same time, the MMOs enter the 'SMS track', increasing their radii and reaching radii of the order of $10^4 R_{\odot}$, which will be maintained practically until consuming all the gas. It will allow them to be the object with the highest probability of collisions. Therefore the swelling MMOs increase their cross sections resulting in runaway collision period. After consuming almost all of the gas, the accretion rates naturally decrease, which would possibly take the MMOs to the 'STAR stage' allowing them to enter the main sequence.

In our simulations the protostars that finally became the MMO were always close to or within the 10% of the closest stars to the cluster center, as shown in the second panels of Fig. 4.1.5, which explains why the protostars that finally became the MMO reach high accretion rates over a short period of time. This tells us that the initial period and the position of the protostars in the cluster is decisive to know which protostar will become the MMO. This may indicate that the protostars closest to the center of the cluster could be privileged to reach higher accretion rates, so reaching larger radii and masses, thus having a higher probability of becoming a massive object through high accretion rates and high collision rate.

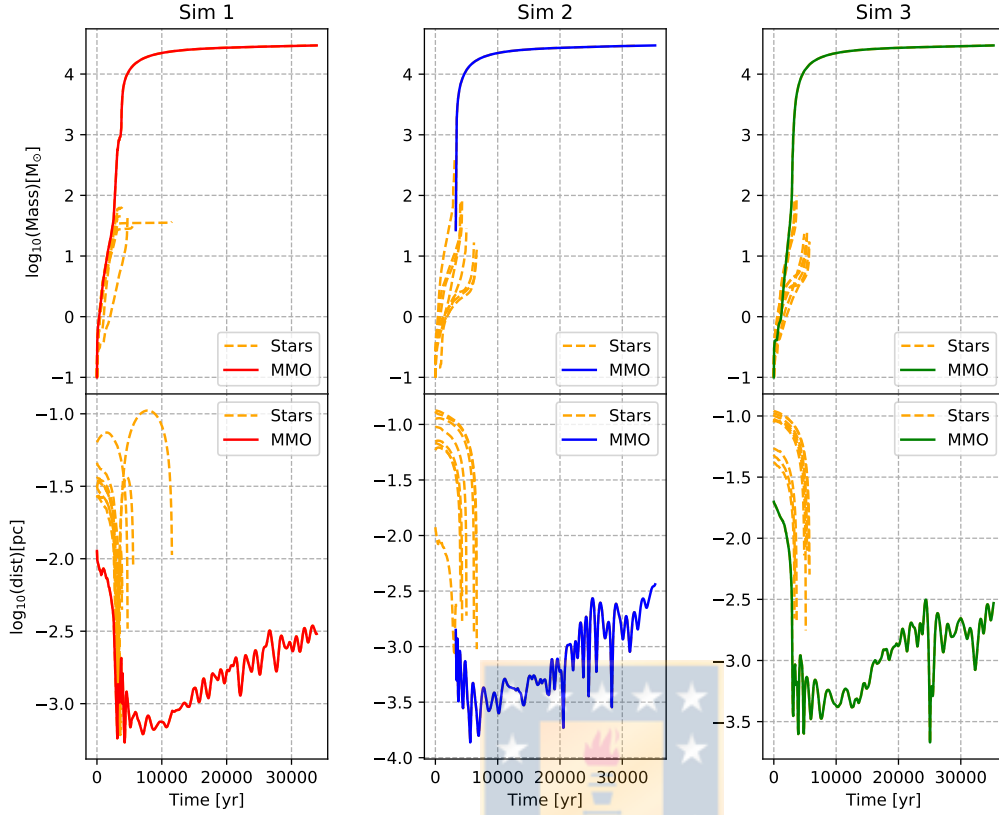


Figure 4.1.5: Time evolution of the correlation between the MMO mass together with the masses of the 9 MMOs in the system (top panel), and the distance from the center of the MMOs and the 9 MMOs in the system (bottom panel) for the three 8000 K simulations.

In the first and second panels in Fig. 4.1.5, we show the time evolution of the mass of the MMOs (solid lines) with the 10 most massive objects for each simulation (dashed lines) and the distance to the center of the cluster of these objects. It is observed that the simulations only form 'ONE' single central massive object, which fell to the cluster center and remained there until consuming most of the gas. The next 9 massive objects end up colliding rapidly with other protostars and finally with the MMO, as we can see in the lower panels; because these protostars fall rapidly towards the cluster center due to the gas inflow. This explains the small hill in the total mass of non-MMO protostars seen in the second panels of Fig. 4.1.4 around ~ 5000 yr. Thus the final low masses are from peripheral protostars, which remain on the periphery and have not yet collapsed due to the gravitational potential. This may indicate that these objects are actually solitary protostars that did not participate in some runaway mass accumulation

process and that they obtained their mass through gas accretion in their low-gas neighborhoods.

As the system evolves in time, collisions occur that result in different collision products, including some that will be ejected from the cluster. To understand in more detail the role of protostellar collisions in the evolution of the system, four categories of possible interactions that a protostar can have as the system evolves are defined:

- Single protostars: They are part of the cluster but not a collision product.
- MMO product: Protostars that collided with the most massive object.
- Collision product: Collisions of other less massive products.
- Escaper: Protostars that escaped from the cluster.

In our study, it is considered that a protostar escaped from the cluster when its distance is greater than $10 R_{gas}$ and also its kinetic energy is greater than its potential energy, which means that it is not gravitationally bound to the system.

In Fig. 4.1.6 we present the time evolution of the protostar fractions corresponding to the four categories presented above. We observe that in all simulations most of the protostars end up colliding with the MMO, only a small or null fraction collides forming other lower-mass products and zero protostars escape from the cluster. The high collisions rate with the MMO ($\gtrsim 90\%$) can be explained as follows:

Due to the high initial gas accumulation, produced by the rapid collapse, the radii of the protostars in the center of the cluster increase considerably, up to several $1000 R_{\odot}$. As a consequence of the inflated protostars, the probability of collisions increases due to their long cross sections, with the MMO being most inflated because it has the highest accretion rate and the highest mass, therefore it has the highest collision probability. Also adding to the fact that protostars tend to fall to the cluster center following the flow of collapsing gas, creating a suitable scenario for a runaway collision to occur.

In our simulations the only two mechanisms by which MMOs can obtain mass is through gas accretion and/or runaway collisions. In Fig. 4.1.7 we show the mass fraction obtained by collisions and the fraction obtained by accretion for

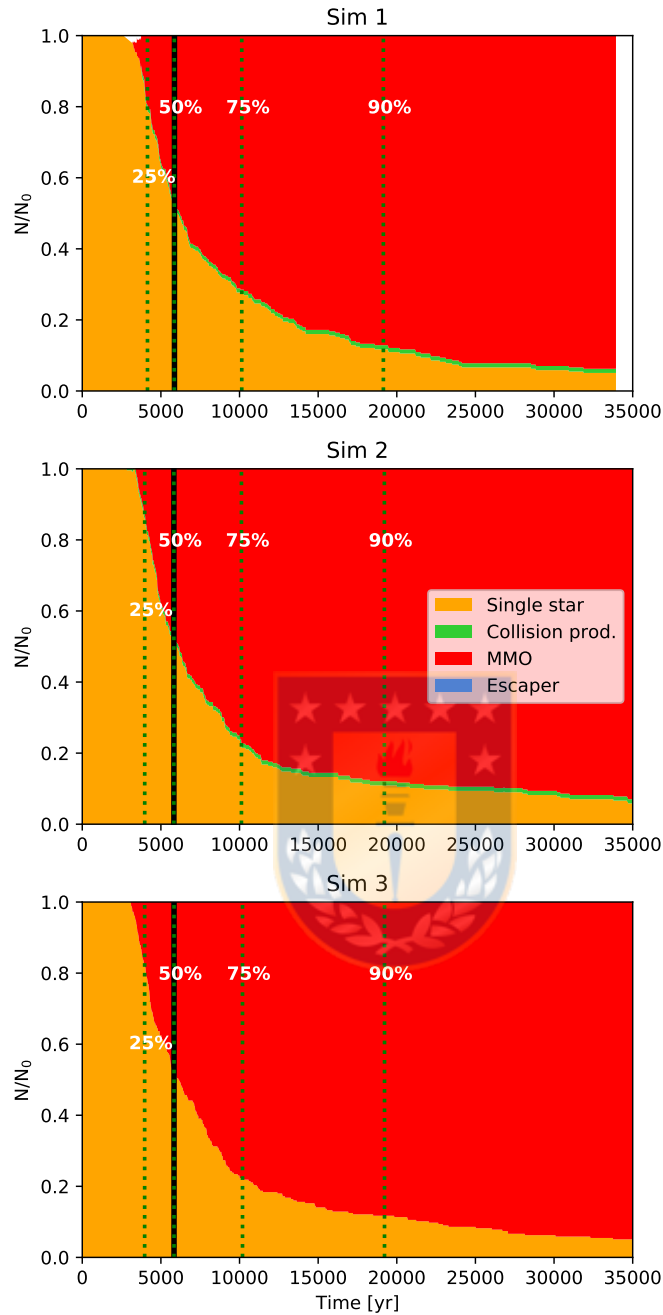


Figure 4.1.6: Time evolution of the fraction of stars belonging to four categories: (1) single protostars (orange, 'single star'), (2) stars that have collided with and are part of the most massive star in the system (red, 'MMO'), (3) stars that are part of other collision products (green, 'Collision prod.') and (4) escaper star (blue, 'Escaper'). The black dashed line shows the moment when the system is dominated by the protostellar mass. The green dotted lines are the times when the protostars accreted 25%, 50%, 75% and 90% of the gas mass. In all our simulations initially the protostars are single stars. The stars will actively interact with one another as they get larger from the gas they are accreting and in general, we see a fast increase in collisions with the MMO, few collisions with other collision products and a drop in the percentage of single stars. Also zero percentage of escapers.

the MMOs at the end of the simulation. We clearly notice a predominance of the accretion mechanism as the main way of the MMOs to obtain mass, reaching over $\sim 80\%$ of the total mass by this mechanism.

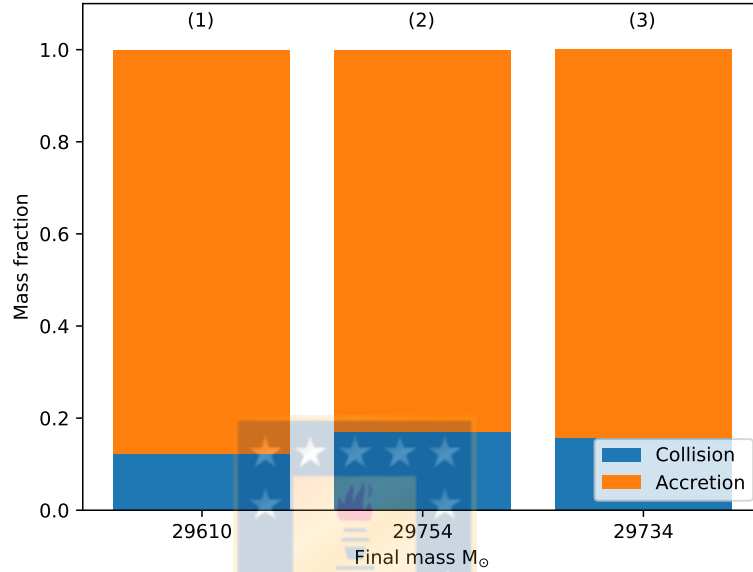


Figure 4.1.7: Final mean masses of the MMO for the three simulations from left to right with an initial temperature of 8000 K at 0.35 Myr. The blue color is the mass acquired through collisions and the orange color is the mass obtained by accretion. In all cases MMOs obtain their mass mostly through accretion.

Even when most of the protostars fall to the center (see Fig. 4.1.3) and collide with the MMO, their mass contribution is not much. This may be due to the rapid collapse of protostars, which means they don't have enough time to fatten up in mass and contribute with a larger fraction of mass to the MMO. In Fig. 4.1.8 the masses of the protostars that collided with their respective MMO are shown. We observe that most of the protostellar masses are of the order of $10^{0-2} M_{\odot}$ (with Q_1, Q_2, Q_3 and Q_4 less than $100 M_{\odot}$) where only isolated protostars are those that exceed these masses.

From Fig. 4.1.7 and Fig. 4.1.8 we deduce that collisions have a minor role in the evolution of the MMO mass and the main component is accretion. However, this only gives us an overview and it is possible that both the collisions and the gas have different periods of relevance in the evolution of the MMO. In Fig. 4.1.9 we show the mass and radius of the MMO that was obtained through accretion

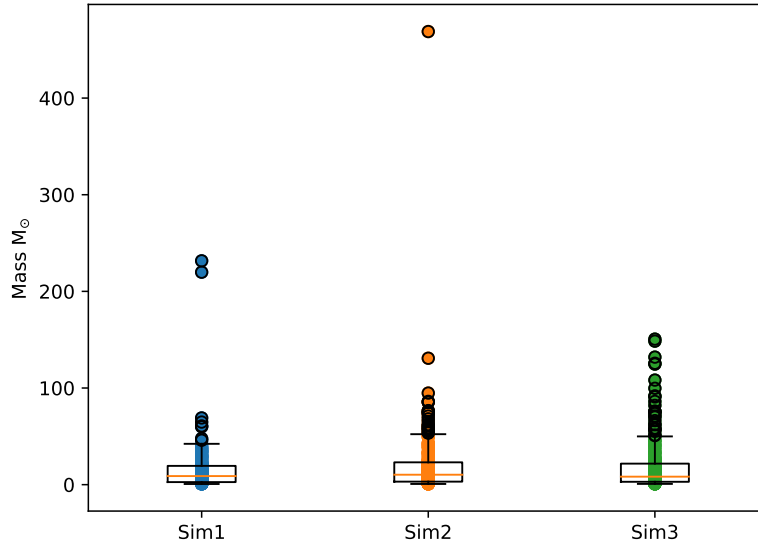


Figure 4.1.8: Box plot for the three simulations (from left to right) of 8000 K, of the protostar masses that collided with the MMOs. For all three cases the average masses are less than $10 M_{\odot}$.

(blue line) and collisions (orange line) over time. It is observed that throughout the evolution of the MMO, accretion plays the main role by which the MMO obtains mass, highlighting its importance in the initial periods, when the MMO only acquires mass through accretion and in all cases only near the highest point (where the protostar is most inflated and therefore most likely to have collisions) collisions start to appear. This is due to a combination of phenomena: First, it is natural that collisions occur after a period of time, since they need time to collapse and fall towards the center of the cluster. Second, for runaway collisions to occur it is better to have a large cross section to increase the probability of collisions and lead to high collision rates as observed in the last panels of Fig. 4.1.4. Also the collisions help to keep the MMO inflated with a large radius, allowing the growth to not slow down once the accretion starts to decay.

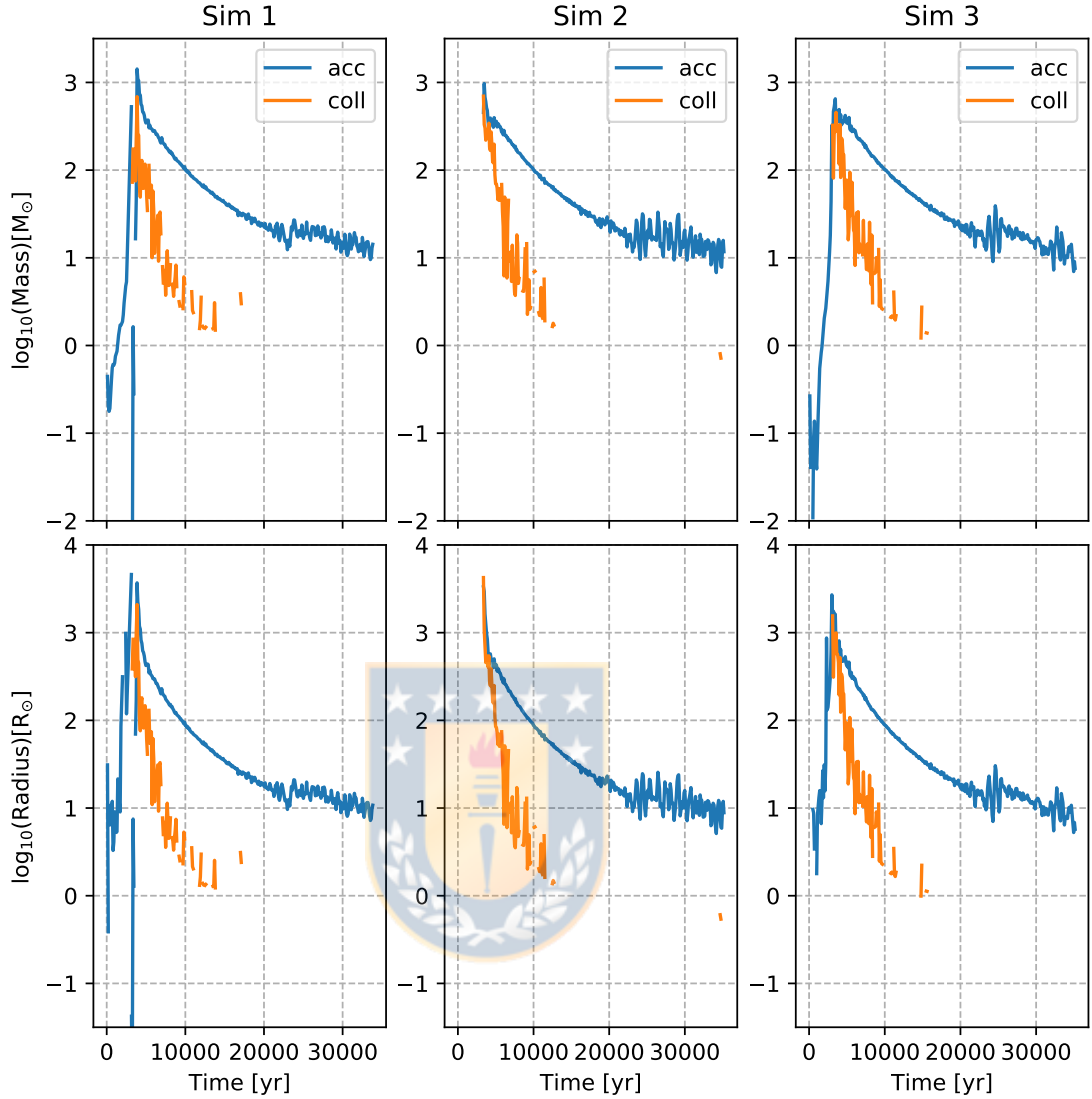


Figure 4.1.9: The top panels show the time evolution of the mass rate obtained by the MMO through collisions Δm_{coll} and accretion Δm_{acc} . The bottom panels show the increases in the radius of the MMO through collisions and accretion ΔR_{coll} and ΔR_{acc} . We observe that accretion plays a fundamental role in the entire evolution of the MMO for all cases, but it is especially relevant at the beginning of the evolution.

4.2 Colder temperatures

In this chapter we show the results assuming lower initial temperatures due to molecular hydrogen cooling. We perform simulations with initial temperatures of 5000 K, 1000 K and 500 K. We show the evolution of collisions, accreted mass, position of the MMO in the cluster and the main parameters and compare to the

8000 K simulations.

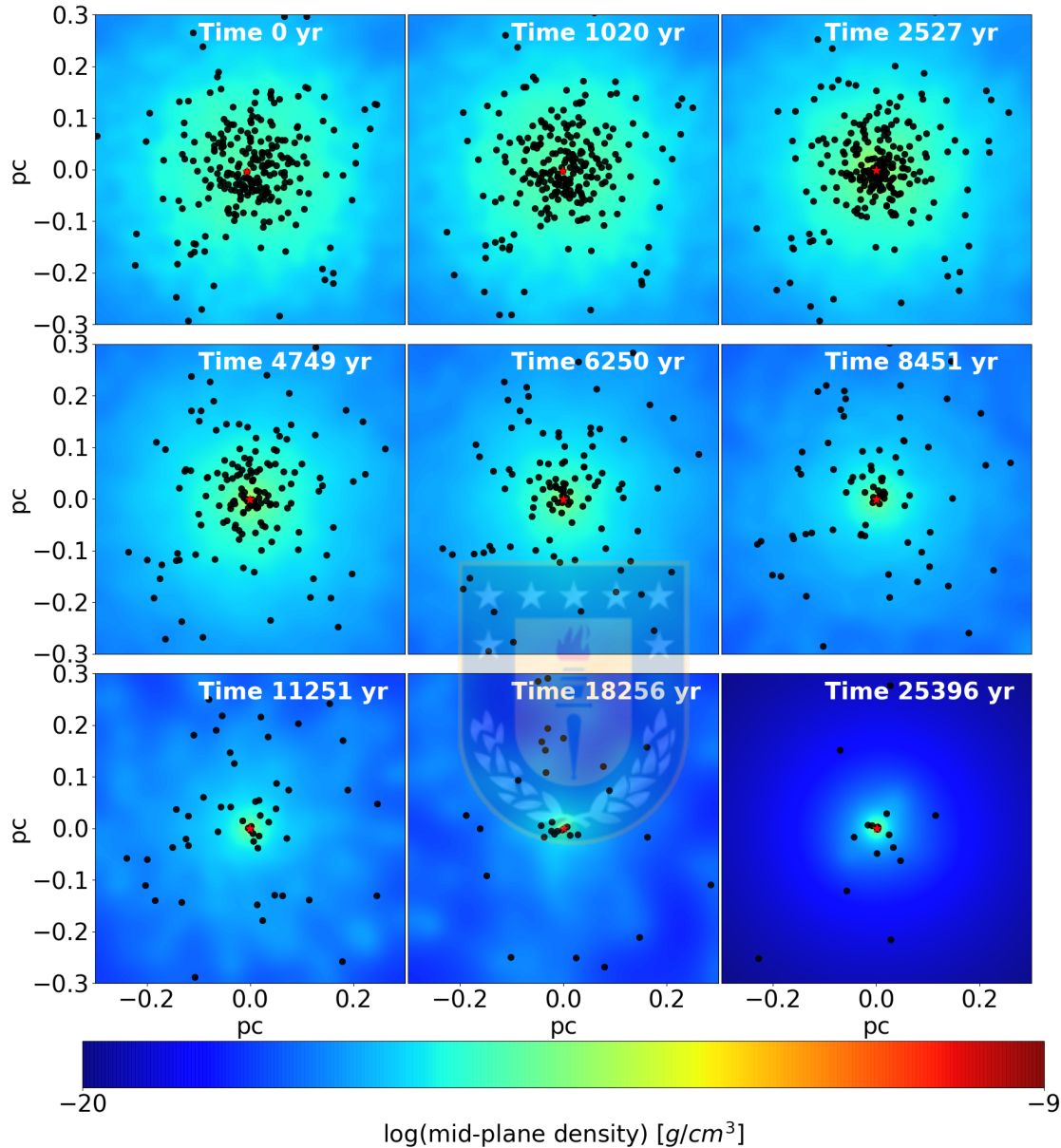


Figure 4.2.1: Density projections for a simulation with an initial temperature of 500 K at different times of a primordial gas cloud with an embedded protostar cluster. The black dots are the protostars and the red dot is the MMO of the cluster. A slight fragmentation is observed, as well as a rapid collapse after 10000 yr compared to the 8000 K simulations.

In Fig. 4.2.1 we show the evolution of the simulation with an initial temperature of 500 K, where a slight fragmentation is observed which is easier to observe in the last row of images and where the biggest difference is seen compared to the

8000 K simulations. We only observe that the collapse is faster, reaching a point similar to the 8000 K simulations in a shorter time.

In Table 4.2.1 we show an overview of the results obtained for the simulations with an initial temperature of $T = 5000, 1000, 500$ K and show the mean values for the simulations of 8000 K.

ID	T_{init} [K]	M_{MMO} [M_{\odot}]	\dot{m}_{MMO} [M_{\odot}/yr]	%	M_{gas} [M_{\odot}]	T_{mean} [K]	N_{star}	M_{star} [M_{\odot}]	N_{coll}	M_{esc} [M_{\odot}]
	8000	29699.8	0.695	98	324.1	8011.8	14	29701.5	242	0
4	5000	29633.7	0.959	99	389.8	5160.6	15	29635.8	241	0
5	1000	29857.8	1.032	99	165.8	1132.7	19	29859.7	237	0
6	500	29916.3	0.998	99	105.19	636.0	30	29920.4	226	0

Table 4.2.1: Summary of the mean values for the 8000 K simulations and simulations with initial temperatures of 5000 K, 1000 K and 500 K, from top to bottom. From left to right the columns correspond to the simulation name, final mass of the MMO, mean accretion of the MMO, percentage of the final mass of the MMO as a function of the total mass of the system, the final gas mass, mean temperature, final star number, final star mass, number of collisions and the total escaped mass.

From Table 4.2.1 a change in the evolution of the system is observed. For the simulation of 5000 K, 1000 K and 500 K we observe higher mean accretion rates for the MMOs ($\sim 1 M_{\odot}/\text{yr}$) than for the simulations of 8000 K where the mean accretion is approximately $\sim 0.7 M_{\odot}/\text{yr}$, which indicates that for colder simulations the evolution of the MMO occurs in a shorter time, reaching an accretion of 90% of gas by protostars, 5000 yr earlier than in the simulations of 8000 K. Also in all simulations we obtain an efficiency ($M_{\text{MMO}}/M_{\text{Total}}$) of the MMO of approximately 99%, which may be due to the initial instability of the gas. As the collapse of the system is mainly due to the instability of the gas, this strongly impacts the evolution of the MMO, because with higher instability, the gas falls to the center of the cluster faster and higher accretion rates are reached. On the other hand, for more stable systems, the gas collapses in a longer time and lower accretion rates are obtained. We use the ratio between the total mass of the gas and the Jeans mass $M_{\text{gas}}/M_{\text{Jeans}}$ as a quantitative measure of the instability of a configuration. For our initial conditions of gas mass, virial radius and temperature we explore an instability range of $M_{\text{gas}}/M_{\text{Jeans}} \approx 5 - 340$, from the highest temperatures to the lowest temperatures, as we can see in Fig. 4.2.2, where the efficiencies obtained for the different temperatures in this work and the

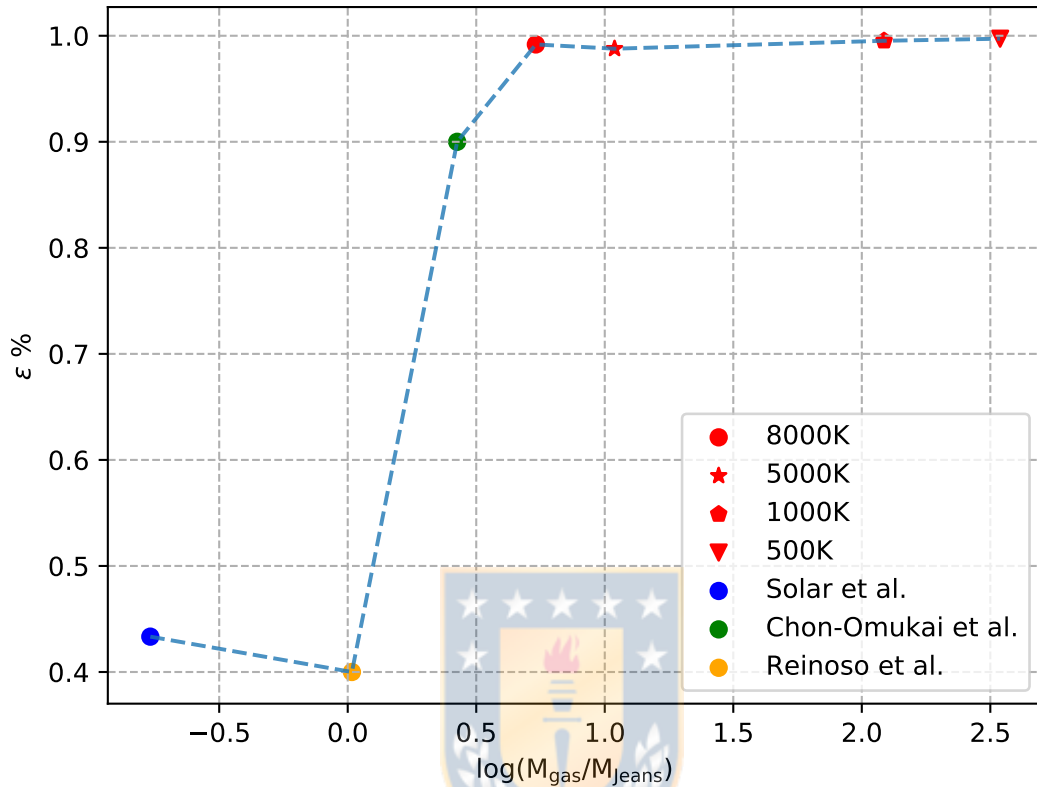


Figure 4.2.2: Efficiency of the MMOs as a function of $M_{\text{gas}}/M_{\text{Jeans}}$ for the simulations with different temperatures explored in this thesis (red points), Chon and Omukai (2020) (green point), Solar et al. (2022) (blue point) and Reinoso et al. in preparation (orange point).

efficiencies of the works Chon and Omukai (2020); Solar et al. (2022) and Reinoso et al. in preparation. Reaching high efficiencies ($\gtrsim 80\%$) for more unstable configurations. This means that the system is always unstable, producing a rapid initial collapse, where most of the mass is accreted, reaching a high efficiency and high absorption of the mass of the gas cloud, as observed in Fig. 4.2.2.

In Fig. 4.2.3 we show the evolution of the mass fraction for simulations with a temperature of 5000 K, 1000 K and 500 K from top to bottom. In general, very similar collapse is observed for all cases and only for the simulation of 5000 K a slightly slower collapse is observed around 20000 yr. For all simulations we observe faster collapse than for the simulations with an initial temperature of 8000 K, where more than $\sim 90\%$ of the gas mass was accreted before 15000 yr. In addition, the moment when 50% of the mass is accreted occurs approximately at the same

time, both in the simulations that consider molecular hydrogen cooling as well as atomic hydrogen cooling. The green dotted lines show the moments when 25%, 50%, 75% and 90% of the accreted mass are reached and the black vertical line indicates when the protostars have more mass than the gas and this dominates the system dynamics; in all cases with lower temperature these moments occur approximately at the same time. But compared it to the 8000 K simulations, the times when 75% and 90% of the mass have been accreted are earlier and closer together, which may indicate that cooling effects are reflected in the second half of the evolution of the system and the initial evolution is not sensitive to changes in the initial temperature in these ranges. Furthermore, we note that in these simulations the amount of escaped mass is still approximately zero.

The Fig. 4.2.4, Fig. 4.2.5 and Fig. 4.2.6 show the Lagrangian radii for the simulations with initial temperatures of 5000 K, 1000 K and 500 K. The first panels show the evolution of the protostars in the cluster, where a very similar collapse is observed for all simulations, collapsing rapidly and reaching a unification of the protostars in one single massive object before 5000 yr. This is expected, since the parameter variations are made in the gas and the protostars only interact gravitationally with the gas, which should not cause big changes in their dynamics. The protostars probably collapse towards the center due to the accretion of the protostars increasing in mass, producing an instability and leading to collisions and the formation of a central object.

Compared to the protostars, which show almost the same behavior for the simulations of 8000 K, 5000 K, 1000 K and 500 K, the gas has a faster collapse for simulations with low temperatures. The gas tends to collapse in a similar way in all cases, with a gradual contraction of all percentages of the Lagrangian radii of the gas and an early central collapse. However, the collapse of the gas is faster than in the simulations with higher temperatures, reaching a total gas contraction in approximately ~ 25000 yr. This is probably due to differences in gas pressure from fragmentation for simulations with lower temperature. As a result of fragmentation, high densities are not reached in the center of the cluster and therefore there is no pressure from the center outwards that resists the collapse of the cloud, as is it the case for higher temperatures. We observe small variations in the shape of the gas falling towards the center of the cluster for the 5000 K simulation, but this does not greatly affect the general results.

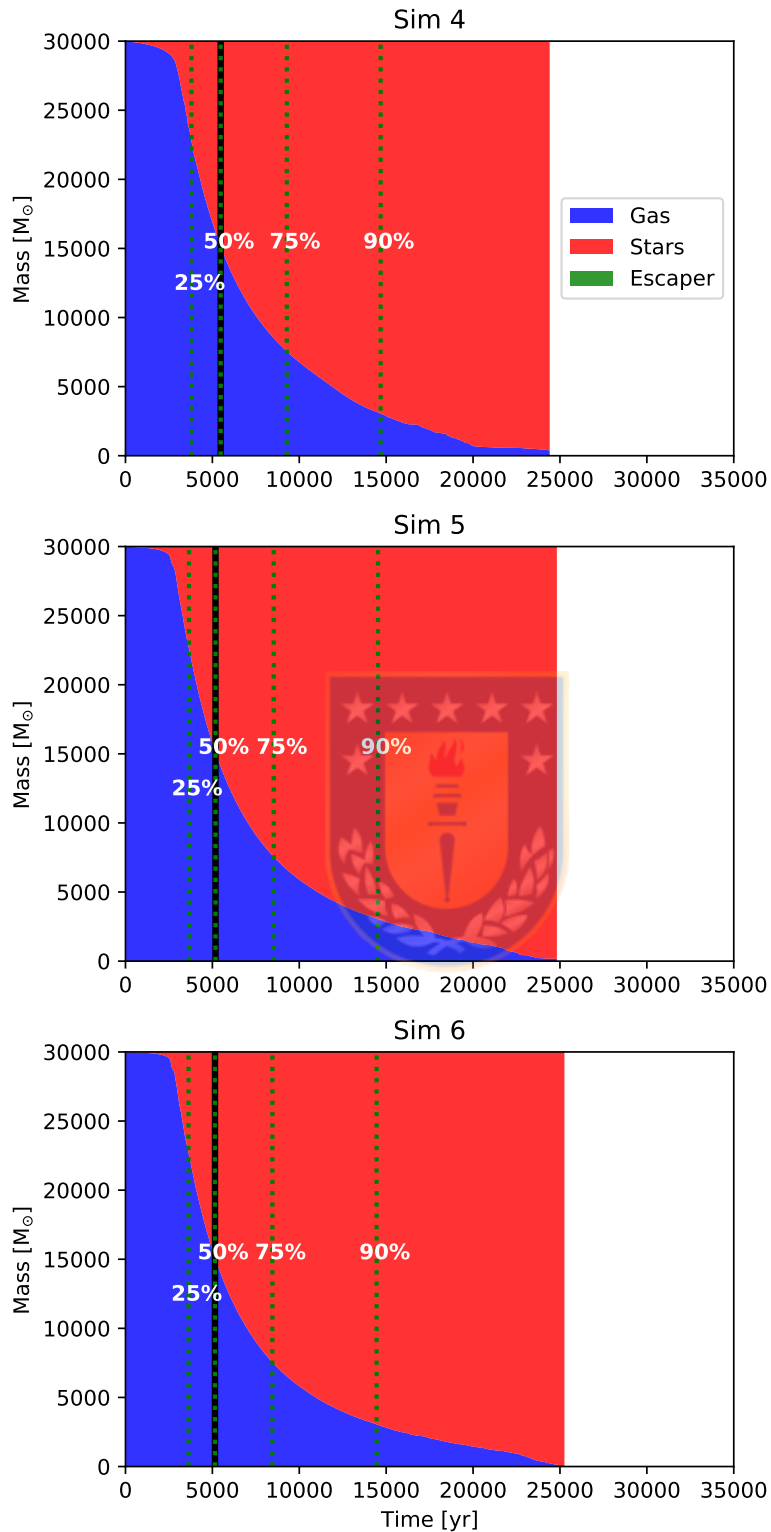


Figure 4.2.3: Time evolution of the mass fraction for the simulations with an initial temperature of 300 K, 500 K and 1000 K of the gas (blue zone), stars (red zone) and the mass that escaped (green zone), according to the escape criterion indicated above. The green dotted lines are the times when the protostars accreted 25%, 50%, 75% and 90% of the gas mass and the black solid line is the moment when the system is dominated by the protostars mass.

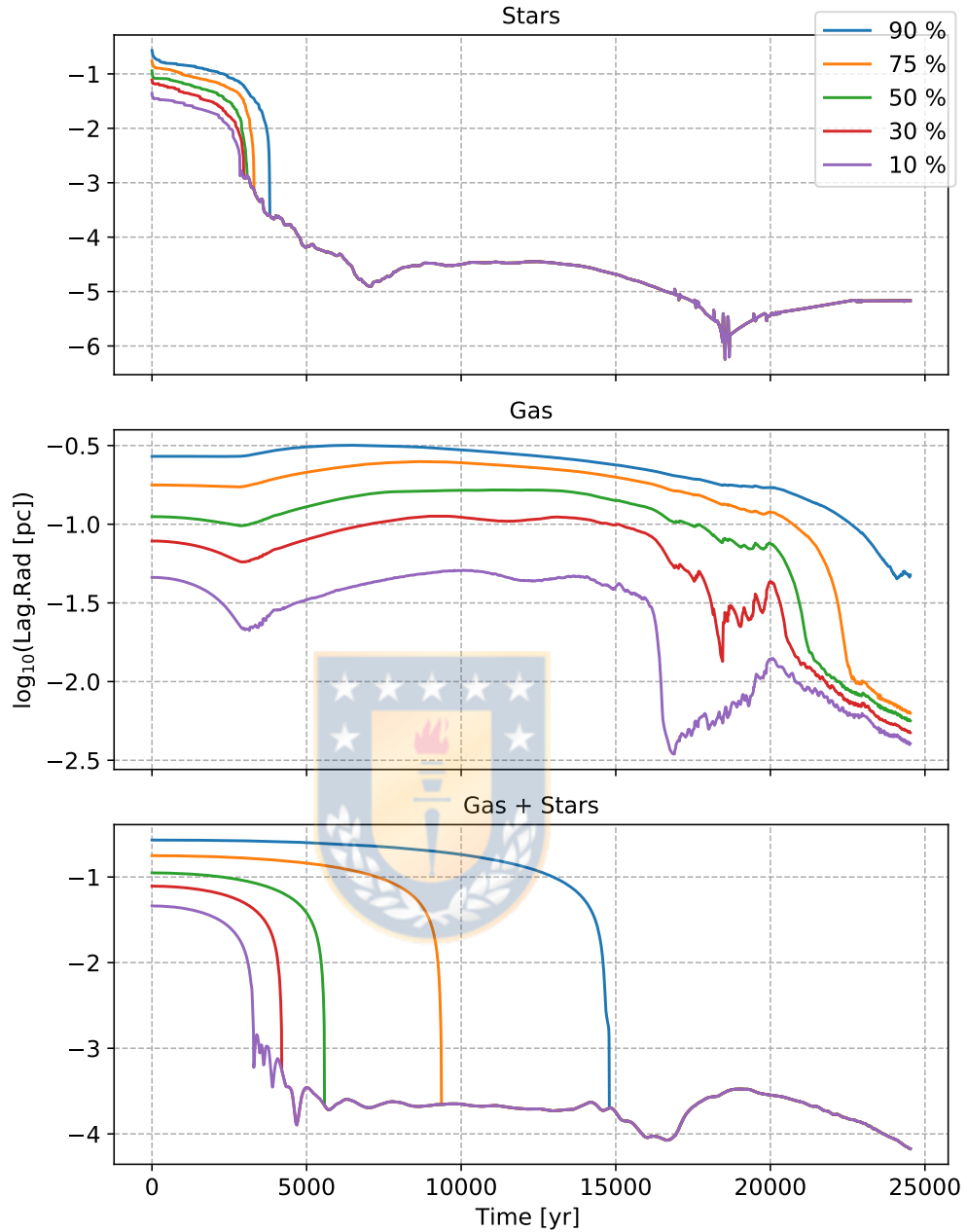


Figure 4.2.4: Time evolution of the 90%, 75%, 50%, 30% and 10% Lagrangian radii in the 5000 K simulations. In the top panel the Lagrangian radii for the protostars labeled as 'Stars' are shown, in the middle panel for the gas labeled 'Gas' and in the bottom panel the Lagrangian radii for the total system 'Gas + Stars'. In general we observe a similar behavior to the 8000 K simulations, with slight differences in the gas collapse.

In the bottom panel of Fig. 4.2.4, Fig. 4.2.5 and Fig. 4.2.6 the mass collapses to form an MMO. Again the behavior for all simulations is similar, except that the collapse of 75% and 90% of the mass for the simulations with temperatures of

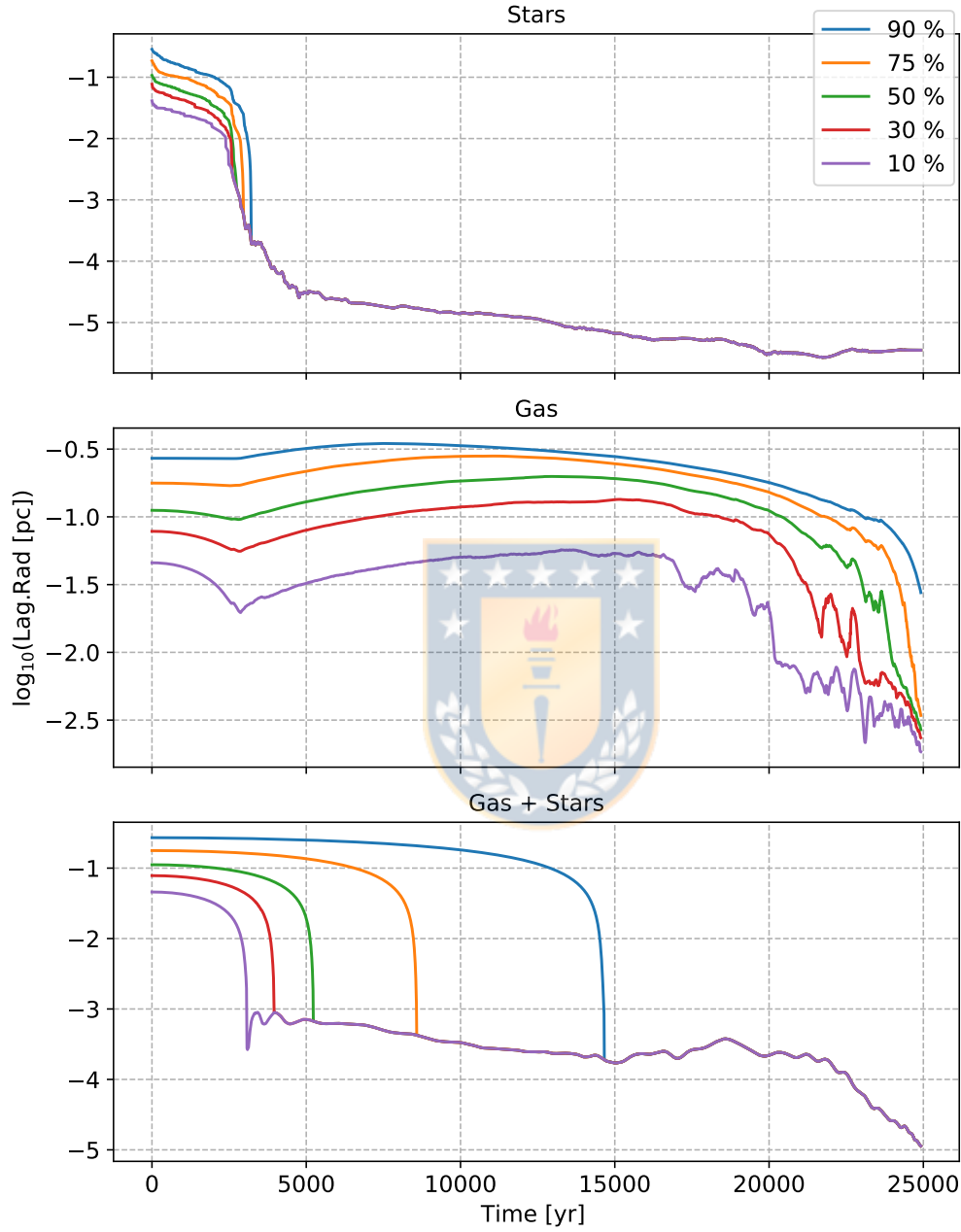


Figure 4.2.5: Time evolution of the 90%, 75%, 50%, 30% and 10% Lagrangian radii in the 1000 K simulations. In the top panel the Lagrangian radii for the protostars denoted as 'Stars' are shown, in the middle panel for the gas labeled 'Gas' and in the bottom panel the Lagrangian radii for the total system 'Gas + Stars'. Very similar development of the protostars as in the 8000 K simulation, but with a more rapid collapse due to lower pressure.

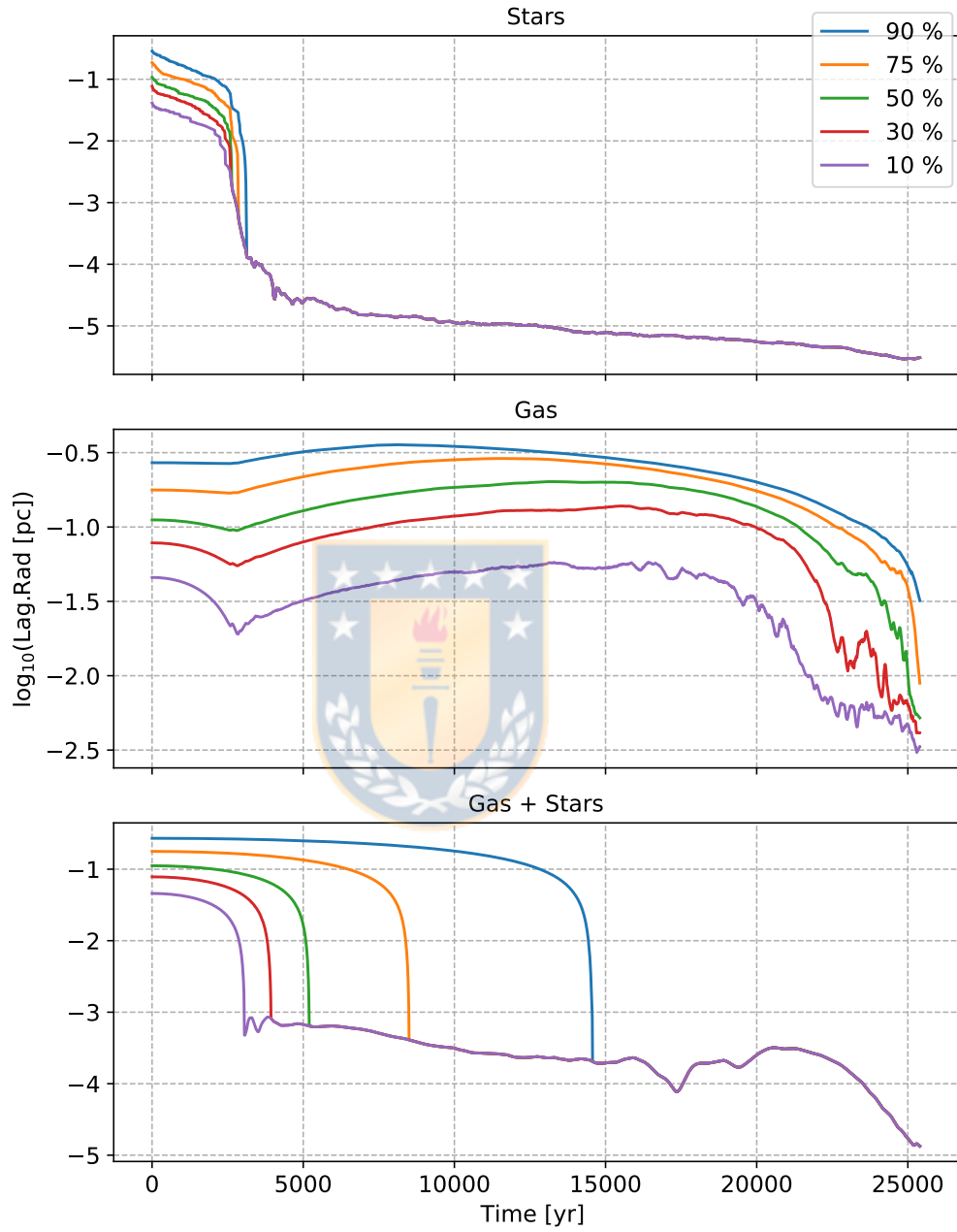


Figure 4.2.6: Time evolution of the 90%, 75%, 50%, 30% and 10% Lagrangian radii in the 500 K simulations. In the top panel the Lagrangian radii for the protostars denoted as 'Stars' are shown, in the middle panel for the gas labeled as 'Gas' and in the bottom panel the Lagrangian radii for the total system 'Gas + Stars'. With a very similar development of the protostars as in the 1000 K and 8000 K.

5000 K, 1000 K and 500 K occurs much earlier than for the higher temperature simulations. Which again indicates that the cooling has a stronger impact in the second half of the evolution after reaching a peak in the density of the gas produced by the contraction and formation of the MMO.

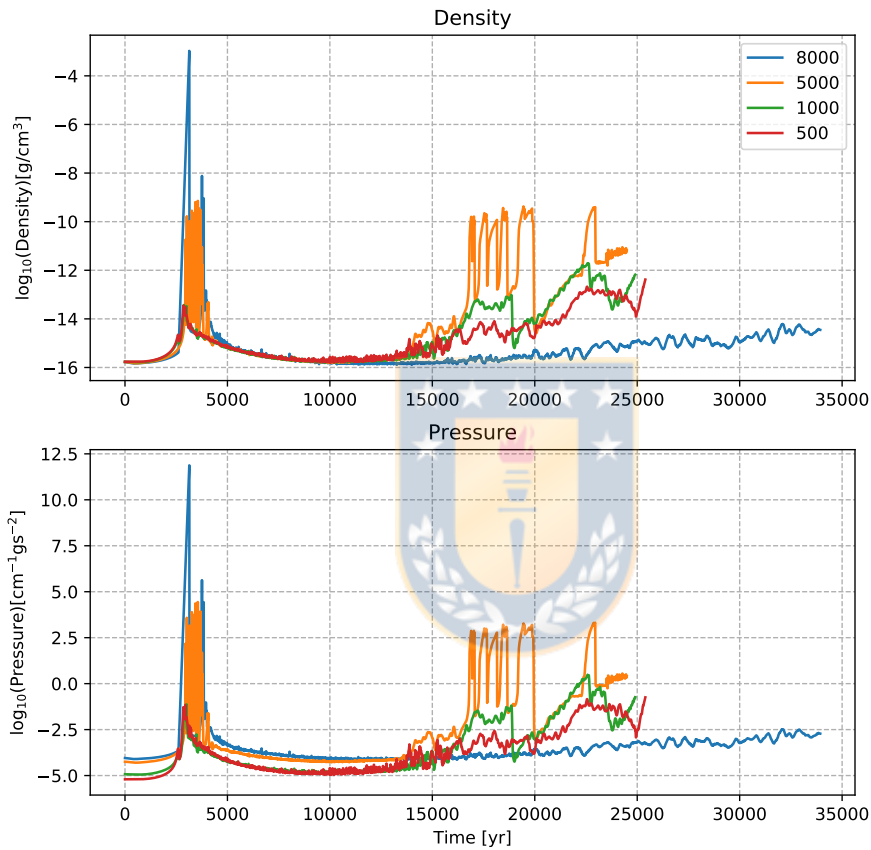


Figure 4.2.7: Time evolution of the mean gas density and pressure for the simulations with temperatures of 8000 K, 5000 K, 1000 K and 500 K. We observe higher densities and pressures at the beginning of the evolution for the higher temperature simulations.

As mentioned above, the faster collapse of the gas for the simulations with lower temperatures may be due to the different densities reached by the gas produced by the fragmentation. In Fig. 4.2.7 we show the mean density and pressure for all temperatures. It is clearly observed that for the simulations with temperatures of 8000K and 5000K, higher densities and pressures are reached as a result of the low gas fragmentation. These pressures in the center of the cluster resist the collapse

of the gas, directly impacting the accretion of the MMO and the protostars in the center of the cluster. After a period of high gas density for the simulations with higher temperatures, we observe that the system stabilizes staying mainly constant in density and pressure. On the other hand, for the simulations with lower temperatures, at the beginning of the evolution of the system high densities are not reached, allowing a free fall of the gas towards the center of the cluster. However, after a while the gas naturally begins to accumulate as a result of the collapse and begins to increase both its density and pressure. When the gas densities for the lower temperature simulations start to increase (~ 15000 yr) the amount of gas accreted is already $\sim 90\%$, therefore this should not have a huge impact on the evolution of the MMO.

Fig. 4.2.8 shows the gas mass fractions and the protostellar mass fractions (upper panels), the mass of the MMO and the total mass of the remaining protostars (second panels), the radius of the MMO with the mean radius of the remaining protostars (third panels) and finally the collisions rate (lower panels). In general similar behaviors are observed for all simulations, reaching a total gas accretion of $\sim 100\%$ and the dominance of an early MMO in the simulation. In the second panels we have slight differences where for the cases with initial temperatures of 1000 K and 500 K there is a lower accumulation of mass for the protostars different from the MMO (blue line), possibly due to a higher initial collision rate, triggered by a free fall of gas, with a less strong central pressure that resists collapse. In the third, fourth and fifth panels in Fig 4.2.8 we show that the general behavior of the accretion rate of the MMO, the evolution of its radius and the collision rates are approximately equal and also in all simulations a state of 'SMS TRACK' was reached, increasing the radius of the MMO, producing a more favorable scenario for runaway collisions.

In Fig. 4.2.9 we show the collision fraction of protostars in the four categories mentioned above. Compared to the simulations for 8000 K, in the simulations of 5000 K, 1000 K and 500 K, there are no collisions with other protostars, leaving about $\sim 20\%$ of single protostars and in general all simulations have the same collisions behavior. Unlike mass, which is transferred much faster to protostars by accretion, collisions are not highly affected reaching a similar shape and number of collisions in the same times. From these graphs we also observe that the collisions do not occur so quickly, but rather it takes a little time to create favorable

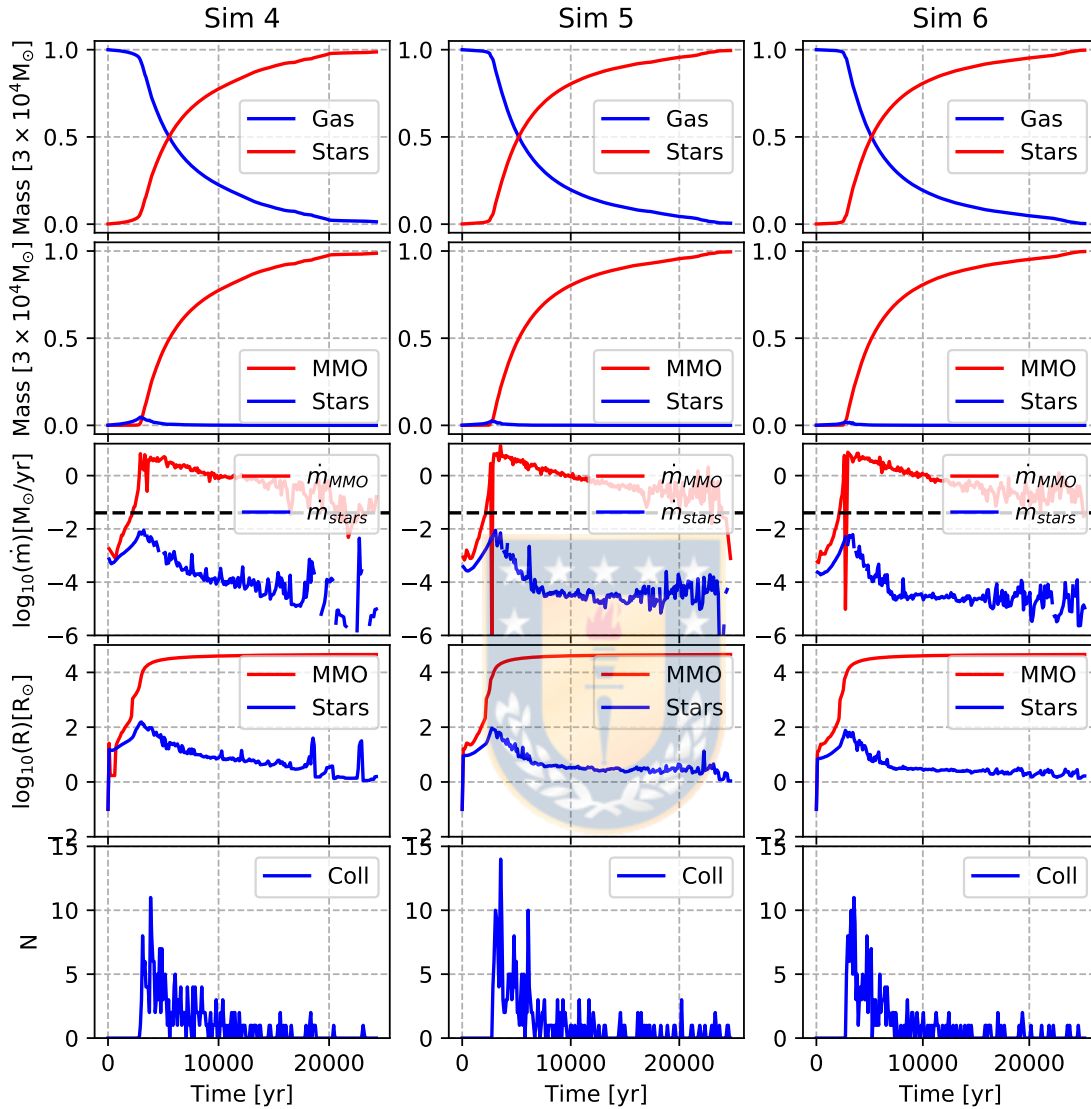


Figure 4.2.8: Evolution of the gas and protostellar mass for the simulations Sim4, Sim5 and Sim6 with an initial temperature of 300 K, 500 K and 1000 K (top panel). Comparison the time evolution of the MMO mass and the total mass of the protostars without the MMO (second panel), the accretion rate of the MMO with the mean accretion rate of the other protostars (third panel), where the black dashed line is the limit accretion rate $\dot{m}_{lim} = 0.04 M_{\odot}/\text{yr}$, for when a protostar passes to the 'SMS Track'. The radius of the MMO and the mean radii of the other protostars (fourth panel). Finally, the evolution of the number of collision over time (bottom panel).

conditions for a runaway collision, allowing the protostars to grow in mass through accretion, and increase their cross section for a higher probability of collisions.

In the cases where the gas is colder, it is likely that due to gas fragmentation, which translates into lower accretion rates, the main mechanism by which the MMO obtains mass is not necessary accretion, but rather collisions with new stars born from fragmentation or fattened protostars due to slower collapsing.

In Fig. 4.2.10, we show the mass fractions of the MMOs obtained by accretion and by collisions of the 10 most massive objects of all simulations. It is observed that for all simulations the accretion continues to predominate as the main mechanism by which the MMO obtains mass; indicating a low impact of the change in temperature on the evolution of the system and the main mechanism by which the MMO obtains its mass. While accretion is the main means by which the MMO obtains mass for both high temperature and low temperature simulations, we can see that collisions contribute $\sim 20\%$ of the MMO mass and this percentage apparently decreases for the coldest simulations. This may be due to the fact that as a result of the fragmentation due to low temperatures, the accretion rates are reduced, and therefore on average the protostars grow less in mass before colliding with the MMO. As we can see from the previous figures, the periods where the protostars grow more in mass and radius are the first moments in the evolution, when a density peak begins to be reached in the center of the cluster, which is reduced for the simulations with lower temperature since a lower central density is reached and therefore lower accretion rates and a lower contribution to the MMO.

In Fig. 4.2.11, we show the masses of the protostars that collided with the MMO in all simulations. A clear tendency is observed that in all simulations very high masses are not reached except for some isolated cases, which explains their low contribution to the final mass of the MMO. However, on average at least 50% of the masses that collide with the MMO of the simulations with higher temperatures are on the simulations with lower temperatures.

In Fig. 4.2.12 we show more precisely the mass (Δm) and radius (ΔR) of the MMO acquired through accretion and collisions for all temperatures. The top figures show the mass and radius acquired by the MMO through collisions, where apparently the contributions of the 1000 K and 500 K simulations decay faster, therefore there would be a smaller contribution to the mass of the MMO through

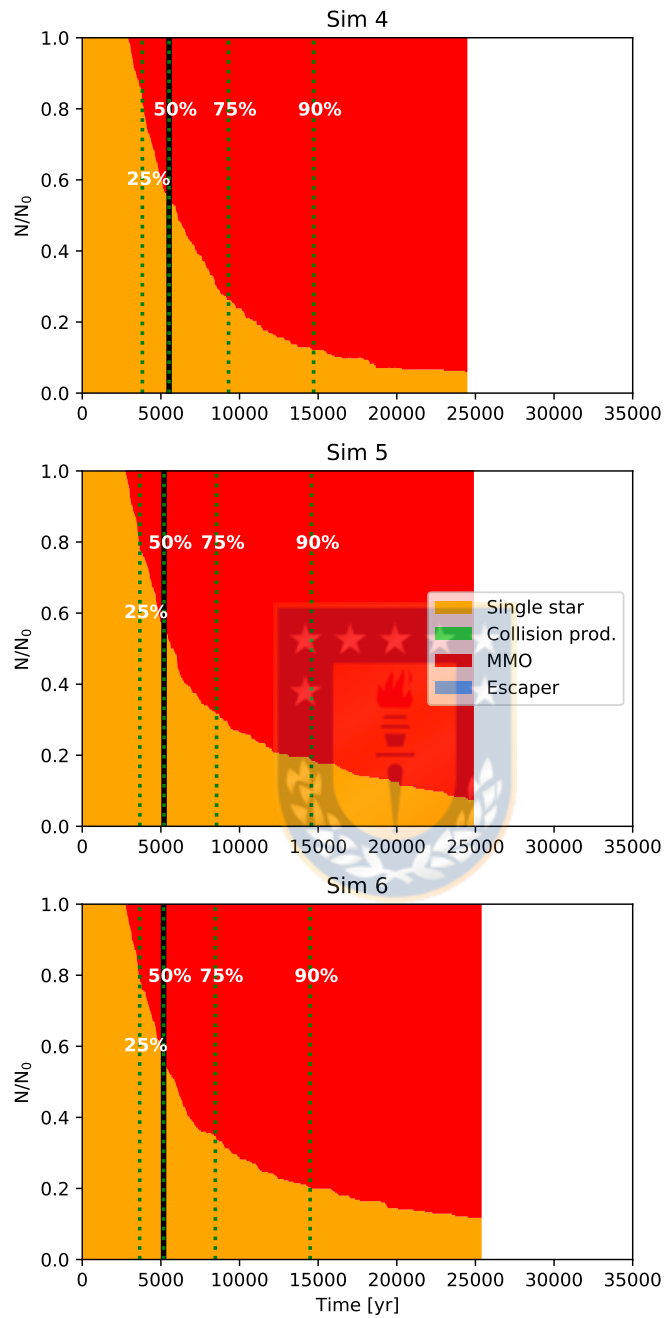


Figure 4.2.9: Time evolution of the fraction of stars belonging to four categories: (1) single protostars (orange, 'single star'), (2) stars that have collided with and are part of the most massive star in the system (red, 'MMO'), (3) stars that are part of other collision products (green, 'Collision prod.') and (4) escaper star (blue, 'Escaper'). The black solid line shows the moment when the system is dominated by the protostars mass. The green dotted lines are the times when the protostars accreted 25%, 50%, 75% and 90% of the gas mass.

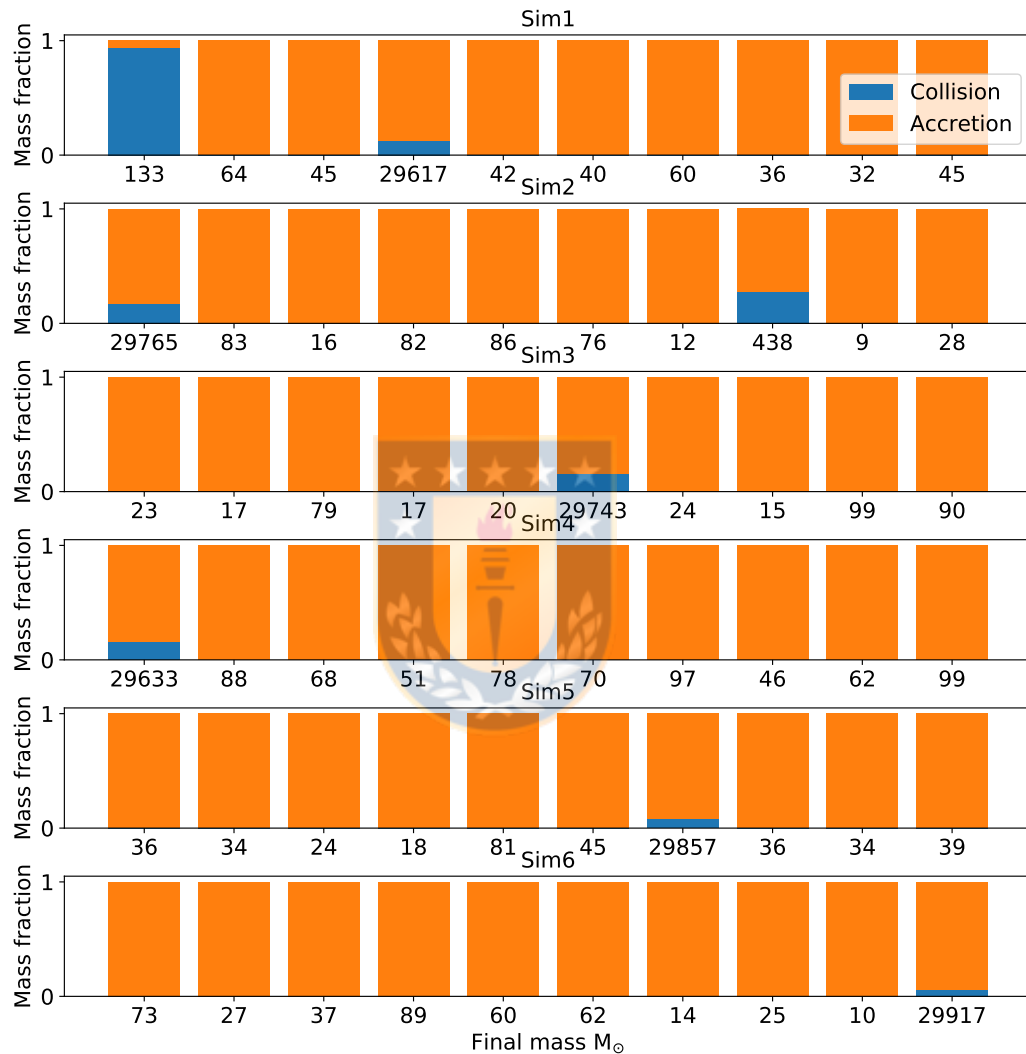


Figure 4.2.10: Final masses of the 10 most massive objects in all simulations performed to 0.25 – 0.35 Myr. The blue color is the mass acquired through collisions and the orange color is the mass obtained by accretion. It is noted that accretion is the predominant means by which massive objects obtain mass for all temperatures explored here.

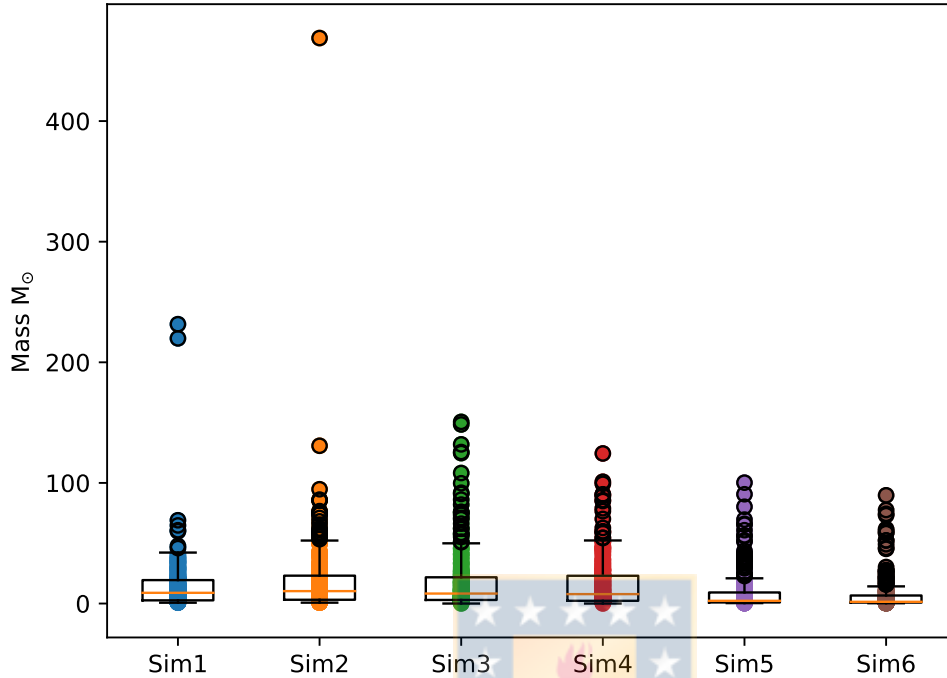


Figure 4.2.11: Boxplot for the three 8000 K simulations and the 300 K, 500 K, 1000 K simulations, in this order from left to right for the masses of protostars that collided with the MMOs. There is a slight incline from larger masses to higher temperatures.

collisions. In addition to this slight difference, no great difference is observed for the different temperatures. In the middle panels, the mass acquired by the MMO through accretion is shown. By this mechanism the MMOs of the 500 K, 1000 K, 5000 K and 8000 K simulations acquire their mass, where the contributions of collisions are sporadic peaks in the evolution of the MMO. As for the case of 8000 K, in the simulations with lower temperature, accretion plays a fundamental role in the initial evolution of the MMO. Since this is the only way for the MMO to acquire mass, increase its radius and be the object with the highest probability of collisions. We observe that the highest point of the mass obtained by accretion is synchronized with the period of collisions, since these are closely related because the accretion increases the cross sections of the protostars, causing more collisions. This means that in the moment of more accretion, there is a higher probability of collisions.

In the last panels we show the total Δm_T and ΔR_T acquired by the MMOs, where we can clearly see moments in which the MMOs do not acquire mass or their accretion rate drops drastically. Apparently these short famine periods occur earlier for higher temperatures. This is because when the gas collapses, high densities and therefore high pressures are reached in the gas. This translates into lower accretion rates as a result of the pressure resisting to the gas collapse, preventing it from falling into the MMO. We can verify that those moments of low accretion occur when the densities and pressures of the gas increase, as can be seen in Fig. 4.2.7.

Just as for the MMO the accretion plays a fundamental role to obtain its mass, for the following massive objects it also seems to be the case. In Fig. 4.2.10 we show that clearly the way in which most of the most massive protostars obtain their mass is by means of accretion. But it seems to be more likely that there are collisions with other protostars for higher temperatures.

At the end of the simulation, we determine the final mass of the MMO, its radius, mean accretion rate and the total number of collisions. The results are presented in the Fig. 4.2.13.

Starting with the maximum mass that the MMO reaches by the end of each simulation at different temperatures, we observe that the maximum mass is practically the same for all simulations, where they all consume almost all available gas, there being a difference of the final masses of the MMOS of only $300 - 400 M_\odot$ for the different temperatures, which corresponds to 1.33% of the total mass.

Observing the radii of the MMOs in the bottom left panel of Fig. 4.2.13 we notice that their behavior apparently does not behave monotonically, i.e. it does not decrease or increase monotonically at low or high temperatures, but rather It has two behaviors. First, the radius tends to decrease for higher temperatures, probably due to a combination of higher mean accretion rates and larger final masses for lower temperatures, leading to larger final radii for lower temperatures. Second, since lower temperature simulations tend to have higher accretion rates, they consume most of the gas quickly and therefore their MMOs start to reduce their radius earlier in the evolution, due to lower final accretion rates. Compared to the simulations with temperatures of 8000 K, their accretion is limited by the gas pressure, which causes them to remain for a longer period of time with

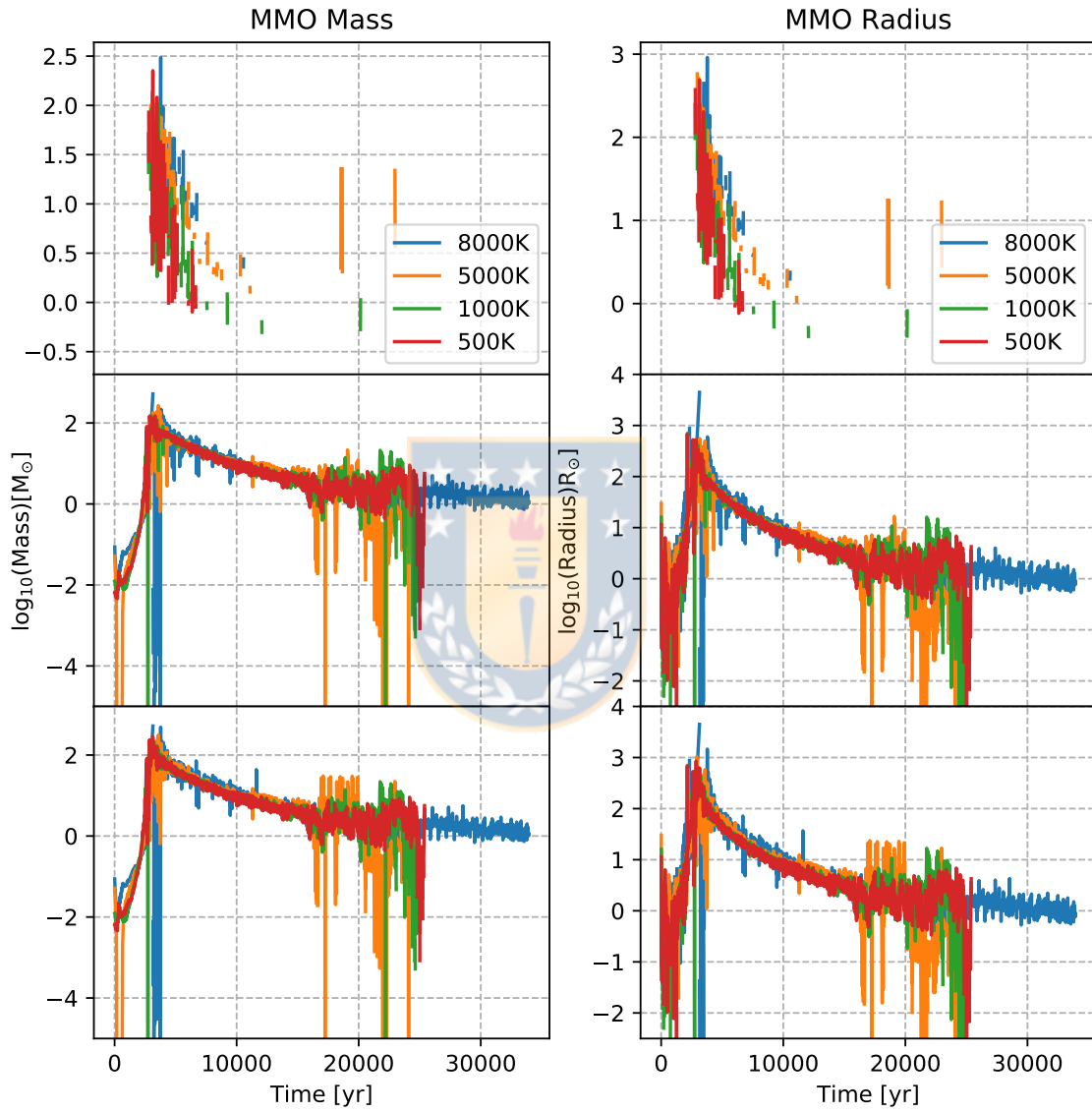


Figure 4.2.12: The left panels show the time evolution of the mass obtained by the MMO through collisions Δm_{coll} , accretion Δm_{acc} and the total mass Δm_{Tot} in the time for all simulations. The right panels show the increases in the radius of the MMO through collisions and accretion ΔR_{coll} , ΔR_{acc} and the total radius ΔR_{Tot} in the time for all simulations.

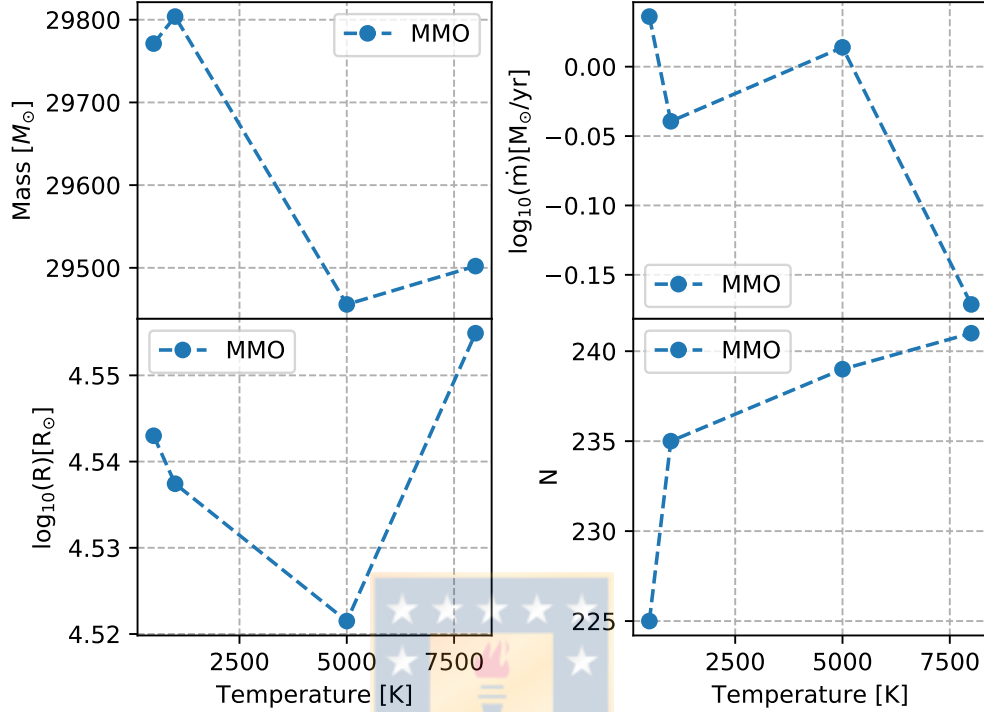


Figure 4.2.13: Parameters of the most massive object as a function of the initial temperature in each simulation. Mass reached at the end of the simulation (upper left), mean radii (lower left), mean accretion rates (upper right), and number of total collisions at the end of the simulation (lower right).

constant accretion rates, reaching more swollen final states on the radii.

Unlike the radius, we see a clear trend in the number of collisions for the different temperatures, where there is a trend of more collisions for the higher temperatures, probably because in the simulations with higher temperatures the mean speeds of the protostars are a little minor. Also, we notice that most of the collisions always occur close to the time of the MMO formation, around 6000 yr.

Finally we observe in the mean accretion rate for the MMO a clear trend of lower accretion rates for higher temperatures, although in all cases the accretion is around $\sim 1 M_{\odot}/\text{yr}$, which explains the rapid formation and evolution of the MMO, the pressure difference resulting from fragmentation may come to play a major role in the evolution of the MMO. This is because the change in temperature does not have an impact on the first moments of the collapse and on the formation of the MMO in the cluster, but it does seem to have an effect on the later stages,

because it directly affects the collapse of the gas and hence accretion, which is the main means by which the MMO acquires mass.



Chapter 5

Discussion and conclusions

5.1 Summary and conclusions

In this thesis, a numerical self-consistent implementation has been presented to investigate the possibility of SMBH seed formation through collisions and accretion. For this purpose three-dimensional multi-physics simulations including hydrodynamics and N-body dynamics were performed using the Smoothed Particle Hydrodynamics Tree code FI and the Hermite predictor-corrector code Ph4 for N-body dynamics in the AMUSE framework. These were combined with realistic accretion recipes and the sink creation method proposed by [Hubber et al. \(2013\)](#).

We performed a serie of simulations using the AMUSE framework of a protostellar cluster embedded in a compact gas cloud at very low metallicity, both initially following a Plummer density profile ([Plummer, 1911](#)) and varying the initial temperature of the gas. Our main result is that the collisions and accretion model is a possible candidate for the formation of SMBH seeds. Even for different gas temperatures, in all simulations the formation of a central massive object occurs. However, in our simulations the radiative feedback of the stars is not implemented, which would cause the internal energy of the gas to increase, leading to a high increase in its kinetic energy in long time periods. This implies that at late times the total energy of the gas would be positive. However, the total energy of the system is always maintained in a virial equilibrium. This can affect the fragmentation in lower-temperature simulations, preventing the necessary densities for the formation of protostars.

Investigations of the formation of SMBH seeds incorporating a hydrodynamic treatment provide more information on the possibility of the formation of SMBH seeds through collisions and accretion, allowing us to know how the gas evolves in these scenarios and how the gas temperature affects the formation of an MMO. In our work, we first present the results simulating a dense primordial gas in its atomic phase, with a temperature of 8000 K. We show the relationship between the mass of the gas and protostars, the accretion rates of the MMO and protostars and relationships between the different types of collision products. Also assuming possible cooling by molecular hydrogen, we explore the possibility of SMBH seed formation for gas clouds with temperatures of 5000 K, 100 K and 500 K. Our results can be summarized as follows:

For the hottest gas cases (8000 K) corresponding to atomic hydrogen cooling, the formation of a SMBH seed occurs rapidly and includes almost all of the mass in the system. Thanks to the high temperatures of the gas, the fragmentation of the gas is inhibited and it collapses isothermally towards the cluster center, reaching high densities allowing an ideal scenario for the formation of protostars as well as high accretion rates. Thanks to the gas inflow, the protostars are dragged towards the cluster center, causing early periods of runaway collisions and a rapid predominance of the MMO in the cluster. We observe that due to the rapid gas accumulation, the protostars in the cluster center grow in mass and inflate their radii caused by the high accretion rates. The inflation of the radii leads to larger cross sections, which increases the probability of collisions, leading to an early period of runaway collisions, with the protostars near the center being most likely to become the MMO. Since the MMO quickly reaches an accretion peak, its radius increases explosively monopolizing cluster collisions. Also due to the rapid collapse and collisions of protostars, the main mechanism by which the MMO acquires its mass is through accretion. Due to the prevention of fragmentation, the gas quickly reaches high densities, causing the pressure in the center of the cluster to increase exponentially, this produces an outward pressure, resisting gravitational collapse. This triggers moments of low or no accretion, which causes the gas to collapse more slowly, allowing a monolithic collapse. This delay allows for more homogeneous accretion rates of the protostars, allowing not only the MMO to accumulate large amounts of mass through accretion. The uniform accumulation of the gas by the protostars causes an increase in the mean radius, allowing a

higher probability of collision.

For the simulations with temperatures of 5000 K, 1000 K and 5000 K we find very similar behaviors compared to the case of 8000 K, where the gas collapses towards the center of the cluster due to the Jeans instability and quickly forms an MMO. Due to the high accumulation of gas in the center of the cluster, as well as for the simulations with higher temperatures, the beginning of the evolution of the MMO is marked by high accretion rates. Thanks to the fragmentation triggered by low temperatures, the densities reached in the center of the cluster are lower and therefore also the pressure. This means that there is no strong central pressure that is related to the collapse of the gas and regulates the accretion of the MMO. Therefore, we observe that higher accretion rates are reached for simulations with lower temperatures, which leads to a faster system evolution, reaching almost all of the gas accretion at ~ 0.25 yr. As in the first part of the evolution of the system the collapse is not regulated by an outward pressure, high accretion rates are reached, however with time the gas begins to accumulate increasing the pressure, but when the pressure is high enough to resist the gas collapse, $\sim 90\%$ of the gas has already been consumed.

Naturally, the variation in temperature affects the evolution of the cluster, either delaying its collapse or allowing high accretion rates. However, all our results strongly suggest that the interaction between gas and stars can lead to the formation of a single massive central object of the order of $\sim 10^4 M_{\odot}$ being a plausible scenario for the formation of a SMBH seed.

5.2 Discussion

Our research provides an intuition about the formation of SMBH seeds including gas and stellar dynamics, as well as a first approximation considering different types of cooling modeled via different isothermal temperature evolutions corresponding to the presence of atomic hydrogen or molecular hydrogen cooling. The numerical implementation of the gas helps us to elucidate how its interaction with protostars affects the formation of SMBH seeds in the early Universe. However our implementation is limited, since in our simulations of compact gas clouds, with virial radii of 0.14 pc we extended the limits of single smoothing length codes, requiring the implementation of sink particle creation to be able to resolve high-

density zones, typically in the vicinity of the MMO.

In our model, in the interactions between the protostars, collisions between them are allowed, providing a mechanism for the formation of a central massive object in the cluster. However, we did it in a simplified way, without considering mass loss during collisions, assuming an invariance in the densities of the resulting protostars, etc. The implementation of a more complete model to characterize the collisions between the protostars is necessary, since it is possible that very violent collisions do not result in a collision product in the form of protostars. In addition, the mass loss during the collisions can generate an impact on the evolution and the final mass of the MMO in the cluster as can be seen in [Alister Seguel et al. \(2020\)](#).

The gas dynamics was modeled with the FI code, solving the gas dynamics including the thermodynamic equations in a Lagrangian framework. Using an N-body code and the Bridge method, we calculate the gravitational interaction between the protostars and the gas. However, even when the gas is modeled numerically, we still neglect its chemical evolution, radiation and feedback phenomena. It is modeled here as a monoatomic gas, assuming a fixed abundance of 75% mass in **H** and 25% mass in **He** and no interactions with radiation. Considering cooling and heating effects will allow us to study feedback from protostars that could limit the accretion time scale, possibly leading to lower protostar masses. This could affect the MMO since gas accretion would play a minor role, as shown in [Schleicher et al. \(2022\)](#). Cooling caused by molecular hydrogen could impact the gas inflow due to fragmentation, strongly affecting the accretion rates and therefore the final mass of the MMO. Furthermore, the cooling by heavier metals together with early fragmentation can prevent the formation of an MMO, because the cluster does not become compact enough. Finally, the analyzed scenario can be strongly influenced by the metallicity of the gas, which influences the cooling, fragmentation, feedback, dynamic effects of the gas and even the initial mass function of the resulting protostars.

From the results of the simulations we observe that the change in temperature does not present a change in the possibility of the cluster in creating an MMO, since for all temperatures an MMO is always formed in practically the same way and reaching the same mass percentages in similar times. The difference in the evolution of the MMO occurs in the second half of its evolution, where as a result

of the lower densities the gas collapses faster for lower temperatures, potentially producing a more massive MMO, due to higher accretion rates. On the other hand, for the simulations with higher temperatures, a central density is quickly reached, controlling the accretion of the MMO and prolonging it for a longer time. This maintains an inflated radius of the MMO for longer time, allowing for more collisions to happen.

As we have already mentioned in this work we have not yet robustly implemented cooling or heating processes, but our results agree with those found by [Chon and Omukai \(2020\)](#) in the super competitive accretion scenario, where only a few central stars grow into supermassive stars while the other protostars compete for the gas reservoir. They explored similar scenarios including tabulated density-temperature values pre-calculated with one-zone models and our results agree with their low metallicity cases ($< 10^{-4} Z_{\odot}$), where they obtain binary systems of masses of $\sim 10^4 M_{\odot}$ in 10^4 yr, obtaining an efficiency of $\sim 90 - 100\%$ but in the same way as in our simulations approximately the total gas mass was accreted. In comparison in our simulations and according to similar efficiencies obtained by [Reinoso et al.](#), in preparation, for a time of 10^4 yr we obtain masses of the MMOs of $\sim 2.2 - 2.4 \times 10^4 M_{\odot}$ for the simulations from higher to lower temperatures, reaching an efficiency of $\sim 70\%$ of MMO for simulationes with $M_{\text{gas}}/M_{\text{Jeans}} \approx 5.3$ and an efficiency of $\sim 80\%$ for simulationes with $M_{\text{gas}}/M_{\text{Jeans}} \approx 340$. As we know from previous works ([Das et al., 2021b](#); [Schleicher et al., 2022](#); [Chon and Omukai, 2020](#)) the efficiency of MMO formation is highly sensitive to the initial conditions, but another interesting related parameter is the initial instability of the gas, where together with the results obtained by [Solar et al. \(2022\)](#) simulations suggest that the instability of the gas directly affects the efficiency of MMO formation, being apparently faster for more unstable systems. With these unstable conditions and accretionary scenarios, the system is more susceptible to the creation of massive MMOs and with high efficiency, as obtained by [Sassano et al. \(2021\)](#). Even considering higher metallicities, the results considering effects of super-competitive accretion are more likely to produce more massive BHs. On the other hand, initial conditions such as metallicity, background radiation, etc. directly impact the SMBH seed formation scenario, as well as affect the mass function of supermassive black holes, as shown in [Sassano et al. \(2021\)](#), so to elucidate questions about the formation of the first galaxies and BHs in them future observations of the early

Universe from the JWST in the near-infrared will be very important.



Bibliography

- Aarseth, S. J. (1985). 12 - direct methods for n-body simulations. In BRACKBILL, J. U. and COHEN, B. I., editors, *Multiple Time Scales*, pages 377–418. Academic Press.
- Abel, T., Bryan, G. L., and Norman, M. L. (2000). The formation and fragmentation of primordial molecular clouds. *The Astrophysical Journal*, 540(1):39–44.
- Agarwal, B. and Khochfar, S. (2014). Revised rate coefficients for H₂ and H destruction by realistic stellar spectra. *Monthly Notices of the Royal Astronomical Society*, 446(1):160–168.
- Alister Seguel, P. J., Schleicher, D. R. G., Boekholt, T. C. N., Fellhauer, M., and Klessen, R. S. (2020). Formation of SMBH seeds in Population III star clusters through collisions: the importance of mass loss. , 493(2):2352–2362.
- Ambrosiano, J., Greengard, L., and Rokhlin, V. (1988). The fast multipole method for gridless particle simulation. *Computer Physics Communications*, 48(1):117–125.
- Bañados, E., Venemans, B. P., Decarli, R., Farina, E. P., Mazzucchelli, C., Walter, F., Fan, X., Stern, D., Schlafly, E., Chambers, K. C., Rix, H. W., Jiang, L., McGreer, I., Simcoe, R., Wang, F., Yang, J., Morganson, E., De Rosa, G., Greiner, J., Baloković, M., Burgett, W. S., Cooper, T., Draper, P. W., Flewelling, H., Hodapp, K. W., Jun, H. D., Kaiser, N., Kudritzki, R. P., Magnier, E. A., Metcalfe, N., Miller, D., Schindler, J. T., Tonry, J. L., Wainscoat, R. J., Waters, C., and Yang, Q. (2016). The Pan-STARRS1 Distant $z > 5.6$ Quasar Survey: More than 100 Quasars within the First Gyr of the Universe. , 227(1):11.
- Bañados, E., Venemans, B. P., Mazzucchelli, C., Farina, E. P., Walter, F., Wang, F., Decarli, R., Stern, D., Fan, X., Davies, F. B., Hennawi, J. F., Simcoe, R. A., Turner, M. L., Rix, H.-W., Yang, J., Kelson, D. D., Rudie, G. C., and Winters, J. M. (2018). An 800-million-solar-mass black hole in a significantly neutral Universe at a redshift of 7.5. , 553(7689):473–476.
- Barnes, J. and Hut, P. (1986a). A hierarchical $O(N \log N)$ force-calculation algorithm. , 324(6096):446–449.

- Barnes, J. and Hut, P. (1986b). A hierarchical $O(N \log N)$ force-calculation algorithm. , 324(6096):446–449.
- Bate, M. R., Bonnell, I. A., and Price, N. M. (1995). Modelling accretion in protobinary systems. , 277(2):362–376.
- Baumgardt, H. and Klessen, R. S. (2011). The role of stellar collisions for the formation of massive stars. , 413(3):1810–1818.
- Becerra, F., Greif, T. H., Springel, V., and Hernquist, L. E. (2015). Formation of massive protostars in atomic cooling haloes. , 446(3):2380–2393.
- Becerra, F., Marinacci, F., Inayoshi, K., Bromm, V., and Hernquist, L. E. (2018). Opacity Limit for Supermassive Protostars. , 857(2):138.
- Boekholt, T. and Portegies Zwart, S. (2015). On the reliability of N-body simulations. *Computational Astrophysics and Cosmology*, 2:2.
- Boekholt, T. C. N., Schleicher, D. R. G., Fellhauer, M., Klessen, R. S., Reinoso, B., Stutz, A. M., and Haemmerlé, L. (2018). Formation of massive seed black holes via collisions and accretion. , 476(1):366–380.
- Bonnell, I. A., Bate, M. R., and Zinnecker, H. (1998). On the formation of massive stars. , 298(1):93–102.
- Bottema, R. (2003). Simulations of normal spiral galaxies. , 344(2):358–384.
- Bovino, S., Grassi, T., Schleicher, D. R. G., and Latif, M. A. (2014). Formation of Carbon-enhanced Metal-poor Stars in the Presence of Far-ultraviolet Radiation. , 790(2):L35.
- Bowman, J. D., Rogers, A. E. E., Monsalve, R. A., Mozdzen, T. J., and Mahesh, N. (2018). An absorption profile centred at 78 megahertz in the sky-averaged spectrum. , 555(7694):67–70.
- Breeden, J. L., Cohn, H. N., and Hut, P. (1994). The Onset of Gravo-thermal Oscillations in Globular Cluster Evolution. , 421:195.
- Bromm, V., Coppi, P. S., and Larson, R. B. (1999). Forming the first stars in the universe: The fragmentation of primordial gas. *The Astrophysical Journal*, 527(1):L5–L8.
- Bromm, V., Coppi, P. S., and Larson, R. B. (2002). The formation of the first stars. i. the primordial star-forming cloud. *The Astrophysical Journal*, 564(1):23–51.
- Bromm, V. and Loeb, A. (2003). Formation of the First Supermassive Black Holes. , 596(1):34–46.
- Bromm, V., Yoshida, N., Hernquist, L., and McKee, C. F. (2009). The formation of the first stars and galaxies. , 459(7243):49–54.
- Carr, B. J., Bond, J. R., and Arnett, W. D. (1984). Cosmological consequences of Population III stars. , 277:445–469.

- Chandrasekhar, S. (1964). The Dynamical Instability of Gaseous Masses Approaching the Schwarzschild Limit in General Relativity. , 140:417.
- Chon, S. and Omukai, K. (2020). Supermassive star formation via super competitive accretion in slightly metal-enriched clouds. , 494(2):2851–2860.
- Ciardi, B., Ferrara, A., and Abel, T. (2000). Intergalactic H₂ Photodissociation and the Soft Ultraviolet Background Produced by Population III Objects. , 533(2):594–600.
- Clark, P. C., Glover, S. C. O., and Klessen, R. S. (2008). The First Stellar Cluster. , 672(2):757–764.
- Clarke, C. J. and Bonnell, I. A. (2008). Accretion-driven core collapse and the collisional formation of massive stars. , 388(3):1171–1174.
- Cohn, H. (1979). Numerical integration of the Fokker-Planck equation and the evolution of star clusters. , 234:1036–1053.
- Collaboration, T. E. H. T. (2022). First sagittarius a* event horizon telescope results. i. the shadow of the supermassive black hole in the center of the milky way. *The Astrophysical Journal Letters*, 930(L12).
- D’Amico, G., Panci, P., Lupi, A., Bovino, S., and Silk, J. (2018). Massive black holes from dissipative dark matter. , 473(1):328–335.
- Das, A., Schleicher, D. R. G., Basu, S., and Boekholt, T. C. N. (2021a). Effect of mass-loss due to stellar winds on the formation of supermassive black hole seeds in dense nuclear star clusters. , 505(2):2186–2194.
- Das, A., Schleicher, D. R. G., Leigh, N. W. C., and Boekholt, T. C. N. (2021b). Formation of supermassive black hole seeds in nuclear star clusters via gas accretion and runaway collisions. , 503(1):1051–1069.
- Davies, M. B., Miller, M. C., and Bellovary, J. M. (2011). Supermassive Black Hole Formation Via Gas Accretion in Nuclear Stellar Clusters. , 740(2):L42.
- Dehnen, W. (2001). Towards optimal softening in three-dimensional N-body codes - I. Minimizing the force error. , 324(2):273–291.
- Dehnen, W. (2014). A fast multipole method for stellar dynamics. *Computational Astrophysics and Cosmology*, 1:1.
- Devecchi, B. and Volonteri, M. (2009). FORMATION OF THE FIRST NUCLEAR CLUSTERS AND MASSIVE BLACK HOLES AT HIGH REDSHIFT. *The Astrophysical Journal*, 694(1):302–313.
- Dijkstra, M., Ferrara, A., and Mesinger, A. (2014). Feedback-regulated supermassive black hole seed formation. , 442(3):2036–2047.
- Dijkstra, M., Haiman, Z., Mesinger, A., and Wyithe, J. S. B. (2008). Fluctuations in the high-redshift Lyman–Werner background: close halo pairs as the origin

- of supermassive black holes. *Monthly Notices of the Royal Astronomical Society*, 391(4):1961–1972.
- Duckworth, H., Sharp, D. J., and Ghajari, M. (2021). Smoothed particle hydrodynamic modelling of the cerebrospinal fluid for brain biomechanics: Accuracy and stability. *International Journal for Numerical Methods in Biomedical Engineering*, 37(4):e3440.
- Duquennoy, A. and Mayor, M. (1991). Multiplicity among Solar Type Stars in the Solar Neighbourhood - Part Two - Distribution of the Orbital Elements in an Unbiased Sample. , 248:485.
- Elvis, M., Risaliti, G., and Zamorani, G. (2002). Most Supermassive Black Holes Must Be Rapidly Rotating. , 565(2):L75–L77.
- Escala, A. (2021). Observational Support for Massive Black Hole Formation Driven by Runaway Stellar Collisions in Galactic Nuclei. , 908(1):57.
- Espinoza, P., Selman, F. J., and Melnick, J. (2009). The massive star initial mass function of the Arches cluster. , 501(2):563–583.
- Event Horizon Telescope Collaboration, Akiyama, K., Alberdi, A., Alef, W., Asada, K., Azulay, R., Baczko, A.-K., Ball, D., Baloković, M., Barrett, J., Bintley, D., Blackburn, L., Boland, W., Bouman, K. L., Bower, G. C., Bremer, M., Brinkerink, C. D., Brissenden, R., Britzen, S., Broderick, A. E., Brogiere, D., Bronzwaer, T., Byun, D.-Y., Carlstrom, J. E., Chael, A., Chan, C.-k., Chatterjee, S., Chatterjee, K., Chen, M.-T., Chen, Y., Cho, I., Christian, P., Conway, J. E., Cordes, J. M., Crew, G. B., Cui, Y., Davelaar, J., De Laurentis, M., Deane, R., Dempsey, J., Desvignes, G., Dexter, J., Doleman, S. S., Eatough, R. P., Falcke, H., Fish, V. L., Fomalont, E., Fraga-Encinas, R., Freeman, W. T., Friberg, P., Fromm, C. M., Gómez, J. L., Galison, P., Gammie, C. F., García, R., Gentaz, O., Georgiev, B., Goddi, C., Gold, R., Gu, M., Gurwell, M., Hada, K., Hecht, M. H., Hesper, R., Ho, L. C., Ho, P., Honma, M., Huang, C.-W. L., Huang, L., Hughes, D. H., Ikeda, S., Inoue, M., Issaoun, S., James, D. J., Jannuzi, B. T., Janssen, M., Jeter, B., Jiang, W., Johnson, M. D., Jorstad, S., Jung, T., Karami, M., Karuppusamy, R., Kawashima, T., Keating, G. K., Kettenis, M., Kim, J.-Y., Kim, J., Kim, J., Kino, M., Koay, J. Y., Koch, P. M., Koyama, S., Kramer, M., Kramer, C., Krichbaum, T. P., Kuo, C.-Y., Lauer, T. R., Lee, S.-S., Li, Y.-R., Li, Z., Lindqvist, M., Liu, K., Liuzzo, E., Lo, W.-P., Lobanov, A. P., Loinard, L., Lonsdale, C., Lu, R.-S., MacDonald, N. R., Mao, J., Markoff, S., Marrone, D. P., Marscher, A. P., Martí-Vidal, I., Matsushita, S., Matthews, L. D., Medeiros, L., Menten, K. M., Mizuno, Y., Mizuno, I., Moran, J. M., Moriyama, K., Moscibrodzka, M., Müller, C., Nagai, H., Nagar, N. M., Nakamura, M., Narayan, R., Narayanan, G., Natarajan, I., Neri, R., Ni, C., Noutsos, A., Okino, H., Olivares, H., Ortiz-León, G. N., Oyama, T., Özel, F., Palumbo, D. C. M., Patel, N., Pen, U.-L., Pesce, D. W., Piétu, V., Plambeck, R., PopStefanija, A., Porth, O., Prather, B., Preciado-López, J. A., Psaltis, D., Pu, H.-Y., Ramakrishnan, V., Rao, R., Rawlings, M. G.,

- Raymond, A. W., Rezzolla, L., Ripperda, B., Roelofs, F., Rogers, A., Ros, E., Rose, M., Roshanineshat, A., Rottmann, H., Roy, A. L., Ruszczyk, C., Ryan, B. R., Rygl, K. L. J., Sánchez, S., Sánchez-Arguelles, D., Sasada, M., Savolainen, T., Schloerb, F. P., Schuster, K.-F., Shao, L., Shen, Z., Small, D., Sohn, B. W., SooHoo, J., Tazaki, F., Tiede, P., Tilanus, R. P. J., Titus, M., Toma, K., Torne, P., Trent, T., Trippe, S., Tsuda, S., van Bemmell, I., van Langevelde, H. J., van Rossum, D. R., Wagner, J., Wardle, J., Weintroub, J., Wex, N., Wharton, R., Wielgus, M., Wong, G. N., Wu, Q., Young, K., Young, A., Younsi, Z., Yuan, F., Yuan, Y.-F., Zensus, J. A., Zhao, G., Zhao, S.-S., Zhu, Z., Algaba, J.-C., Allardi, A., Amestica, R., Anczarski, J., Bach, U., Baganoff, F. K., Beaudoin, C., Benson, B. A., Berthold, R., Blanchard, J. M., Blundell, R., Bustamente, S., Cappallo, R., Castillo-Domínguez, E., Chang, C.-C., Chang, S.-H., Chang, S.-C., Chen, C.-C., Chilson, R., Chuter, T. C., Córdova Rosado, R., Coulson, I. M., Crawford, T. M., Crowley, J., David, J., Derome, M., Dexter, M., Dornbusch, S., Dudevoir, K. A., Dzib, S. A., Eckart, A., Eckert, C., Erickson, N. R., Everett, W. B., Faber, A., Farah, J. R., Fath, V., Folkers, T. W., Forbes, D. C., Freund, R., Gómez-Ruiz, A. I., Gale, D. M., Gao, F., Geertsema, G., Graham, D. A., Greer, C. H., Grosslein, R., Gueth, F., Haggard, D., Halverson, N. W., Han, C.-C., Han, K.-C., Hao, J., Hasegawa, Y., Henning, J. W., Hernández-Gómez, A., Herrero-Illana, R., Heyminck, S., Hirota, A., Hoge, J., Huang, Y.-D., Impellizzeri, C. M. V., Jiang, H., Kamble, A., Keisler, R., Kimura, K., Kono, Y., Kubo, D., Kuroda, J., Lacasse, R., Laing, R. A., Leitch, E. M., Li, C.-T., Lin, L. C. C., Liu, C.-T., Liu, K.-Y., Lu, L.-M., Marson, R. G., Martin-Cocher, P. L., Massingill, K. D., Matulonis, C., McColl, M. P., McWhirter, S. R., Messias, H., Meyer-Zhao, Z., Michalik, D., Montaña, A., Montgomerie, W., Mora-Klein, M., Muders, D., Nadolski, A., Navarro, S., Neilsen, J., Nguyen, C. H., Nishioka, H., Norton, T., Nowak, M. A., Nystrom, G., Ogawa, H., Oshiro, P., Oyama, T., Parsons, H., Paine, S. N., Peñalver, J., Phillips, N. M., Poirier, M., Pradel, N., Primiani, R. A., Raffin, P. A., Rahlin, A. S., Reiland, G., Risacher, C., Ruiz, I., Sáez-Madaín, A. F., Sassella, R., Schellart, P., Shaw, P., Silva, K. M., Shiokawa, H., Smith, D. R., Snow, W., Souccar, K., Sousa, D., Sridharan, T. K., Srinivasan, R., Stahm, W., Stark, A. A., Story, K., Timmer, S. T., Vertatschitsch, L., Walther, C., Wei, T.-S., Whitehorn, N., Whitney, A. R., Woody, D. P., Wouterloot, J. G. A., Wright, M., Yamaguchi, P., Yu, C.-Y., Zaballos, M., Zhang, S., and Ziurys, L. (2019). First M87 Event Horizon Telescope Results. I. The Shadow of the Supermassive Black Hole. , 875(1):L1.
- Fan, X., Narayanan, V. K., Lupton, R. H., Strauss, M. A., Knapp, G. R., Becker, R. H., White, R. L., Pentericci, L., Leggett, S. K., Haiman, Z., Gunn, J. E., Ivezić, Ž., Schneider, D. P., Anderson, S. F., Brinkmann, J., Bahcall, N. A., Connolly, A. J., Csabai, I., Doi, M., Fukugita, M., Geballe, T., Grebel, E. K., Harbeck, D., Hennessy, G., Lamb, D. Q., Miknaitis, G., Munn, J. A., Nichol, R., Okamura, S., Pier, J. R., Prada, F., Richards, G. T., Szalay, A., and York, D. G. (2001). A Survey of $z > 5.8$ Quasars in the Sloan Digital Sky Survey. I. Discovery of Three New Quasars and the Spatial Density of Luminous Quasars

- at $z \sim 6$. , 122(6):2833–2849.
- Federrath, C., Banerjee, R., Clark, P. C., and Klessen, R. S. (2010). Modeling Collapse and Accretion in Turbulent Gas Clouds: Implementation and Comparison of Sink Particles in AMR and SPH. , 713(1):269–290.
- Fernandez, R., Bryan, G. L., Haiman, Z., and Li, M. (2014). H₂ suppression with shocking inflows: testing a pathway for supermassive black hole formation. *Monthly Notices of the Royal Astronomical Society*, 439(4):3798–3807.
- Ferrara, A., Salvadori, S., Yue, B., and Schleicher, D. (2014). Initial mass function of intermediate-mass black hole seeds. *Monthly Notices of the Royal Astronomical Society*, 443(3):2410–2425.
- Forgan, D., Rice, K., Cossins, P., and Lodato, G. (2011). The nature of angular momentum transport in radiative self-gravitating protostellar discs. , 410(2):994–1006.
- Fujii, M., Iwasawa, M., Funato, Y., and Makino, J. (2007). BRIDGE: A Direct-Tree Hybrid N-Body Algorithm for Fully Self-Consistent Simulations of Star Clusters and Their Parent Galaxies. , 59:1095.
- Fujii, M. S. and Portegies Zwart, S. (2013). The growth of massive stars via stellar collisions in ensemble star clusters. , 430(2):1018–1029.
- Gao, L., Yoshida, N., Abel, T., Frenk, C. S., Jenkins, A., and Springel, V. (2007). The first generation of stars in the Λ cold dark matter cosmology. , 378(2):449–468.
- Gerritsen, J. (1997). *Star formation and the interstellar medium in galaxy simulations*. PhD thesis. date_{submitted} : 1997 Rights : *University of Groningen*.
- Gerritsen, J. P. E. and Icke, V. (1997). Star formation in N-body simulations. I. The impact of the stellar ultraviolet radiation on star formation. , 325:972–986.
- Ghez, A. M., Salim, S., Weinberg, N. N., Lu, J. R., Do, T., Dunn, J. K., Matthews, K., Morris, M. R., Yelda, S., Becklin, E. E., Kremenek, T., Milosavljevic, M., and Naiman, J. (2008). Measuring Distance and Properties of the Milky Way’s Central Supermassive Black Hole with Stellar Orbits. , 689(2):1044–1062.
- Ghisellini, G., Della Ceca, R., Volonteri, M., Ghirlanda, G., Tavecchio, F., Foschini, L., Tagliaferri, G., Haardt, F., Pareschi, G., and Grindlay, J. (2010). Chasing the heaviest black holes of jetted active galactic nuclei. , 405(1):387–400.
- Gingold, R. A. and Monaghan, J. J. (1977). Smoothed particle hydrodynamics: theory and application to non-spherical stars. *Monthly Notices of the Royal Astronomical Society*, 181(3):375–389.
- Godunov, S. K. and Bohachevsky, I. (1959). Finite difference method for numerical computation of discontinuous solutions of the equations of fluid dynamics. *Matematičeskij sbornik*, 47(89)(3):271–306.

- Grassi, T., Bovino, S., Haugbølle, T., and Schleicher, D. R. G. (2017). A detailed framework to incorporate dust in hydrodynamical simulations. , 466(2):1259–1274.
- Grete, P., Latif, M. A., Schleicher, D. R. G., and Schmidt, W. (2019). Intermittent fragmentation and statistical variations during gas collapse in magnetized atomic cooling haloes. , 487(4):4525–4535.
- Gropp, W., Lusk, E., Doss, N., and Skjellum, A. (1996). A high-performance, portable implementation of the mpi message passing interface standard. *Parallel Computing*, 22(6):789–828.
- Haemmerlé, L. (2020). General-relativistic instability in hylotropic supermassive stars. , 644:A154.
- Haemmerlé, L. (2021). General-relativistic instability in rapidly accreting supermassive stars: The impact of rotation. , 650:A204.
- Haemmerlé, L., Woods, T. E., Klessen, R. S., Heger, A., and Whalen, D. J. (2018). The evolution of supermassive Population III stars. , 474(2):2757–2773.
- Haiman, Z. (2004). Constraints from Gravitational Recoil on the Growth of Supermassive Black Holes at High Redshift. , 613(1):36–40.
- Haiman, Z., Abel, T., and Rees, M. J. (2000). The radiative feedback of the first cosmological objects. *The Astrophysical Journal*, 534(1):11–24.
- Haiman, Z., Rees, M. J., and Loeb, A. (1997). Destruction of molecular hydrogen during cosmological reionization. *The Astrophysical Journal*, 476(2):458–463.
- Hartmann, L. (1998). *Accretion Processes in Star Formation*.
- Heger, A., Fryer, C. L., Woosley, S. E., Langer, N., and Hartmann, D. H. (2003). How massive single stars end their life. *The Astrophysical Journal*, 591(1):288–300.
- Hernquist, L. and Katz, N. (1989a). TREESPH: A Unification of SPH with the Hierarchical Tree Method. , 70:419.
- Hernquist, L. and Katz, N. (1989b). TREESPH: A Unification of SPH with the Hierarchical Tree Method. , 70:419.
- Hirano, S., Hosokawa, T., Yoshida, N., Omukai, K., and Yorke, H. W. (2015). Primordial star formation under the influence of far ultraviolet radiation: 1540 cosmological haloes and the stellar mass distribution. , 448(1):568–587.
- Hirano, S., Hosokawa, T., Yoshida, N., Umeda, H., Omukai, K., Chiaki, G., and Yorke, H. W. (2014). iONE HUNDRED FIRST STARS/i: PROTOSTELLAR EVOLUTION AND THE FINAL MASSES. *The Astrophysical Journal*, 781(2):60.
- Hirasawa, T. (1969). Formation of Protogalaxies and Molecular Processes in Hydrogen Gas. *Progress of Theoretical Physics*, 42(3):523–543.
- Hosokawa, T. and Omukai, K. (2009). Low-Metallicity Protostars and the

- Maximum Stellar Mass Resulting from Radiative Feedback: Spherically Symmetric Calculations. , 703(2):1810–1818.
- Hosokawa, T., Omukai, K., and Yorke, H. W. (2012). Rapidly Accreting Supergiant Protostars: Embryos of Supermassive Black Holes? , 756(1):93.
- Hosokawa, T., Omukai, K., Yoshida, N., and Yorke, H. W. (2011). Protostellar feedback halts the growth of the first stars in the universe. *Science*, 334(6060):1250–1253.
- Hosokawa, T., Yorke, H. W., Inayoshi, K., Omukai, K., and Yoshida, N. (2013). Formation of Primordial Supermassive Stars by Rapid Mass Accretion. , 778(2):178.
- Hubber, D. A., Walch, S., and Whitworth, A. P. (2013). An improved sink particle algorithm for sph simulations. *Monthly Notices of the Royal Astronomical Society*, 430(4):3261–3275.
- Hut, P., Makino, J., and McMillan, S. (1995). Building a Better Leapfrog. , 443:L93.
- Inayoshi, K. and Omukai, K. (2012). Supermassive black hole formation by cold accretion shocks in the first galaxies. , 422(3):2539–2546.
- Inayoshi, K., Visbal, E., and Haiman, Z. (2020). The assembly of the first massive black holes. *Annual Review of Astronomy and Astrophysics*, 58(1):27–97.
- Inayoshi, K., Visbal, E., and Kashiyama, K. (2015). Direct collapse black hole formation via high-velocity collisions of protogalaxies. , 453(2):1692–1700.
- J. P. Gardner, J. C. Mather, M. Clampin, R. Doyon, M. A. Greenhouse, H. B. Hammel, J. B. Hutchings, P. Jakobsen, S. J. Lilly, K. S. Long, J. I. Lunine, M. J. Mccaughrean, M. Mountain, J. Nella, G. H. Rieke, M. J. Rieke, H.-W. Rix, E. P. Smith, G. Sonneborn, M. Stiavelli, H. S. Stockman, R. A. Windhorst, and G. S. Wright (2006). “the james webb space telescope,” space science reviews. *Space Sci Rev*, 123:485–606.
- Janka, H.-T. (2002). Supermassive Stars: Fact or Fiction? In Gilfanov, M., Sunyeav, R., and Churazov, E., editors, *Lighthouses of the Universe: The Most Luminous Celestial Objects and Their Use for Cosmology*, page 357.
- Jiang, L., McGreer, I. D., Fan, X., Strauss, M. A., Bañados, E., Becker, R. H., Bian, F., Farnsworth, K., Shen, Y., Wang, F., Wang, R., Wang, S., White, R. L., Wu, J., Wu, X.-B., Yang, J., and Yang, Q. (2016). THE FINAL SDSS HIGH-REDSHIFT QUASAR SAMPLE OF 52 QUASARS ATz 5.7. *The Astrophysical Journal*, 833(2):222.
- Johnson, J. L., Dalla, V. C., and Khochfar, S. (2012). The First Billion Years project: the impact of stellar radiation on the co-evolution of Populations II and III. *Monthly Notices of the Royal Astronomical Society*, 428(3):1857–1872.
- Katz, H., Sijacki, D., and Haehnelt, M. G. (2015). Seeding high-redshift QSOs by collisional runaway in primordial star clusters. , 451(3):2352–2369.

- Latif, M. A., Bovino, S., Grassi, T., Schleicher, D. R. G., and Spaans, M. (2015). How realistic UV spectra and X-rays suppress the abundance of direct collapse black holes. , 446(3):3163–3177.
- Latif, M. A., Khochfar, S., Schleicher, D., and Whalen, D. J. (2021). Radiation hydrodynamical simulations of the birth of intermediate-mass black holes in the first galaxies. , 508(2):1756–1767.
- Latif, M. A., Schleicher, D. R. G., Bovino, S., Grassi, T., and Spaans, M. (2014). THE FORMATION OF MASSIVE PRIMORDIAL STARS IN THE PRESENCE OF MODERATE UV BACKGROUNDS. *The Astrophysical Journal*, 792(1):78.
- Latif, M. A., Schleicher, D. R. G., Schmidt, W., and Niemeyer, J. (2013). Black hole formation in the early Universe. *Monthly Notices of the Royal Astronomical Society*, 433(2):1607–1618.
- Lucy, L. B. (1977). A numerical approach to the testing of the fission hypothesis. , 82:1013–1024.
- Lynden-Bell, D. and Wood, R. (1968). The gravo-thermal catastrophe in isothermal spheres and the onset of red-giant structure for stellar systems. , 138:495.
- Maassen, J. and Bal, H. (2007). *Smartsockets*: solving the connectivity problems in grid computing. pages 1–10. 1272368.
- Machacek, M. E., Bryan, G. L., and Abel, T. (2001). Simulations of Pregalactic Structure Formation with Radiative Feedback. , 548(2):509–521.
- Makino, J. and Aarseth, S. J. (1992). On a Hermite Integrator with Ahmad-Cohen Scheme for Gravitational Many-Body Problems. , 44:141–151.
- Matsuda, T., Satō, H., and Takeda, H. (1969). Cooling of Pre-Galactic Gas Clouds by Hydrogen Molecule. *Progress of Theoretical Physics*, 42(2):219–233.
- Matsuoka, Y., Onoue, M., Kashikawa, N., Iwasawa, K., Strauss, M. A., Nagao, T., Imanishi, M., Lee, C.-H., Akiyama, M., Asami, N., Bosch, J., Foucaud, S., Furusawa, H., Goto, T., Gunn, J. E., Harikane, Y., Ikeda, H., Izumi, T., Kawaguchi, T., Kikuta, S., Kohno, K., Komiyama, Y., Lupton, R. H., Minezaki, T., Miyazaki, S., Morokuma, T., Murayama, H., Niida, M., Nishizawa, A. J., Oguri, M., Ono, Y., Ouchi, M., Price, P. A., Sameshima, H., Schulze, A., Shirakata, H., Silverman, J. D., Sugiyama, N., Tait, P. J., Takada, M., Takata, T., Tanaka, M., Tang, J.-J., Toba, Y., Utsumi, Y., and Wang, S.-Y. (2018). Subaru High- z Exploration of Low-Luminosity Quasars (SHELLQs). II. Discovery of 32 quasars and luminous galaxies at $5.7 < z \leq 6.8$. , 70:S35.
- Mayer, L., Fiacconi, D., Bonoli, S., Quinn, T., Roškar, R., Shen, S., and Wadsley, J. (2015). DIRECT FORMATION OF SUPERMASSIVE BLACK HOLES IN METAL-ENRICHED GAS AT THE HEART OF HIGH-REDSHIFT GALAXY MERGERS. *The Astrophysical Journal*, 810(1):51.
- Mayer, L., Kazantzidis, S., Escala, A., and Callegari, S. (2010). Direct formation of

- supermassive black holes via multi-scale gas inflows in galaxy mergers. *Nature*, 466(7310):1082–1084.
- Mazzucchelli, C., Bañados, E., Decarli, R., Farina, E. P., Venemans, B. P., Walter, F., and Overzier, R. (2017). No Overdensity of Lyman-Alpha Emitting Galaxies around a Quasar at $z \sim 5.7$. , 834(1):83.
- McConnell, N. J., Ma, C.-P., Gebhardt, K., Wright, S. A., Murphy, J. D., Lauer, T. R., Graham, J. R., and Richstone, D. O. (2011). Two ten-billion-solar-mass black holes at the centres of giant elliptical galaxies. , 480(7376):215–218.
- McKee, C. F. and Tan, J. C. (2008). The Formation of the First Stars. II. Radiative Feedback Processes and Implications for the Initial Mass Function. , 681(2):771–797.
- Mesinger, A., Bryan, G. L., and Haiman, Z. (2006). Ultraviolet radiative feedback on high-redshift protogalaxies. *The Astrophysical Journal*, 648(2):835–851.
- Miyamoto, M. and Nagai, R. (1975). Three-dimensional models for the distribution of mass in galaxies. , 27:533–543.
- Moeckel, N. and Clarke, C. J. (2011). Collisional formation of very massive stars in dense clusters. , 410(4):2799–2806.
- Monaghan, J. J. and Lattanzio, J. C. (1985). A refined particle method for astrophysical problems. , 149(1):135–143.
- Newton, I. (1687). *Philosophiae Naturalis Principia Mathematica. Auctore Js. Newton.*
- Oh, S. and Kroupa, P. (2012). The influence of stellar dynamical ejections and collisions on the relation between the maximum stellar and star cluster mass. , 424(1):65–79.
- Oh, S. P. and Haiman, Z. (2002). Second-generation objects in the universe: Radiative cooling and collapse of halos with virial temperatures above 10^4 K. *The Astrophysical Journal*, 569(2):558–572.
- Omukai, K. (2001). Primordial star formation under far-ultraviolet radiation. *The Astrophysical Journal*, 546(2):635–651.
- Omukai, K. and Nishi, R. (1999). Photodissociative regulation of star formation in metal-free pregalactic clouds. *The Astrophysical Journal*, 518(1):64–68.
- Omukai, K., Schneider, R., and Haiman, Z. (2008). Can Supermassive Black Holes Form in Metal-enriched High-Redshift Protogalaxies? , 686(2):801–814.
- Omukai, K., Tsuribe, T., Schneider, R., and Ferrara, A. (2005). Thermal and Fragmentation Properties of Star-forming Clouds in Low-Metallicity Environments. , 626(2):627–643.
- Onoue, M., Kashikawa, N., Matsuoka, Y., Kato, N., Izumi, T., Nagao, T., Strauss, M. A., Harikane, Y., Imanishi, M., Ito, K., Iwasawa, K., Kawaguchi, T., Lee,

- C.-H., Noboriguchi, A., Suh, H., Tanaka, M., and Toba, Y. (2019). Subaru High- z Exploration of Low-luminosity Quasars (SHELLQs). VI. Black Hole Mass Measurements of Six Quasars at $6.1 \leq z \leq 6.7$. , 880(2):77.
- O'Shea, B. W. and Norman, M. L. (2008). Population III Star Formation in a Λ CDM Universe. II. Effects of a Photodissociating Background. , 673(1):14–33.
- Pacucci, F., Natarajan, P., and Ferrara, A. (2017). Feedback limits to maximum seed masses of black holes. *The Astrophysical Journal*, 835(2):L36.
- Peebles, P. J. E. and Dicke, R. H. (1968). Origin of the Globular Star Clusters. , 154:891.
- Pelupessy, F. I., van der Werf, P. P., and Icke, V. (2004). Periodic bursts of star formation in irregular galaxies. , 422:55–64.
- Pelupessy, F. I., van Elteren, A., de Vries, N., McMillan, S. L. W., Drost, N., and Portegies Zwart, S. F. (2013). The Astrophysical Multipurpose Software Environment. , 557:A84.
- Peters, T., Schleicher, D. R. G., Smith, R. J., Schmidt, W., and Klessen, R. S. (2014). Low-metallicity star formation: relative impact of metals and magnetic fields. , 442(4):3112–3126.
- Plummer, H. C. (1911). On the problem of distribution in globular star clusters. , 71:460–470.
- Portegies Zwart, S. and McMillan, S. (2018). *Astrophysical Recipes*. 2514-3433. IOP Publishing.
- Portegies Zwart, S., McMillan, S., Harfst, S., Groen, D., Fujii, M., Nualláin, B. Ó., Glebbeek, E., Heggie, D., Lombardi, J., Hut, P., Angelou, V., Banerjee, S., Belkus, H., Fragos, T., Fregeau, J., Gaburov, E., Izzard, R., Jurić, M., Justham, S., Sottoriva, A., Teuben, P., van Bever, J., Yaron, O., and Zemp, M. (2009a). A multiphysics and multiscale software environment for modeling astrophysical systems. , 14(4):369–378.
- Portegies Zwart, S., McMillan, S., Harfst, S., Groen, D., Fujii, M., Nualláin, B. Ó., Glebbeek, E., Heggie, D., Lombardi, J., Hut, P., Angelou, V., Banerjee, S., Belkus, H., Fragos, T., Fregeau, J., Gaburov, E., Izzard, R., Jurić, M., Justham, S., Sottoriva, A., Teuben, P., van Bever, J., Yaron, O., and Zemp, M. (2009b). A multiphysics and multiscale software environment for modeling astrophysical systems. , 14(4):369–378.
- Portegies Zwart, S., McMillan, S., Harfst, S., Groen, D., Fujii, M., Nualláin, B. , Glebbeek, E., Heggie, D., Lombardi, J., Hut, P., and et al. (2009). A multiphysics and multiscale software environment for modeling astrophysical systems. *New Astronomy*, 14(4):369–378.
- Portegies Zwart, S., van Elteren, A., Pelupessy, I., McMillan, S., Rieder, S., de Vries, N., Marosvolgyi, M., Whitehead, A., Wall, J., Drost, N., Jilkova, L., Martinez

- Barbosa, C., van der Helm, E., Beedorf, J., Bos, P., Boekholt, T., van Werkhoven, B., Wijnen, T., Hamers, A., Caputo, D., Ferrari, G., Toonen, S., Gaburov, E., Paardekooper, J.-P., Janes, J., Punzo, D., Kruip, C., and Altay, G. (2018). Amuse: The Astrophysical Multipurpose Software Environment.
- Portegies Zwart, S. F., McMillan, S. L., van Elteren, A., Pelupessy, F. I., and de Vries, N. (2013). Multi-physics simulations using a hierarchical interchangeable software interface. *Computer Physics Communications*, 184(3):456–468.
- Price, D. J. and Monaghan, J. J. (2007). An energy-conserving formalism for adaptive gravitational force softening in smoothed particle hydrodynamics and N-body codes. , 374(4):1347–1358.
- Rasio, F. A. and Lombardi, J. C., J. (1999). Smoothed particle hydrodynamics calculations of stellar interactions. *Journal of Computational and Applied Mathematics*, 109(1):213–230.
- Reed, S. L., McMahan, R. G., Martini, P., Banerji, M., Auger, M., Hewett, P. C., Kuposov, S. E., Gibbons, S. L. J., Gonzalez-Solares, E., Ostrovski, F., Tie, S. S., Abdalla, F. B., Allam, S., Benoit-Lévy, A., Bertin, E., Brooks, D., Buckley-Geer, E., Burke, D. L., Carnero Rosell, A., Carrasco Kind, M., Carretero, J., da Costa, L. N., DePoy, D. L., Desai, S., Diehl, H. T., Doel, P., Evrard, A. E., Finley, D. A., Flaughner, B., Fosalba, P., Frieman, J., García-Bellido, J., Gaztanaga, E., Goldstein, D. A., Gruen, D., Gruendl, R. A., Gutierrez, G., James, D. J., Kuehn, K., Kuropatkin, N., Lahav, O., Lima, M., Maia, M. A. G., Marshall, J. L., Melchior, P., Miller, C. J., Miquel, R., Nord, B., Ogando, R., Plazas, A. A., Romer, A. K., Sanchez, E., Scarpine, V., Schubnell, M., Sevilla-Noarbe, I., Smith, R. C., Sobreira, F., Suchyta, E., Swanson, M. E. C., Tarle, G., Tucker, D. L., Walker, A. R., and Wester, W. (2017). Eight new luminous $z \geq 6$ quasars discovered via SED model fitting of VISTA, WISE and Dark Energy Survey Year 1 observations. , 468(4):4702–4718.
- Rees, M. J. (1984). Black Hole Models for Active Galactic Nuclei. , 22:471–506.
- Regan, J. A., Visbal, E., Wise, J. H., Haiman, Z., Johansson, P. H., and Bryan, G. L. (2017). Rapid formation of massive black holes in close proximity to embryonic protogalaxies. *Nature Astronomy*, 1:0075.
- Reinoso, B., Schleicher, D. R. G., Fellhauer, M., Klessen, R. S., and Boekholt, T. C. N. (2018). Collisions in primordial star clusters. Formation pathway for intermediate mass black holes. , 614:A14.
- Sakurai, Y., Hosokawa, T., Yoshida, N., and Yorke, H. W. (2015). Formation of primordial supermassive stars by burst accretion. , 452(1):755–764.
- Sakurai, Y., Yoshida, N., Fujii, M. S., and Hirano, S. (2017). Formation of intermediate-mass black holes through runaway collisions in the first star clusters. , 472(2):1677–1684.

- Salmon, J. K. and Warren, M. S. (1994). Skeletons from the treecode closet. *Journal of Computational Physics*, 111(1):136–155.
- Sassano, F., Schneider, R., Valiante, R., Inayoshi, K., Chon, S., Omukai, K., Mayer, L., and Capelo, P. R. (2021). Light, medium-weight, or heavy? The nature of the first supermassive black hole seeds. , 506(1):613–632.
- Schleicher, D. R. G., Palla, F., Ferrara, A., Galli, D., and Latif, M. (2013). Massive black hole factories: Supermassive and quasi-star formation in primordial halos. , 558:A59.
- Schleicher, D. R. G., Reinoso, B., Latif, M., Klessen, R. S., Vergara, M. Z. C., Das, A., Alister, P., Díaz, V. B., and Solar, P. A. (2022). Origin of supermassive black holes in massive metal-poor protoclusters. , 512(4):6192–6200.
- Schneider, R. and Omukai, K. (2010). Metals, dust and the cosmic microwave background: fragmentation of high-redshift star-forming clouds. , 402(1):429–435.
- Schneider, R., Omukai, K., Inoue, A. K., and Ferrara, A. (2006). Fragmentation of star-forming clouds enriched with the first dust. , 369(3):1437–1444.
- Schodel, R., Ott, T., Genzel, R., Hofmann, R., Lehnert, M., Eckart, A., Mouawad, N., Alexander, T., Reid, M., Lenzen, R., Hartung, M., Lacombe, F., Rouan, D., Gendron, E., Rousset, G., Lagrange, A., Brandner, W., Ageorges, N., and Lidman, C. (2002). A star in a 15.2-year orbit around the supermassive black hole at the centre of the milky way. *Nature*, 419(6908):3.
- Shakura, N. I. and Sunyaev, R. A. (1973). Black holes in binary systems. Observational appearance. , 24:337–355.
- Shang, C., Bryan, G. L., and Haiman, Z. (2010). Supermassive black hole formation by direct collapse: keeping protogalactic gas H_2 free in dark matter haloes with virial temperatures $T_{vir} > \text{rsim } 10^4$ K. , 402(2):1249–1262.
- Shapiro, S. L. (2005). Spin, accretion, and the cosmological growth of supermassive black holes. *The Astrophysical Journal*, 620(1):59–68.
- Shapiro, S. L. and Teukolsky, S. A. (1983). *Black holes, white dwarfs, and neutron stars : the physics of compact objects*.
- Shen, Y., Wu, J., Jiang, L., Bañados, E., Fan, X., Ho, L. C., Riechers, D. A., Strauss, M. A., Venemans, B., Vestergaard, M., Walter, F., Wang, F., Willott, C., Wu, X.-B., and Yang, J. (2019). Gemini GNIRS Near-infrared Spectroscopy of 50 Quasars at $z \gtrsim 5.7$. , 873(1):35.
- Solar, P. A., Schleicher, D. R. G., Reinoso, B., and Klessen, R. S. (2022). Exploring the formation of supermassive black holes in protostar clusters, incorporating a hydrodynamic treatment. *Boletín de la Asociación Argentina de Astronomía La Plata Argentina*, 63:277–279.
- Soltan, A. (1982). Masses of quasars. , 200:115–122.

- Spitzer, L. (1987). *Dynamical evolution of globular clusters*.
- Springel, V. and Hernquist, L. (2002). Cosmological smoothed particle hydrodynamics simulations: the entropy equation. , 333(3):649–664.
- Springel, V., Yoshida, N., and White, S. D. M. (2001). GADGET: a code for collisionless and gasdynamical cosmological simulations. , 6(2):79–117.
- Suazo, M., Prieto, J., Escala, A., and Schleicher, D. R. G. (2019). The Role of Gas Fragmentation During the Formation of Supermassive Black Holes. , 885(2):127.
- Sugimura, K., Omukai, K., and Inoue, A. K. (2014). The critical radiation intensity for direct collapse black hole formation: dependence on the radiation spectral shape. *Monthly Notices of the Royal Astronomical Society*, 445(1):544–553.
- Ueda, Y., Akiyama, M., Ohta, K., and Miyaji, T. (2003). Cosmological Evolution of the Hard X-Ray Active Galactic Nucleus Luminosity Function and the Origin of the Hard X-Ray Background. , 598(2):886–908.
- Umeda, H., Hosokawa, T., Omukai, K., and Yoshida, N. (2016). THE FINAL FATES OF ACCRETING SUPERMASSIVE STARS. *The Astrophysical Journal*, 830(2):L34.
- Venemans, B. P., Bañados, E., Decarli, R., Farina, E. P., Walter, F., Chambers, K. C., Fan, X., Rix, H.-W., Schlafly, E., McMahon, R. G., Simcoe, R., Stern, D., Burgett, W. S., Draper, P. W., Flewelling, H., Hodapp, K. W., Kaiser, N., Magnier, E. A., Metcalfe, N., Morgan, J. S., Price, P. A., Tonry, J. L., Waters, C., AlSayyad, Y., Banerji, M., Chen, S. S., González-Solares, E. A., Greiner, J., Mazzucchelli, C., McGreer, I., Miller, D. R., Reed, S., and Sullivan, P. W. (2015). THE IDENTIFICATION OF z -DROPOUTS IN PAN-STARRS1: THREE QUASARS AT $6.5 < z < 6.7$. *The Astrophysical Journal*, 801(1):L11.
- Vergara, M. Z. C., Schleicher, D. R. G., Boekholt, T. C. N., Reinoso, B., Fellhauer, M., Klessen, R. S., and Leigh, N. W. C. (2021). Stellar collisions in flattened and rotating Population III star clusters. , 649:A160.
- Vito, F., Brandt, W. N., Bauer, F. E., Calura, F., Gilli, R., Luo, B., Shemmer, O., Vignali, C., Zamorani, G., Brusa, M., Civano, F., Comastri, A., and Nanni, R. (2019). The X-ray properties of $z > 6$ quasars: no evident evolution of accretion physics in the first Gyr of the Universe. , 630:A118.
- Volonteri, M. (2010). Formation of supermassive black holes. , 18(3):279–315.
- Volonteri, M. and Rees, M. J. (2005). Rapid growth of high-redshift black holes. *The Astrophysical Journal*, 633(2):624–629.
- Wiklund, T., Mobasher, B., and Bromm, V. (2012). *The First Galaxies: Theoretical Predictions and Observational Clues*. Astrophysics and Space Science Library. Springer Berlin Heidelberg.
- Willott, C. J., Delorme, P., Reyl e, C., Albert, L., Bergeron, J., Crampton, D., Delfosse, X., Forveille, T., Hutchings, J. B., McLure, R. J., Omont, A., and

- Schade, D. (2010). The Canada-France High-z Quasar Survey: Nine New Quasars and the Luminosity Function at Redshift 6. , 139(3):906–918.
- Wise, J. H. and Abel, T. (2007). Suppression of H_2 /subcooling in the ultraviolet background. *The Astrophysical Journal*, 671(2):1559–1567.
- Wise, J. H., Regan, J. A., O’Shea, B. W., Norman, M. L., Downes, T. P., and Xu, H. (2019). Formation of massive black holes in rapidly growing pre-galactic gas clouds. *Nature*, 566(7742):85–88.
- Wise, J. H., Turk, M. J., and Abel, T. (2008). Resolving the formation of protogalaxies. II. central gravitational collapse. *The Astrophysical Journal*, 682(2):745–757.
- Wolcott-Green, J. and Haiman, Z. (2019). H_2 self-shielding with non-LTE rovibrational populations: implications for cooling in protogalaxies. *Monthly Notices of the Royal Astronomical Society*, 484(2):2467–2473.
- Wolcott-Green, J., Haiman, Z., and Bryan, G. L. (2011). Photodissociation of H_2 in protogalaxies: modelling self-shielding in three-dimensional simulations. *Monthly Notices of the Royal Astronomical Society*, 418(2):838–852.
- Woods, T. E., Heger, A., Whalen, D. J., Haemmerlé, L., and Klessen, R. S. (2017). On the Maximum Mass of Accreting Primordial Supermassive Stars. , 842(1):L6.
- Wu, X.-B., Wang, F., Fan, X., Yi, W., Zuo, W., Bian, F., Jiang, L., McGreer, I. D., Wang, R., Yang, J., Yang, Q., Thompson, D., and Beletsky, Y. (2015). An ultraluminous quasar with a twelve-billion-solar-mass black hole at redshift 6.30. , 518(7540):512–515.
- Yajima, H. and Khochfar, S. (2016). The role of stellar relaxation in the formation and evolution of the first massive black holes. , 457(3):2423–2432.
- Yoshida, N., Abel, T., Hernquist, L., and Sugiyama, N. (2003). Simulations of early structure formation: Primordial gas clouds. *The Astrophysical Journal*, 592(2):645–663.
- Yoshida, N., Omukai, K., Hernquist, L., and Abel, T. (2006). Formation of primordial stars in a Λ CDM universe. *The Astrophysical Journal*, 652(1):6–25.
- Yu, Q. and Tremaine, S. (2002). Observational constraints on growth of massive black holes. , 335(4):965–976.
- Zeldovich, Y. B. and Novikov, I. D. (1971). *Relativistic astrophysics. Vol.1: Stars and relativity*.
- Zhang, W., Woosley, S. E., and Heger, A. (2008). Fallback and black hole production in massive stars. *The Astrophysical Journal*, 679(1):639–654.